ICFO

Institut
de Ciències
Fotòniques

Continuous-wave optical parametric oscillators and frequency conversion sources from the ultraviolet to the mid-infrared

Kavita Devi

Universitat Politecnica de Catalunya
Barcelona, May 2013

Doctorate Program: **Photonics**

Duration: **2009-2013**

Thesis advisor: **Prof. Majid Ebrahim-Zadeh**

Thesis submitted in partial fulfillment of the requirements for the degree of Doctor of Philosophy of the Universitat Politecnica de Catalunya

May 2013

Dedicated to my loving parents

Declaration

I hereby declare that the matter embodied and presented in the thesis entitled, **"Continuous-wave optical parametric oscillators and frequency conversion sources from the ultraviolet to the mid-infrared"** is the result of investigations carried out by me at the ICFO-Institute of Photonic Sciences, Castelldefels, Barcelona, Spain under the supervision of Prof. Majid Ebrahim-Zadeh, and that it has not been submitted elsewhere for the award of any degree or diploma. In keeping with the general practice in reporting scientific observations, due acknowledgment has been made whenever the work described is based on the findings of other investigators.

Kavita Devi

Certificate

I hereby certify that the matter embodied and presented in this thesis entitled, **"Continuous-wave optical parametric oscillators and frequency conversion sources from the ultraviolet to the mid-infrared"** has been carried out by Miss Kavita Devi at the ICFO-Institute of Photonic Sciences, Castelldefels, Barcelona, Spain, under my supervision, and that it has not been submitted elsewhere for the award of any degree or diploma.

Prof. Majid Ebrahim-Zadeh

(ICFO, Research Supervisor)

Acknowledgements

I am pleased to acknowledge the many individuals, for their support and assistance in different aspects, during the course of this doctoral studies.

First of all, I would like to express my sincere gratitude to Prof. Majid Ebrahim-Zadeh for his guidance, advice, and invaluable ideas, without which this thesis would not have been possible. He has not only supervised me, but has also provided me the enourmous encouragement and support, that gave me enthusiasm and confidence to face a new challenge at any time. His vast knowledge in broader field of science and technology together with industrial experience enriched my growth as a researcher. His ever friendly attitude gave me the freedom to express, explore and implement new ideas. I am indebted to him more than he knows.

I am very grateful to have a wonderful group of labmates. My special thanks goes to Goutam, Adolfo, Chaitanya, Ramaiah, Ossi, Enrique and Stefano, for creating such a great environment in the lab, sharing instruments, thoughts and expertise. The discussions and collaborations with Goutam and Chaitanya have been fruitful during the last years. I would like to extend my special thanks to Chaitanya for always providing me a helping hand, and to Adolfo for helping me translate the abstract of this thesis into Spanish.

I want to express my gratitude to Prof. Luis Torner, Director of the ICFO-Institute of Photonic Sciences, and his management team for making ICFO such a wonderful place for research. The efficiency of the human resource team, purchasing unit, mechanical and electronic workshop, and knowledge and technology transfer unit helped me to concentrate fully on my research.

I am grateful to all my teachers and professors in the school, college and IIT Guwahati for sharing their immense knowledge in wide range of fields and preparing me for the advanced studies. I express my thanks to Prof. A. Khare, Dr. S. Khijwania and Dr. P. Poulose for their belief in me. I would also like to thank my friends, Rajan(bhaiya), Ritwick(bhaiya), Joyee(didi), Arpita, Saurabh, Arup, Anshuman, and including my MSc and BSc friends for sharing their scientific as well as non-scientific views. I can not put my thoughts and feelings into words, when it comes to thank Dhriti. Despite his own busy research schedule, he has always been supportive in every aspects. My heartiest thanks goes to him, for his patience, time, affection and support.

My everlasting gratitude goes to my mother, Rumi Devi and father, Rajendra Nath Sharma for their unconditional and continuous love and support. They are the ones who initiated the intellectual development in me. They have always been my inspiration and a guiding light. Special thanks to my sisters Gitali and Mitu, for being supportive and caring.

Abstract

High-power, continuous-wave (cw) optical parametric oscillators (OPOs), from the ultraviolet (UV) and visible to the near- and mid-infrared (IR) wavelength range, are of interest for a variety of applications such as spectroscopy, trace-gas detection and remote sensing. As such, it is desired to investigate OPOs and different frequency conversion techniques, to cover the spectral regions that are inaccessible to lasers, and that too in a compact and low-cost design.

This thesis presents the development of high-power cw OPOs, and frequency conversion sources, spanning the UV to mid-IR spectral range, employing different designs, experimental configurations and nonlinear crystals, making them compact and cost-effective. Commercial high-power cw lasers at 1940 nm, 1064 nm and 532 nm have been exploited as the pump sources, in the work presented in this thesis.

We have demonstrated a fiber-based cw source at 970 nm, in a simple and practical design. Using direct single-pass second-harmonic-generation (SHG), 13.1 W of output power at 970 nm has been generated in a high-beam-quality, narrow-linewidth, linearly-polarized beam. Further, a technique based on the use of an antiresonant ring (ARR) interferometer for the attainment of optimum output coupling in a cw singly-resonant OPO has been investigated. The technique was deployed in a Yb-fiber-laser-pumped cw OPO based on MgO:PPLN. To extend the tunability of the 1-μm-pumped OPO from the mid-IR to near-IR, SHG of the intracavity signal has been performed in fanout-grating MgO:sPPLT. This compact cw source, tunable across 775–807 nm, provides >3 W of near-infrared power across 56% of SHG tuning range, in high spatial beam quality. We have also generated output in the UV, down to 355 nm, using single-pass configuration based on sum-frequency-generation

of fundamental at 1064 nm and the generated SHG at 532 nm, in BiB_3O_6. Further, we demonstrated an architecture comprising two cw OPOs coupled together with an ARR interferometer, generating two pairs of signal and idler wavelengths, that can be independently and arbitrarily tuned to indefinitely close spacing, through degeneracy, and beyond, across the wavelength range of 870-1370 nm. The OPOs, based on identical MgO:sPPLT crystals, were pumped by a single cw laser at 532 nm. On the other hand, we also demonstrated active mode-locking of cw OPOs using direct low-frequency electro-optic phase-modulation (EOM), opening up the possibility of avoiding the need for ultrafast laser sources and synchronous pumping. We have generated picosecond pulses in doubly- and singly-resonant configuration. Also, a technique based on the deployment of the EOM in combination with an ARR interferometer internal to the cw OPO has been investigated for active mode-locking.

Resumen

Los osciladores ópticos paramétricos (OPOs) de onda continua (cw) y alta potencia en el rango espectral ultravioleta (UV), visible e infrarrojo cercano y medio (IR), son de gran interés para una gran variedad de aplicaciones como: espectroscopia, detección de gases y sensores remotos. Por lo tanto, es vital la investigación en OPOs y diferentes técnicas de conversión de frecuencias con el objetivo de cubrir las regiones espectrales inaccesibles a los láseres, así como lograr diseños compactos y de bajo coste.

Esta tesis presenta el desarrollo de cw OPOs de alta potencia y fuentes de conversión de frecuencias, expandiendo el rango espectral desde el UV hasta el IR medio, empleando diferentes diseños, configuraciones experimentales y cristales no lineales, resultando en diseños compactos y de bajo coste. En el trabajo presentado en esta tesis, se han utilizado como fuentes de bombeo láseres comerciales de alta potencia a 1940 nm, 1064 nm y 532 nm.

Hemos demostrado una fuente basada en fibra a 970 nm con un diseño simple y práctico. Utilizando directamente generación de segundo armónico (SHG) en un paso, se ha logrado generar 13.1 W de potencia de salida a 970 nm con un haz de alta calidad, ancho de línea estrecho y polarización lineal. Adicionalmente, se ha investigado una técnica que emplea un interferómetro de anillo antiresonante (ARR) para conseguir acoplamiento de salida óptimo en un cw OPO simplemente resonante. Esta técnica fue implementada en un cw OPO basado en MgO:PPLN y bombeado por un láser de fibra Yb. Con el objetivo de expandir la sintonización del OPO bombeado a 1 μm desde el IR medio al IR cercano, se ha implementado SHG de la señal intracavidad utilizando MgO:sPPLT con una red *fanout*. El resultado es una fuente cw compacta, sintonizable en el rango 775–807 nm, con potencias del infrarrojo cercano >3 W a lo largo del 56% del rango de sintonización de SHG y con alta calidad espacial del haz. También hemos generado salida en el UV hasta los 355 nm, utilizando una configuración de paso único en BiB_3O_6 para generación de suma de frecuencias entre la fundamental a 1064 nm y la de SHG generada a 532 nm. Además, demostramos una arquitectura incluyendo dos cw OPOs acoplados con un interferómetro ARR, generando dos pares de longitudes de onda señal y *idler* que pueden ser independiente y arbitrariamente sintonizadas, incluso hasta la degeneración y más allá, a lo largo del rango de longitudes de onda 870-1370 nm. Los OPOs utilizan dos cristales idénticos de MgO:sPPLT y fueron bombeados por un cw laser a 532 nm. Por otra parte, también demostramos *mode-locking* activo de un cw OPO utilizando directamente modulación de fase electroóptica (EOM) de baja frecuencia, abriendo la posibilidad de evitar la necesidad de uso de fuentes láser ultrarrápidas y bombeos sincronizados. Mediante esta técnica, hemos generado pulsos de picosegundos tanto en configuraciones doble y simplemente resonantes. Adicionalmente, se ha investigado ora técnica que integra un EOM combinado con un interferómetro ARR dentro de la cavidad del cw OPO con el objetivo de conseguir *mode-locking* activo.

Publications

Journal publications

1. **K. Devi,** S. Chaitanya Kumar, and M. Ebrahim-Zadeh, "Mode-locked continuous-wave mid-infrared optical parametric oscillator: pulse formation and spectral characterization," To be submitted (2013).
2. **K. Devi,** S. Chaitanya Kumar, and M. Ebrahim-Zadeh, "Tunable continuous-wave, ultraviolet source based on intracavity sum-frequency-generation in an optical parametric oscillator," Opt. Express, submitted (2013).
3. **K. Devi,** S. Chaitanya Kumar, and M. Ebrahim-Zadeh, "Directly phase-modulation-mode-locked doubly-resonant optical parametric oscillator," Opt. Express, submitted (2013).
4. S. Chaitanya Kumar, **K. Devi,** and M. Ebrahim-Zadeh, "Stable, continuous-wave, Yb-fiber-based single-pass ultraviolet source," Opt. Letters, submitted (2013).
5. **K. Devi,** S. Chaitanya Kumar, A. Esteban-Martin, and M. Ebrahim-Zadeh, "Dual-wavelength interferometrically-coupled continuous-wave optical parametric oscillator," Laser and Photonics Reviews, submitted (2013).
6. **K. Devi,** S. Chaitanya Kumar, and M. Ebrahim-Zadeh, "High-power, continuous-wave, single-frequency, all-periodically-poled, near-infrared source," Opt. Letters 37, 5049-5051 (2012).
7. **K. Devi**, S. Chaitanya Kumar, and M. Ebrahim-Zadeh, "Mode-locked, continuous-wave, singly resonant optical parametric oscillator," Opt. Letters 37, 3909-3911 (2012).

8. **K. Devi,** S. Chaitanya Kumar, A. Esteban-Martin, and M. Ebrahim-Zadeh, "Antiresonant ring output-coupled continuous-wave optical parametric oscillator," Opt. Express 20, 19313-19321 (2012).

9. A. Esteban-Martin, G. K. Samanta, **K. Devi,** S. Chaitanya Kumar, and M. Ebrahim-Zadeh, "Frequency-modulation-mode-locked optical parametric oscillator," Opt. Letters 37, 115-117 (2012).
   (Among Top-10 downloaded articles (OSA) in Jan, 2012.)

10. S. Chaitanya Kumar, G. K. Samanta, **K. Devi,** S. Sanguinetti, and M. Ebrahim-Zadeh, "Single-frequency, high-power, continuous-wave fiber-laser-pumped Ti:sapphire laser," Appl. Optics 51, 15-20 (2012).
    (Selected for the cover page of the 50^{th}Anniversary issue; Among Top-10 downloaded articles (OSA) in the year 2012.)

11. G. K. Samanta, S. Chaitanya Kumar, **K. Devi,** and M. Ebrahim-Zadeh, "High-power, continuous-wave Ti:sapphire laser pumped by fiber-laser green source at 532 nm," Optics and Lasers in Engineering 50, 215-219 (2012).

12. **K. Devi,** S. Chaitanya Kumar, and M. Ebrahim-Zadeh, "13.1 W, high-beam-quality, narrow-linewidth continuous-wave fiber-based source at 970 nm," Opt. Express 19, 11631-11637 (2011).
    (Selected for July issue of Virtual Journal of Biomedical Optics, 6(7), 2011.)

13. S. Chaitanya Kumar, G. K. Samanta, **K. Devi,** and M. Ebrahim-Zadeh, "High-efficiency, multicrystal, single-pass, continuous-wave second harmonic generation," Opt. Express 19, 11152-11169 (2011).

14. S. Chaitanya Kumar, **K. Devi,** G. K. Samanta, and M. Ebrahim-Zadeh,

“Fiber-laser-based green-pumped continuous-wave singly-resonant optical parametric oscillator,” Journal of Laser Physics 21, 782-789 (2011).

15. G. K. Samanta, S. Chaitanya Kumar, **K. Devi,** and M. Ebrahim-Zadeh, “Multi-crystal, continuous-wave, single-pass second-harmonic-generation with 56% efficiency,” Opt. Letters 35, 3513-3515 (2010).
(Highlighted in Laser Focus World, Jan 2011; Among Top-10 downloaded articles over two years, 2011-2012.)

Proceeding publications

1. **K. Devi,** S. Chaitanya Kumar, G. K. Samanta, A. Esteban-Martin, and M. Ebrahim-Zadeh, “Continuous-wave mode-locked optical parametric oscillator,” Proc. SPIE 8434, 84340D (2012).

2. **K. Devi,** S. Chaitanya Kumar, A. Esteban-Martin, and M. Ebrahim-Zadeh, “Interferometeric output coupling of a continuous-wave optical parametric oscillator,” Proc. SPIE 8434, 84340E (2012).

3. **K. Devi,** S. Chaitanya Kumar, and M. Ebrahim-Zadeh, “High-beam-quality, narrow-linewidth, 13 W continuous-wave fiber-based source at 970 nm,” Proc. SPIE 8434, 843405 (2012).

4. **K. Devi,** S. Chaitanya Kumar, G. K. Samanta, and M. Ebrahim-Zadeh, “Highly efficient continuous-wave single-pass second-harmonic generation using multicrystal scheme,” Proc. SPIE 8173, 81730K (2010).

5. **K. Devi,** S. Chaitanya Kumar, G. K. Samanta, and M. Ebrahim-Zadeh, “Continuous-wave-fiber-laser-pumped Ti:sapphire laser,” Proc. SPIE 8173, 81730J (2010).

Conference publications

1. **K. Devi,** S. Chaitanya Kumar, and M. Ebrahim-Zadeh, “Actively mode-locked continuous-wave singly-resonant mid-infrared optical parametric oscillator,” MICS, Paris, France, October 2013.

2. **K. Devi,** S. Chaitanya Kumar, and M. Ebrahim-Zadeh, “Stable, continuous-wave, fiber-laser-based, ultraviolet generation in BiB_3O_6,” CLEO/Europe-EQEC, Munich, Germany, May 2013.

3. V. Ramaiah Badarla, **K. Devi,** S. Chaitanya Kumar, A. Esteban-Martin, and M. Ebrahim-Zadeh, “Interferometrically coupled two-color femtosecond optical parametric oscillator,” International Conference on Fiber Optics and Photonics, Chennai, India, December 2012.

4. **K. Devi,** S. Chaitanya Kumar, and M. Ebrahim-Zadeh, “Frequency-modulation-mode-locked singly-resonant optical parametric oscillator,” NLO 50 International Symposium, Barcelona, Spain, October 2012.

5. **K. Devi,** S. Chaitanya Kumar, and M. Ebrahim-Zadeh, “Tunable, high-power, all-periodically-poled, continuous-wave, intracavity-frequency-doubled optical parametric oscillator,” 5th EPS-QEOD Europhoton Conference, Stockholm, Sweden, August 2012.

6. **K. Devi,** S. Chaitanya Kumar, and M. Ebrahim-Zadeh, “Actively mode-locked optical parametric oscillator using low-frequency phase-modulation,” Conf. Lasers and Electro-Optics (CLEO), San Jose, California, USA, May 2012.

7. **K. Devi,** V. Ramaiah-Badarla, S. Chaitanya Kumar, A. Esteban-Martin, and M. Ebrahim-Zadeh, “Dual-wavelength, interferometrically coupled

continuous-wave optical parametric oscillators," Conf. Lasers and Electro-Optics (CLEO), San Jose, California, USA, May 2012.

8. **K. Devi,** S. Chaitanya Kumar, A. Esteban-Martin, and M. Ebrahim-Zadeh, "Interferometrically output-coupled continuous-wave optical parametric oscillator," Conf. Lasers and Electro-Optics (CLEO), San Jose, California, USA, May 2012.

9. **K. Devi,** S.Chaitanya Kumar, G. K. Samanta, A. Esteban-Martin, and M. Ebrahim-Zadeh, "Continuous-wave mode-locked optical parametric oscillator," SPIE Photonics Europe, Brussels, Belgium, April 2012.

10. **K. Devi,** S.Chaitanya Kumar, A. Esteban-Martin, and M. Ebrahim-Zadeh, "Interferometeric output coupling of a continuous-wave optical parametric oscillator," SPIE Photonics Europe, Brussels, Belgium, April 2012.

11. **K. Devi,** S.Chaitanya Kumar, and M. Ebrahim-Zadeh, "High-beam-quality, narrow-linewidth, 13 W continuous-wave fiber-based source at 970 nm," SPIE Photonics Europe, Brussels, Belgium, April 2012.

12. S. Chaitanya Kumar, G. K. Samanta, **K. Devi,** S. Sanguinetti, and M. Ebrahim-Zadeh, "High-power, single-frequency Ti:sapphire laser pumped by a continuous-wave fiber laser green source," CLEO/Europe-EQEC, Munich, Germany, May 2011.

13. **K. Devi,** S. Chaitanya Kumar, G. K. Samanta, and M. Ebrahim-Zadeh, "Highly efficient continuous-wave single-pass second-harmonic generation using multicrystal scheme," International Conference on Fiber Optics and Photonics, Guwahati, India, December 2010.

14. **K. Devi,** S. Chaitanya Kumar, G. K. Samanta, and M. Ebrahim-Zadeh, "Continuous-wave-fiber-laser-pumped Ti:sapphire laser," International Conference on Fiber Optics and Photonics, Guwahati, India, December 2010.

15. G. K. Samanta, S. Chaitanya Kumar, **K. Devi,** and M. Ebrahim-Zadeh, "55%-efficient, 13-W, single-pass SHG of a cw Yb-fiber laser in a double-crystal scheme," Conf. Lasers and Electro-Optics (CLEO), San Jose, California, USA, May 2010.

16. G. K. Samanta, S. Chaitanya Kumar, **K. Devi,** and M. Ebrahim-Zadeh, "Fiber-laser-pumped Ti:sapphire laser," Conf. Lasers and Electro-Optics (CLEO), San Jose, California, USA, May 2010.

Contents

List of Tables

List of Figures

Chapter 1

Introduction

The invention of the laser [1] represents an extraordinary leap in science and technology. With its tremendous progress in the last few decades, it has now become omnipresent, catering for various industrial and medical applications, while also playing important role in different aspects of our life. The unique property of direct generation and manipulation of coherent light has made the laser a remarkable tool. The laser is a source that emits light with spectral purity based on stimulated emission between quantized energy levels in the laser material. There are many practical applications where high-power coherent light source with high beam quality and, importantly, broad wavelength tunability is required [2]. To develop a tunable laser, materials with broadened energy levels that result in broad gain spectra can be used. However, the maximum continuous spectral coverage still remains limited [3]. Figure 1.1 shows the wavelength coverage of some tunable lasers. The most prominent and widely available tunable laser is the Ti:sapphire laser. It has a broad gain bandwidth, which is also advantageous for ultrashort pulse generation. The tunability of the Ti:sapphire laser is, however, limited to at best 300–400 nm. In addition, even after five decades since the invention of the laser, due to the restricted availability of suitable gain media, many regions of the optical spectrum extending from the ultraviolet (UV) to the mid-infrared (mid-IR) remain inaccessible to lasers.

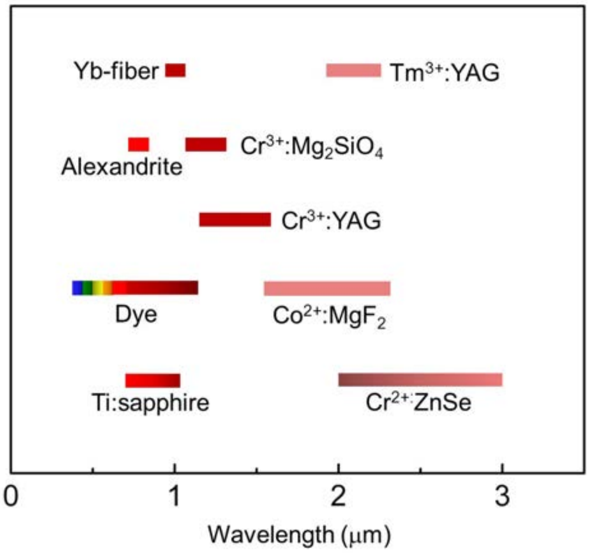

Figure 1.1: Spectral coverage of conventional tunable lasers.

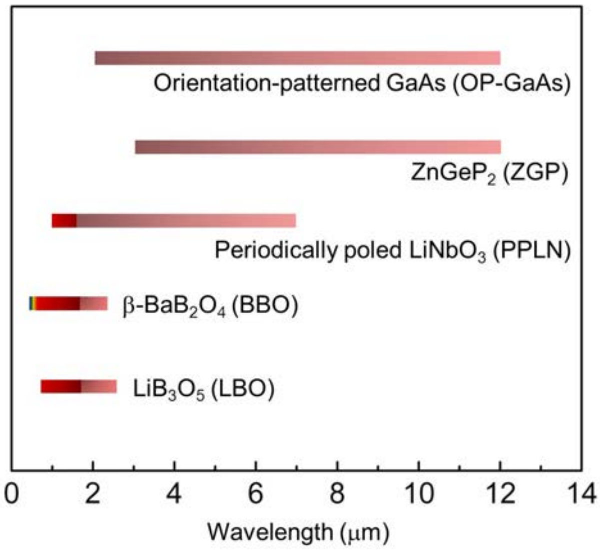

Figure 1.2: Spectral tuning available from OPOs.

The realization of the potential of nonlinear optical phenomena to provide coherent radiation was indeed a major step in the direction of overcoming the spectral limitations of lasers [4], as it led to the developement of optical parametric oscillators (OPOs) [5]. OPOs are potentially capable of providing tunable coherent radiation from a single device across extended spectral regions. Figure 1.2 shows the tuning capability of OPOs. They can also deliver output over the entire temporal spectrum from continuous-wave (cw) to ultrafast femtosecond time-scales. Such devices are of great interest for a variety of applications from spectroscopy and biomedicine to remote sensing and environmental monitoring [5].

Nonlinear effects in electromagnetism had indeed been observed long before the invention of laser, in the late 19th century, by John Kerr [6], and later by Raman in 1927 [7], when he discovered spontaneous scattering of photons into new frequencies in passing through a transparent medium. The word nonlinear optics was introduced in 1943 by E. Schrodinger [8, 9]. It was then in 1961, when the unprecedented optical intensities available from the laser made the first observation of a coherent nonlinear optical effect possible, as reported by Franken et al. [10], who demonstrated second-harmonic-generation (SHG) of Ruby laser at 347.2 nm in the quartz crystal. The first observation of sum-frequency-generation (SFG) was then made by M. Bass in 1962 [11]. However, in order to obtain high conversion efficiencies in nonlinear optical processes, phase-matching condition needs to be satisfied, which means that a proper phase relationship needs to be maintained between the interacting waves along the propagation direction. With the phase-matching condition satisfied, in the same year of 1962, J. A. Giordmaine demonstrated the first experiment on the generation of intense SHG, by matching the phase velocities of the fundamental and the second-harmonic light [12], and later in 1963, Smith and Braslau demonstrated the first difference-frequency-generation (DFG) [13]. During the same period, the importance of parametric generation and amplification was recognized as an important technique for the generation of tunable coherent radiation in new spectral regions [14–16]. In 1965, Wang and Racette demonstrated DFG accompanied with the measurement of parametric gain [17]. This process of DFG then corroborated the optical parametric generation. In the same year, the first experimental demonstration of an OPO was reported by Giordmaine and Miller [18]. The pump wavelength used in the experiment was at 529 nm, obtained by the second-harmonic-generation of a pulse Nd^{+3}:$CaWO_4$ laser, and the OPO was tunable from 970 nm to 1150 nm. The pulsed OPO was then followed by the demonstration of cw OPOs, independently by Smith et al. [19] and Byer et al. [20] in 1968. Although, since these early days, the basic principles behind the optical parametric generation have been known, due to the unavailability of suitable pump lasers and proper nonlinear optical materials, the extension of these techniques to shorter time domains of picoseconds and femtoseconds were not possible for another 20 years.

In the 1980s, the advent of new nonlinear optical materials and new laser sources with improved spatial and spectral coherence and sufficient intensity in the desired spectral regions once again prompted a major resurgence of interest in the development of pulsed OPOs [21–24]. This then led to the first demonstration of a synchronously-pumped femtosecond OPO by D. C. Edelstein in 1989 [25]. Today, with the tremendous progress in the field, there are numerous pulsed OPOs in the spectral regions from the mid-IR [2, 26] to the visible [27], and further down to the UV [28], using nonlinear crystals such as LiB_3O_5 (LBO), β-BaB_2O_4 (BBO) and BiB_3O_6 (BIBO). The generation of terahertz radiation from pulsed OPOs has also been demonstrated [29].

Due to the substantially lower nonlinear gain available under cw pumping, cw OPOs have been traditionally the more challenging class of devices. The spectrally pure, high-power and tunable cw OPO are of great importance for numerous applications. A high-power (watt-level) pump laser, optical material with high nonlinearity, and lower oscillation threshold pump power are typical requirements for successful operation of cw OPOs. The singly-resonant oscillator (SRO) configuration of a cw OPO, where a single wave (signal or idler) resonates inside the OPO cavity, despite having high operation threshold power, are advantageous for the generation of high-power single-frequency radiation over extended spectral regions. The first cw SRO was demonstrated by Yang et al. in 1993 using birefringent KTP crystal [30], utilizing type II noncritical phase-matching. To overcome the high cw SRO threshold, various techniques based on different resonance configurations have also been deployed, which include doubly-resonant oscillator (DRO), triply-resonant oscillator (TRO), pump-enhanced SRO (PE-SRO) and intracavity SRO (IC-SRO) [31–34]. The advent of quasi-phase-matching technology based on periodical poling of nonlinear materials in 1991 [35], had a major impact on the development of high-power cw OPOs. In 1996, Bosenberg at al. [36] demonstrated the first cw OPO based on periodically-poled $LiNbO_3$ (PPLN). Since then, the development of novel quasi-phase-matched (QPM) materials, new innovations in resonance configurations and improved pumping techniques using stable, high-power laser sources have led to important breakthroughs in cw OPOs [37–41].

A majority of cw OPOs developed till date are based on PPLN [36–39, 41–43]. The high effective nonlinearity (d_{eff}~17 pm/V) and long interaction length available with PPLN crystal has brought the threshold of cw SROs well within the reach of available cw lasers. It has enabled the cw SRO operation at unprecedented power levels, high conversion efficiencies, and providing spectral coverage from 1 μm to 5 μm [38, 41–43]. To prevent the PPLN crystal from photorefractive damage, the crystal is doped with MgO, then well-known as MgO:PPLN. On the other hand, MgO-doped periodically-poled stoichiometric $LiTaO_3$ (MgO:sPPLT), due to its increased resistance to photo-refractive damage and moderate nonlinear coefficient (d_{eff}~9 pm/V), is a promising material in the UV to near-infrared (near-IR) regions, especially in high-power operation [40, 44]. The attainment of first-order quasi-phase-matching for the generation of UV output is, however, challenging till date. To increase the extraction

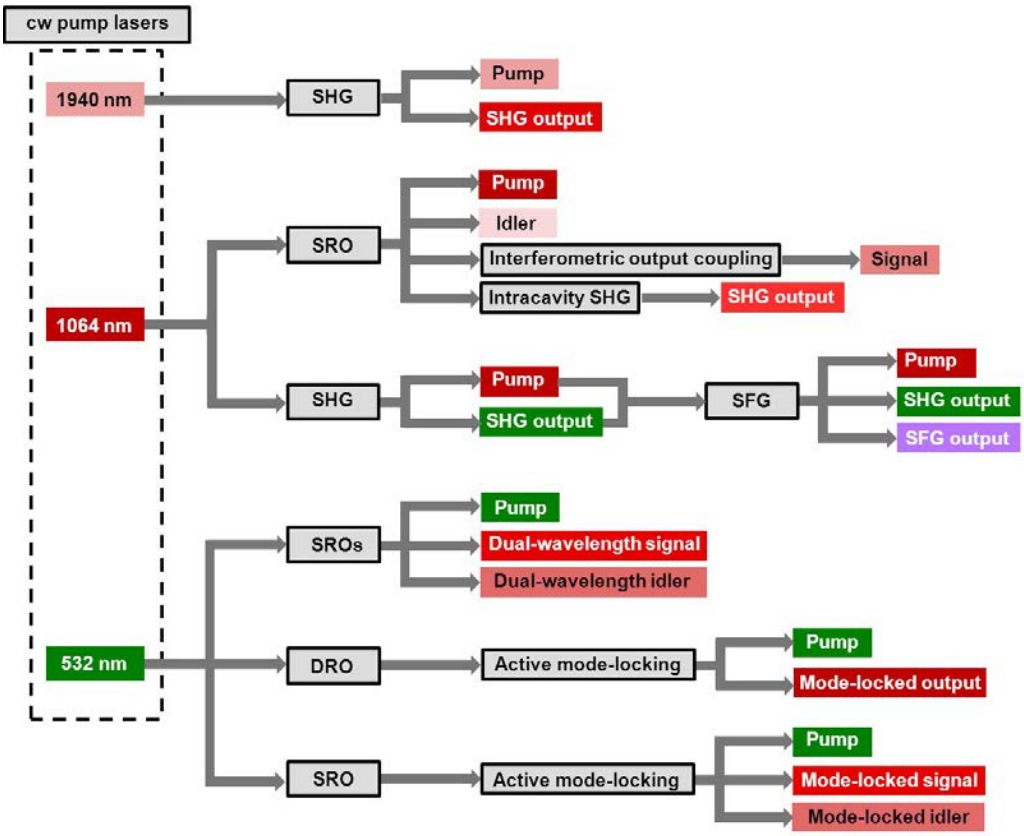

Figure 1.3: Approach of the thesis research work.

efficiency and wavelength tunability of cw SROs, various techniques such as output coupling and intracavity SHG have also been employed [41, 45, 46]. The advent of these QPM nonlinear crystals has also enabled the direct active mode-locking of cw OPOs, generating steady-state pulses [47].

The approach of the research work presented in this thesis is shown in Fig. 1.3. The work performed was purely under cw pumping, using three commercial, narrow-linewidth, linearly-polarized, cw laser sources. Using a compact fiber laser at 1940 nm, efficient single-pass SHG at 970 nm, has been demonstrated and investigated. Another fiber laser at 1064 nm has been used to pump a cw SRO based on MgO:PPLN. The cw SRO, tunable in the mid-IR range, has been interferometrically output-coupled, providing continuous and fine control of output-coupling optimization. To extend the emission into near-IR range, the intracavity signal has been frequency-doubled using a fanout-grating MgO:sPPLT. To generate output in the UV, down to 355 nm, sum-frequency-mixing of the second-harmonic output of the fiber laser and the pump at 1064 nm has been performed in BIBO. The solid-state laser in the green has been used to demonstrate a dual-wavelength OPO. The cw OPOs, both in DRO as well as in SRO configuration, pumped in the green, and based on MgO:sPPLT, are further actively mode-locked to generate stable picosecond pulses. The thesis is organized into 9 chapters.

Chapter 2 provides an introduction to nonlinear optics and various nonlinear optical phenomena, including SHG, SFG, DFG and OPO. The wavelength tuning capabilities of an OPO have been discussed. Since a proper cavity design is required for successful operation of a cw OPO, we have discussed the design issues. The phenomenon of active mode-locking method that can be employed in cw OPOs have also been presented in this chapter.

Out of the different viable methods for SHG that have relied on intracavity, external resonant enhancement, and multiple-pass configurations, the external single-pass SHG (SP-SHG) is the simplest approach. The combination of a cw fiber laser and SP-SHG based on a periodically-poled nonlinear crystal is a potential approach for high-power generation, not only because of its compact and practical design, but also due to the high spatial beam quality and narrow linewidth, which is inherently transfered from the fiber laser to the second-harmonic output. We demonstrate such a high-power, fiber-laser-based, linearly-polarized, cw source at 970 nm in chapter 3. Also relevant theoretical studies for the characterization of SP-SHG in the crystal have been performed and presented in this chapter.

In chapter 4, we demonstrate the successful deployment of an antiresonant ring (ARR) interferometer for the attainment of optimum output coupling in a cw OPO. The cw OPO, configured as a SRO, and pumped at 1064 nm, is based on MgO:PPLN crystal, with the ARR interferometer integrated into one arm of the standing-wave cavity. The proof-of-principle demonstration confirms the effectiveness of the technique for continuous, in situ, and fine control of output coupling in cw OPOs to achieve maximum output power at any arbitrary pumping level above threshold. The theoretical calculations performed for conventional output-coupled cw SRO are also presented in this chapter.

In chapter 5, a high-power, single-frequency, cw source tunable across 775-807 nm in the near-infrared, based on internal SHG of a cw SRO, pumped at 1064 nm, is demonstrated. The compact, all-periodically-poled source employs multigrating MgO:PPLN crystal for the OPO and a fanout-grating MgO:sPPLT crystal for intracavity SHG. The cw SRO is further tunable across 3125-3396 nm in the idler, providing high output power. The results of output power across the tuning range, power scaling, power stability, beam quality and linewidth measurement are presented in this chapter.

Using the cw Yb-fiber laser at 1064 nm and the second-harmonic output of the pump, we performed sum-frequency-mixing in BIBO. We have demonstrated the generation of cw UV output at 354.7 nm in single-pass configuration. The results of power scaling, power stability, frequency stability, and beam quality are presented in chapter 6.

In chapter 7, we demonstrate two cw OPOs coupled together with an ARR interferometer, generating two pairs of signal and idler wavelengths. The OPOs, configured as SROs, based on identical 30-mm-long MgO:sPPLT crystals, are pumped by a single cw laser at 532 nm. The two pairs of signal and idler wavelengths can be independently and arbitrarily tuned to indefinitely close spacing, through degeneracy, and beyond, across the wavelength range of 870-1370 nm. The closest frequency separation and power scaling results are also presented in this chapter.

In chapter 8, the green-pumped cw OPO is then further demonstrated to generate mode-locked pulses. The generation of picosecond pulses is demonstrated in both DRO as well as SRO configuration. A mode-locking technique based on the deployment of a phase modulator in combination with an ARR interferometer internal to a cw DRO, providing phase-to-amplitude modulation, has been presented. The direct active mode-locking of the DRO based on pure phase-modulation using the phase modulator as the single mode-locking element is then demonstrated. Further, direct phase-modulation mode-locking of a cw OPO in SRO configuration has been achieved. The OPOs, pumped at 532 nm, are based on MgO:sPPLT as the nonlinear gain crystal. The results of record picosecond pulse duration, effect of intracavity frequency detuning and change in modulation depth on the pulse duration and repetition rate have been investigated. The output spectrum and the confirmation of mode-locked operation have also been presented in this chapter. Finally, in chapter 9 the thesis has been concluded with some of our ongoing effort and future outlook in the field.

Chapter 2

Basics of nonlinear optics

2.1 The origin of optical nonlinearity

Optics is the study of interaction of electromagnetic radiation with matter. When an electromagnetic wave interacts with a dielectric material, the electrons are displaced with respect to the nuclei, and it induces a polarization, defined as dipole moment per unit volume. The dipole oscillations in a dielectric material can result in the emission of light waves. The energy and wavelength of the light wave so generated is determined by the dipole moment and dipole oscillation frequency [48, 49]. When the magnitude of the input electric field is small, the induced polarization follows a linear dependence on the input field strength,

$$P = \epsilon_0 \chi^{(1)} E \tag{2.1}$$

where P and E are the polarization and electric field vectors, respectively, $\chi^{(1)}$ is the linear susceptibility of the medium, and ϵ_0 is the permittivity of free space. This is the regime of linear optics, where the dipole oscillation and the emitted optical wave from the dipole are at the same frequency as the input field. On the other hand, if the field strength is strong enough, the dipole displacement becomes nonlinear with the electric field. This is the regime of nonlinear optics, where the dipole oscillates not only at the input frequency, but also above and below the input frequency, generating new wavelengths. In such case, the induced polarization, P, in its most general form is given by

$$P = \epsilon_0(\chi^{(1)}E + \chi^{(2)}E^2 + \chi^{(3)}E^3 + ...) \tag{2.2}$$

where $\chi^{(2)}$, $\chi^{(3)}$,..... are the higher-order nonlinear susceptibilities. The crystalline media that exhibit even-order nonlinearity are non-centrosymmetric materials, whereas for odd-order nonlinearity, centrosymmetric as well as non-centrosymmetric materials can be used. For the attainment of such optical nonlinearity, higher optical intensities are required, which can be provided only by a laser. Nonlinear optics is a vast field that involves the study of various nonlinear optical interactions. The work demonstrated in this thesis is based on second-order nonlinear processes. As such, the brief discussion on nonlinear processes given here will be limited to interactions that involve the second-order nonlinear susceptibility, $\chi^{(2)}$. Description of other interactions can be found in a multitude of references [4, 48, 50].

2.2 Second-order nonlinear susceptibility

The second-order nonlinear optical interactions can be described in terms of the nonlinear polarization given by

$$P^{NL} = \epsilon_0\chi^{(2)}E^2 \tag{2.3}$$

where the second-order nonlinear susceptibility, $\chi^{(2)} = \chi^{(2)}_{ijk}$, is a tensor of rank 3. The indices i, j, k refer to the Cartesian components of the field and represent the polarization directions. The d-tensor notation, which is used when the Kleinman symmetry condition is valid, is given by [48, 50]

$$d_{ijk} = \frac{1}{2}\chi^{(2)}_{ijk}. \tag{2.4}$$

Under the Kleinman symmetry condition, where frequencies of the interacting waves are far from the resonance frequency of the material, the nonlinear susceptibility is essentially independent of frequency, and the indices can be permuted without permuting the frequencies. The nonlinear susceptibility tensor can then be contracted into a 3x6 matrix, and the nonlinear polarization is described by

$$\begin{pmatrix} P_x \\ P_y \\ P_z \end{pmatrix} = 2\epsilon_0 K \begin{bmatrix} d_{11} & d_{12} & d_{13} & d_{14} & d_{15} & d_{16} \\ d_{21} & d_{22} & d_{23} & d_{24} & d_{25} & d_{26} \\ d_{31} & d_{32} & d_{33} & d_{34} & d_{35} & d_{36} \end{bmatrix} \begin{pmatrix} E_x^2 \\ E_y^2 \\ E_z^2 \\ E_yE_z + E_zE_y \\ E_xE_z + E_zE_x \\ E_xE_y + E_yE_x \end{pmatrix} \tag{2.5}$$

where K is the degeneracy factor, whose value depends on the conversion processes.

2.3 Second-order nonlinear optical interactions

If we consider an optical field consisting of two distinct frequency components, ω_1 and ω_2, incident upon a nonlinear medium, which can be represented by

$$E(t) = E_1(t)e^{-i\omega_1 t} + E_2(t)e^{-i\omega_2 t} + c.c. \tag{2.6}$$

then using equations 2.3 and 2.6, the second-order nonlinear polarization is given by

$$P^{NL} = \sum_n P(\omega_n)e^{-i\omega_n t} = \epsilon_0\chi^{(2)}[E_1^2 e^{-2i\omega_1 t} + E_2^2 e^{-2i\omega_2 t} + 2E_1E_2 e^{-i(\omega_1+\omega_2)t} + 2E_1E_2^* e^{-i(\omega_1-\omega_2)t} + c.c.] + 2\epsilon_0\chi^{(2)}[E_1E_1^* + E_2E_2^*] \tag{2.7}$$

where the first two terms on the right-hand-side represent the second-harmonic-generation (SHG) process, the third and fourth term represents the sum-frequency-generation (SFG) and difference-frequency-generation (DFG) processes, respectively, and the last term is known as optical rectification (OR).

It is to be noted that the degenaracy factor, K, described in section 2.2, takes the value of 1/2 for SHG and optical rectification, and 1 for the other conversion processes.

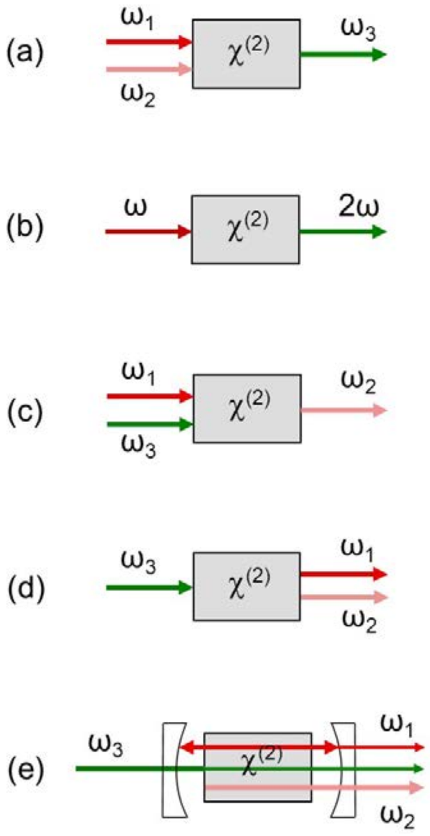

Figure 2.1: Schematic of various second-order nonlinear processes. (a) SFG, (b) SHG, (c) DFG, (d) OPG, and (e) OPO.

The physical meaning of these second-order nonlinear frequency conversion processes are illustrated using the photon picture in Fig. 2.1. In SFG process, as shown in Fig. 2.1(a), two low-energy pump photons at frequencies ω_1 and ω_2, are combined to generate one higher-energy photon at frequency, $\omega_3 = \omega_1 + \omega_2$. The SHG is the degenerate case of SFG process, where two low-energy pump photons at same frequency, $\omega_1 = \omega_2 = \omega$, are combined to generate one photon of energy twice that of the pump photon energy, and at frequency $\omega_3 = 2\omega$, as shown in Fig. 2.1(b). Another special case that has found important applications is when ω_1=0 and $\omega_3 = \omega_2 = \omega$. Then, one of the input fields is static, and the refractive index of the medium is affected through the linear electro-optic effect. This is also known as the Pockels effect. In DFG process, two pump photons of frequency, ω_1 and ω_3, are combined to generate one photon at difference frequency of $\omega_2 = \omega_1 - \omega_3$, as shown in Fig. 2.1(c). A special case, when the two pump photons have the same frequency, ω, resulting in $\omega_2 = 0$, leads to optical rectification, where a static electric field is created within the nonlinear medium. Figure. 2.1(d) shows another type of process known as parametric down-conversion or optical parametric generation (OPG), where spontaneous break-down of high-energy pump photon at frequency, ω_3, into two constituent low-energy photons at frequencies, ω_1 and ω_2, occurs. The two generated wavelengths are referred to as the signal and the idler, of which the signal is, generally, the one with the shorter wavelength. For practical realization of the parametric process and to obtain macroscopic output, the nonlinear medium is enclosed within an optical resonator, and the device is then called optical parametric oscillator (OPO), as shown in Fig. 2.1(e).

2.4 Coupled-wave equations for second-order nonlinear processes

The previous sections of this chapter have shown the response of a nonlinear medium to intense optical field, that induces nonlinear polarization, resulting in the generation of new frequency components. The interaction between the involved fields can be described by Maxwell's wave equations [48].

For a nonlinear, non-magnetic optical medium that contain no free charges and no free currents, the optical wave equation for the propagation of electromagnetic radiation through this medium can be represented by

$$\nabla^2 E - \frac{1}{c^2}\frac{\partial^2 E}{\partial t^2} = \frac{1}{\epsilon_0 c^2}\frac{\partial^2 P}{\partial t^2} \tag{2.8}$$

where $c=1/\sqrt{\mu_0\epsilon_0}$ is the speed of light in vacuum, and μ_0 is the permeability of free space.

In a lossless nonlinear medium, the optical field at a frequency, ω_j, where j=1,2,3 represent the three interacting fields propagating in the z direction, is given by

$$E_j(z,t) = E(z,\omega_j)e^{i(k_j z-\omega_j t)} + c.c. \tag{2.9}$$

and the nonlinear source term is given by

$$P_j(z,t) = P(z,\omega_j)e^{i(k_j z-\omega_j t)} + c.c. \tag{2.10}$$

where k_j is the wavenumber expressed as

$$k_j = \frac{n_j(\omega_j)\omega_j}{c} \tag{2.11}$$

with refractive index, n_j represented as

$$n_j = \sqrt{\frac{\epsilon(\omega_j)}{\epsilon_0}} \tag{2.12}$$

where ϵ is the permittivity of the medium at frequency, ω_j. In the above expressions, we have assumed that the amplitudes of the fields vary slowly over a distance comparable to the wavelength, known as *slowly-varying amplitude approximation* and is valid whenever [48],

$$\frac{d^2E_j}{dz^2} \ll \left|k_j\frac{dE_j}{dz}\right|. \tag{2.13}$$

Using equations 2.3, 2.9, 2.10 and 2.13, the wave equation for each field involved becomes

$$\frac{\partial E_1}{\partial z} = \frac{i\omega_1^2 d_{eff}}{k_1c^2}E_3E_2^*e^{i\Delta kz} \tag{2.14}$$

$$\frac{\partial E_2}{\partial z} = \frac{i\omega_2^2 d_{eff}}{k_2c^2}E_3E_1^*e^{i\Delta kz} \tag{2.15}$$

$$\frac{\partial E_3}{\partial z} = \frac{i\omega_3^2 d_{eff}}{k_3c^2}E_1E_2e^{-i\Delta kz} \tag{2.16}$$

where d_{eff} is the effective nonlinear coefficient, and $\Delta k = k_3 - k_2 - k_1$ is called the wavevector mismatch or phase-mismatch. The effective nonlinear coefficient and the wavevector mismatch, both depend on material properties, propagation direction, and the optical frequencies. Equations 2.14, 2.15 and 2.16 are called *coupled-amplitude equations*, where various frequency components are coupled by the nonlinear interaction. It shows the variation in the amplitude of one field due to its coupling to the other fields.

2.5 Phase-matching

For the attainment of an efficient nonlinear conversion process, two conditions need to be satisfied. One is the energy conservation, where the interacting waves obey the frequency relation, $\omega_3 = \omega_1 + \omega_2$, and the second is the phase-matching between the optical fields, given by $\Delta k = k_3 - k_2 - k_1 = 0$. A perfect phase-matching, where $\Delta k = 0$, is the ideal case. In classical picture, at perfect phase matching, the individual dipoles in the medium are properly phased, resulting in the addition of the field emitted by each dipole in the forward direction. The field amplitude grows linearly with the propagation distance, as shown in Fig. 2.2(a). However, in general, as the optical waves at different frequencies propagate with different phase velocities, because of the dispersion in the nonlinear medium, $\Delta k \neq 0$. Because of this, after travelling a short distance known as the coherence length, $l_c = 2\pi/\Delta k$, the relative phase of the interacting waves slips by 180^o. Along the propagation direction in the nonlinear medium, the waves step in and out of phase periodically, resulting in exchange of energy back and forth. This periodic oscillation along the propagation direction is illustrated as the phase-mismatch or non-phase-matched curve in Fig. 2.2(b). There are two important techniques to achieve phase-matching, birefringent phase-matching (BPM) and quasi-phase-matching (QPM).

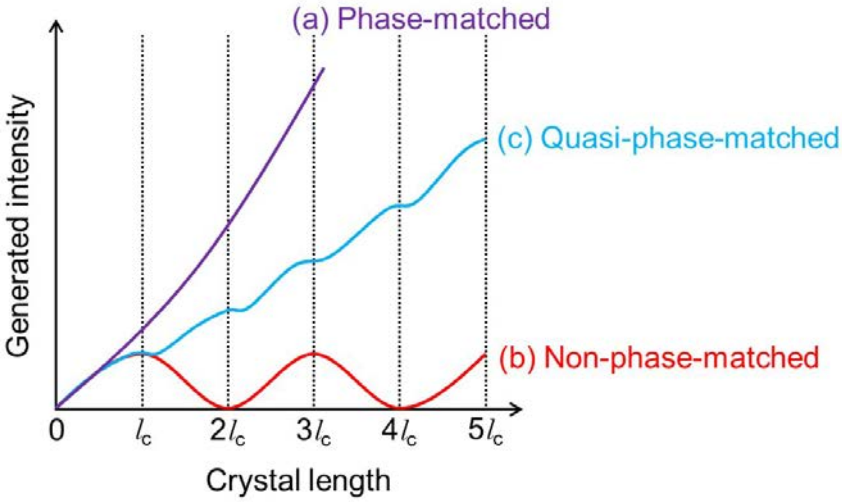

Figure 2.2: Generated wave intensity as a function of propagation distance in nonlinear crystal for (a) perfectly phase-matched ($\Delta k = 0$), (b) non-phase-matched ($\Delta k \neq 0$), and (c) quasi-phase-matched conditions.

2.5.1 Birefringent phase-matching

The most common technique for achieving phase-matching is the birefringent phase-matching (BPM), where the birefringence of a nonlinear crystal is exploited. Birefringence is the property of some anisotropic optical materials, where the refractive index of the material depends on the polarization and propagation direction of light. When the interacting waves of different frequencies are polarized differently, their corresponding phase velocities can be adjusted, so that the index difference due to dispersion is balanced by the index difference due to birefringence.

Depending upon the number of optic axes, a birefringent crystal can be divided onto two categories, uniaxial (one optic axis) and biaxial crystals (two optic axes) [50, 51]. In a uniaxial crystal, the light beam whose polarization is normal to the optic axis is called an ordinary beam or o-beam, and the beam polarized in the optic axis plane is known as extraordinary beam or e-beam. The refractive index of the o-beam, n_o, does not depend on the propagation direction, whereas the refractive index of the e-beam, n_e, does. If θ is the angle between propagation direction and the optic axis, then the refractive index of the e-beam as a function of θ is given by

$$\frac{1}{n_e^2(\theta)} = \frac{cos^2(\theta)}{n_o^2} + \frac{sin^2(\theta)}{n_e^2} \tag{2.17}$$

The difference, $\Delta n(\theta) = n_e(\theta) - n_o$, determines the birefringence of the material. Thus, the following equations are evident:

$$n_e(\theta = 0^o) = n_o \tag{2.18}$$

$$n_e(\theta = 90^o) = n_e \tag{2.19}$$

$$\Delta n(\theta = 0^o) = 0 \tag{2.20}$$

$$\Delta n(\theta = 90^o) = n_e - n_o \tag{2.21}$$

The crystal has positive or negative birefringence, if $n_o{<}n_e \; or \; n_o{>}n_e$, respectively, as illustrated in Fig. 2.3. The BPM can be realized in two types, Type I and Type I. In Type I, the driving fields have the same polarization and the generated field is orthogonally polarized compared to the driving field. In Type II, the driving fields are orthogonally polarized. To understand BPM, we consider SHG process in a positive uniaxial crystal with Type-I phase-matching. Figure 2.4 shows the propagation direction at an angle θ, where the extraordinary index for the fundamental wave at frequency, ω, is equal to the ordinary index for the second-harmonic wave at frequency, 2ω, thus compensating the dispersion and resulting in perfect phase-matching.

Depending upon the value of θ, BPM can also be catogorized into critical phase-matching, CPM ($\theta \neq 90^o$), and noncritical phase-matching, NCPM ($\theta = 90^o$). In CPM, the refractive index, n_e, and the phase velocity become dependent on angle, θ, leading to a reduction in the spatial overlap between the interacting ordinary and extraordinary polarized waves in the nonlinear crystal, thus limiting the interaction length of the nonlinear material. This

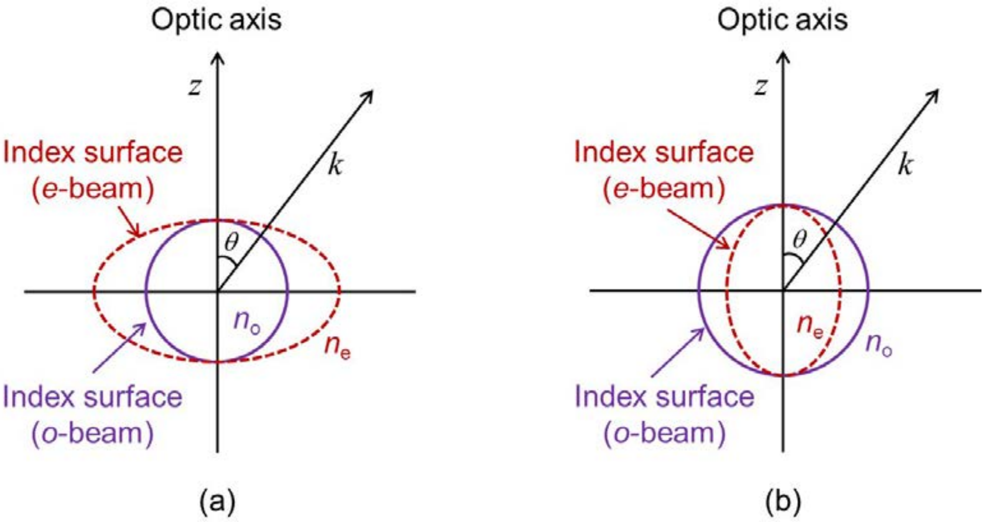

Figure 2.3: Index ellipsoids for (a) positive uniaxial crystals and (b) negative uniaxial crystals.

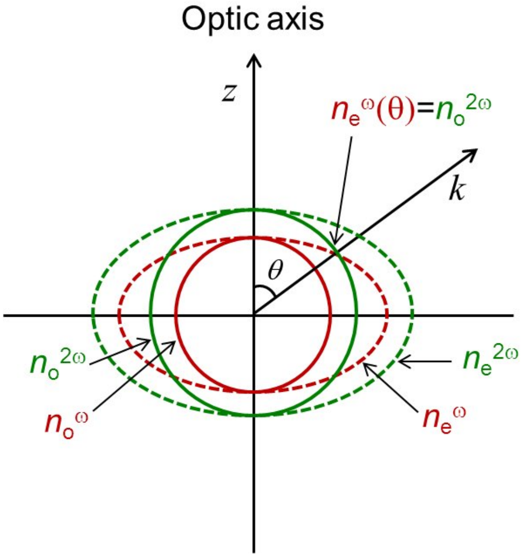

Figure 2.4: Illustration of birefringent phase-matching for SHG in uniaxial crystal.

phenomenon is known as spatial walk-off or Poynting vector walk-off. The spatial walk-off angle, ρ, can be represented as

$$tan(\rho) = -\frac{1}{n_e(\theta)}\frac{dn_e(\theta)}{d\theta} \tag{2.22}$$

In a biaxial crystal, the propagation direction of the wave is defined by two angles, polar (θ) and azimuthal (ϕ). For simplicity, it is conventional to consider the wave propagation in the xy, yz and xz principal planes. The two optic axes are taken to lie in the xz plane, and these make an angle, Ω, with the z-axis, as illustrated in Fig. 2.5.

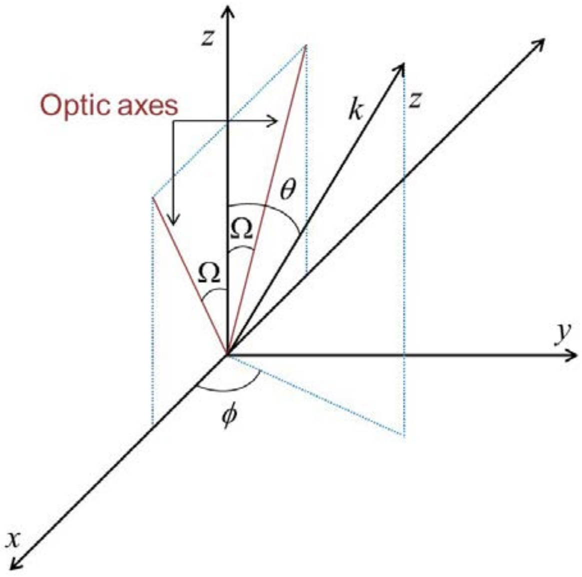

Figure 2.5: Schematic of wave propagation for biaxial crystal, in the crystal coordinate system.

The propagating wave is at angle θ with respect to the z-axis, and at ϕ with respect to the x-axis. In xy plane, $\theta = 90^o$, and ϕ varies from 0^o to 90^o, whereas in yz plane, $\phi = 90^o$, and θ varies from 0^o to 90^o. Considering $n_x < n_y < n_z$, where n_x, n_y and n_z are the principal values of the refractive indices, in xy plane,

$$n_o = n_z \tag{2.23}$$

$$n_e(\phi) = \frac{n_y(1 + tan^2\phi)^{1/2}}{[1 + (n_y/n_x)^2 tan^2\phi]^{1/2}} \tag{2.24}$$

and in yz plane,

$$n_o = n_x \tag{2.25}$$

$$n_e(\theta) = \frac{n_y(1 + tan^2\theta)^{1/2}}{[1 + (n_y/n_z)^2 tan^2\theta]^{1/2}} \tag{2.26}$$

2.5.2 Quasi-phase-matching

There are circumstances when the BPM technique, described in the previous section, are not suitable, such as when the material does not possess sufficient birefringence to compensate for the refractive index difference due to dispersion, or when a particular application requires nonlinear coefficient much larger than the off-diagonal tensor elements. Under these situations, an alternative technique know as quasi-phase-matching (QPM) can be used. Armstrong et al. were the first to suggest the QPM technique [4]. Unlike BPM, QPM is not perfect phase-matching. The idea of QPM is illustrated in Fig. 2.6(a). In the nonlinear crystal, after each coherence length, l_c, the sign of all the components of nonlinear susceptibility tensor is reversed. Thus, the polarization is shifted by 180^o after each coherence length, making the interacting waves propagate in phase along the propagation direction. The introduction of the additional phase is realized by modulating the nonlinear coefficient of the medium with a period $\Lambda = 2l_c$. The nature of this effect has been illustrated in Fig. 2.2(c). As evident, the build-up of output intensity is less rapid than that in the case of perfect phase-matching. Hence, QPM can result in lower conversion efficiency as the nonlinear coefficient is given by

$$d_m = \frac{2}{m\pi} d_{eff} \tag{2.27}$$

where m is referred as order of the QPM. However, QPM permits the use of the same polarization direction for all interacting waves, accessing the highest diagonal coefficients of the nonlinear tensor. As such, the conversion efficiency

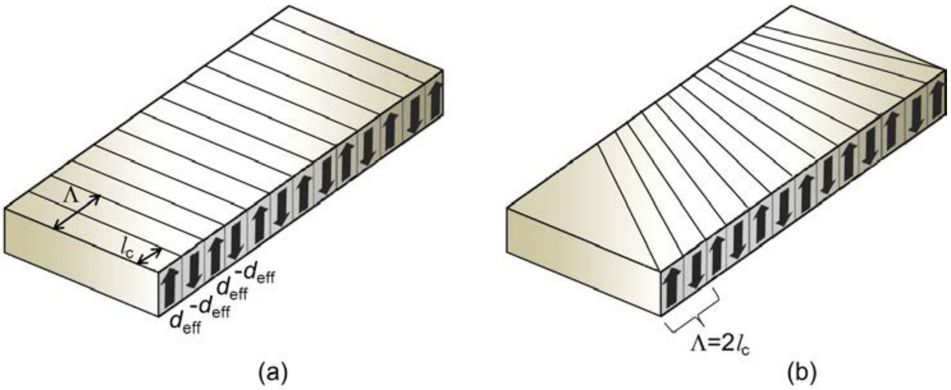

Figure 2.6: (a) Periodic inversion of the sign of the nonlinear coefficient, and (b) fanout grating structure, in a QPM nonlinear material.

in case of QPM technique can be significantly higher than that by BPM technique. Moreover, using NCPM configuration, the spatial walk-off between the interacting fields can be avoided. The most popular technique to fabricate quasi-phase-matched crystals is periodic reversal of the domains of ferroelectric materials such as $LiNbO_3$ and $LiTaO_3$. By applying a strong periodic electric field, the spontaneous electronic polarization of these materials can be inverted. This technique is known as periodic poling. The advancement in periodic poling technology also allows the fabrication of crystals in fanout grating structures, as shown in Fig. 2.6(b).

2.6 Second-harmonic and sum-frequency-generation

As shown in Fig. 2.1(a), sum-frequency-generation is the process where two photons at frequencies, ω_1 and ω_2, interact to generate an output photon at a frequency, ω_3. If the two input photons are at same frequency, ω, the output frequency is at the second-harmonic, 2ω, as illustrated in Fig. 2.1(b). For an efficient nonlinear process, optimum crystal length, and broad spectral and temperature acceptence bandwidths are important criteria [50, 52]. For the SHG process, the spectral acceptance bandwidth is given by

$$\Delta\lambda_{\omega} = \frac{0.4429\lambda_{\omega}}{l}\left|\frac{n_{2\omega}-n_{\omega}}{\lambda_{\omega}} + \frac{\partial n_{\omega}}{\partial\lambda_{\omega}} - \frac{1}{2}\frac{\partial n_{2\omega}}{\partial\lambda_{\omega}}\right|^{-1} \tag{2.28}$$

where λ_{ω} is the pump or fundamental wavelength, l is the length of the nonlinear crystal, n_{ω} and $n_{2\omega}$ are the refractive indices of the fundamental and the generated second-harmonic wave, respectively. The temperature acceptance bandwidth can be given by

$$\Delta T = \frac{0.4429\lambda_{\omega}}{l}\left|\frac{n_{2\omega}-n_{\omega}}{\partial T} + \alpha(n_{2\omega}-n_{\omega})\right|^{-1} \tag{2.29}$$

where α is the linear thermal expansion coefficient of the nonlinear crystal. For SHG, the conversion efficiency under plane-wave and undepleted pump approximation is given by

$$\begin{aligned}\eta_{SHG} &= \frac{P_{2\omega}(l)}{P_{\omega}(0)} = \eta^{o}_{SHG} sinc^{2}\left(\frac{\Delta kl}{2}\right) \\ \eta^{o}_{SHG} &= \frac{8\pi^{2}d^{2}_{eff}l^{2}I_{\omega}}{\epsilon_{0}n^{2}_{\omega}n_{2\omega}c\lambda^{2}_{\omega}}\end{aligned} \tag{2.30}$$

where P_{ω} is the fundamental power, $P_{2\omega}$ is the SHG power, and I_{ω} is the fundamental intensity. The phase-matching condition in the case of periodically-poled materials is attained by,

$$\Delta k = k_{2\omega} - k_{\omega} - \frac{2\pi}{\Lambda} \tag{2.31}$$

The SFG process exhibit similar behaviour, with the conversion efficiency under similar approximations represented as

$$\eta_{SFG} = \frac{P_{\omega_3}(l)}{P_{\omega_1}(0)} = \eta^o_{SFG} sinc^2\left(\frac{\Delta kl}{2}\right) \tag{2.32}$$
$$\eta^o_{SFG} = \frac{8\pi^2 d^2_{eff} l^2 I_{\omega_2}}{\epsilon_0 n_{\omega_1} n_{\omega_2} n_{\omega_3} c\lambda^2_{\omega_3}}$$

where P_{ω_1} and $I_{\omega_1}$are the fundamental power and the fundamental intensity, respectively, P_{ω_3} is the SFG power at SFG wavelength of λ_{ω_3}, and n_{ω_1}, n_{ω_2} and n_{ω_3} are the refractive indices of the interacting waves at frequencies ω_1, ω_2 and ω_3, respectively.

2.7 Optical parametric oscillator

As illustrated in Fig. 2.1(e), an optical parametric oscillator (OPO) essentially consists of a nonlinear medium enclosed by an optical resonator. It is a device based on three-wave interaction process, where a nonlinear material is pumped by an intense input pump field, to generate signal and idler output at macroscopic level, while satisfying energy conservation and phase-matching conditions [49, 53]. The signal and idler are initially generated by the process of parametric noise that corresponds to the spontaneous optical parametric generation. For attaining macroscopic amplification of the generated waves, positive feedback is necessary, that requires an optical oscillator. Thus, as in lasers, OPOs are operated in an oscillator configuration. The primary difference between the lasers and OPOs is that the optical gain in OPOs comes from the parametric amplification in the nonlinear crystal and not from the stimulated emission of population inversion. Unlike the laser, in the OPO there is no energy storage and the gain is only available in the presence of pump.

2.7.1 Parametric gain and amplification

Under phase-matching condition, the parametric noise is amplified during the propagation through the medium. The single-pass parametric gain in the nonlinear crystal is given by

$$G_s(L) = \frac{I_s(l)}{I_s(0)} - 1 = \Gamma^2 l^2 \frac{sinh^2[\Gamma^2 l^2 - (\frac{\Delta kl}{2})^2]^{1/2}}{[\Gamma^2 l^2 - (\frac{\Delta kl}{2})^2]} \tag{2.33}$$

where I_s is the signal field intensity, and Γ is the gain factor defined as

$$\Gamma^2 = \frac{8\pi^2 d_{eff}^2}{c\epsilon_0 n_p n_s n_i \lambda_s \lambda_i} I_p(0) \tag{2.34}$$

Here, I_p is the pump intensity, and n_p, n_s and n_i are the refractive indices of the pump, signal and idler at wavelengths λ_p, λ_s and λ_i, respectively. At degeneracy, when, $\lambda_i = \lambda_s = 2\lambda_p$, the gain factor can also be expressed in the form

$$\Gamma^2 = \frac{8\pi^2 d_{eff}^2}{c\epsilon_0 n_p n_0^2 \lambda_0^2} (1 - \delta^2) I_p(0) \tag{2.35}$$

where $\lambda_0 = 2\lambda_p$ is the degenerate wavelength, n_0 is the refractive index at degeneracy, assuming $n_0 \sim n_s \sim n_i$, and δ is the degeneracy factor. The parametric gain is maximum when, $\delta \sim 0$, and the gain decreases for operation away from degeneracy as $\delta \rightarrow 1$.

Under perfect phase-matching condition, by setting $\Delta k = 0$ in equation 2.33, the net single-pass signal gain reduces to

$$G_s(l) = sinh^2(\Gamma l) \tag{2.36}$$

which, for low gains ($\Gamma l \lesssim 1$), approximates to

$$G_s(l) \cong \Gamma^2 l^2 \tag{2.37}$$

and for high gains ($\Gamma l \gg 1$), reduces to

$$G_s(l) \cong \frac{1}{4} e^{2\Gamma l} \tag{2.38}$$

Hence, under the phase-matching condition, the single-pass signal gain has a quadratic dependence on Γ in the low-gain limit, whereas it increases exponentially with 2Γ in the high-gain limit.

2.7.2 Oscillator configurations

The losses in an OPO cavity primarily originate from the limited reflections of the cavity mirrors, in addition to the losses due to scattering, and absorption in the crystal. As such, while extracting the wave(s) of interest, the other waves are resonated inside the optical cavity. Depending on the number of waves resonating in the optical cavity, there are four major configurations, as illustrated in Fig. 2.7. In singly-resonant oscillator (SRO), one of the generated wave (signal or idler) is resonated, while the other is completely extracted from the cavity together with the undepleted pump. The doubly-resonant oscillator (DRO) resonates both the signal and idler, while the undepleted pump is extracted. In triply-resonant oscillator (TRO), all three waves are resonated. To enhance the pump in the cavity, another configuration known as pump-enhanced SRO (PE-SRO) is used, where one of the generated waves together with the pump is resonated inside the cavity.

The advantage of DROs, particularly in continuous-wave operation, where the pump intensity is low, is that the oscillation threshold pump power can be much lower as compared to that in the SRO. On the other hand, in spite of the high operation threshold of SROs, they provide single-frequency output with stable performance.

2.7.3 Steady-state threshold in cw OPOs

The determination of the oscillation threshold pump power, particularly under continuous-wave pumping, is an important factor. Considering plane-wave and

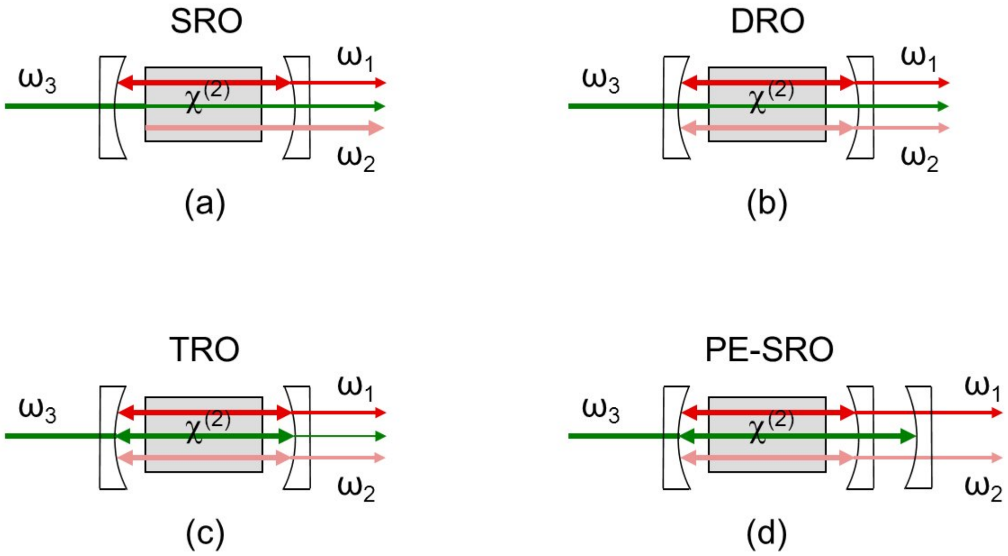

Figure 2.7: Cavity configurations for OPOs: (a) singly-resonant (SRO), (b) doubly-resonant (DRO), (c) triply-resonant (TRO), and (d) pump-enhanced (PE-SRO).

undepleted pump approximation, and assuming phase-matched interaction and single-pass of the pump, the threshold in SRO and DRO are presented here.

Singly-resonant oscillator

Considering the signal as the resonating wave, the pump intensity required to reach the oscillation threshold can be expresed as

$$I_{th} = \frac{\alpha_s c\epsilon_0 n_p n_s n_i \lambda_s \lambda_i}{8\pi^2 l^2 d_{eff}^2} \tag{2.39}$$

where α_s is the fractional round-trip power loss in the SRO for the signal wave.

Doubly-resonant oscillator

For DRO, the threshold pump intensity can be expressed as

$$I_{th} = \frac{\alpha_s c \epsilon_0 n_p n_s n_i \lambda_s \lambda_i}{8\pi^2 l^2 d_{eff}^2} \frac{\alpha_i}{4} \tag{2.40}$$

where α_s and α_i are the round-trip power loss of signal and idler wave, respectively, in the DRO cavity. The threshold of the DRO is reduced by a factor of $(\alpha_i/4)$ as compared to the SRO.

2.7.4 Wavelength tuning

The OPOs are well-known for their wide wavelength tunability. Under phase-matched condition, $\Delta k{\sim}0$, the phase-matching relation reduces to

$$2\pi \left(\frac{n_p}{\lambda_p} - \frac{n_s}{\lambda_s} - \frac{n_i}{\lambda_i} \right) = 0 \tag{2.41}$$

Thus, the wavelength tuning can be attained by changing any of the physical parameter that influences the refractive index of the nonlinear medium, while maintaining the phase-matched condition. The common parameters that are used are:

- Crystal angle (Angle tuning)
- Crystal temperature (Temperature tuning)
- Pump wavelength (Pump tuning)

For periodically-poled crystals, the quasi-phase-matched grating periods (Grating tuning) can also be used for tuning. Figure 2.8 shows typical wavelength tuning curves for a MgO:PPLN-based SRO, theoretically calculated from the relevent Sellmeier equations [54], where crystal temperature and the grating period are varied.

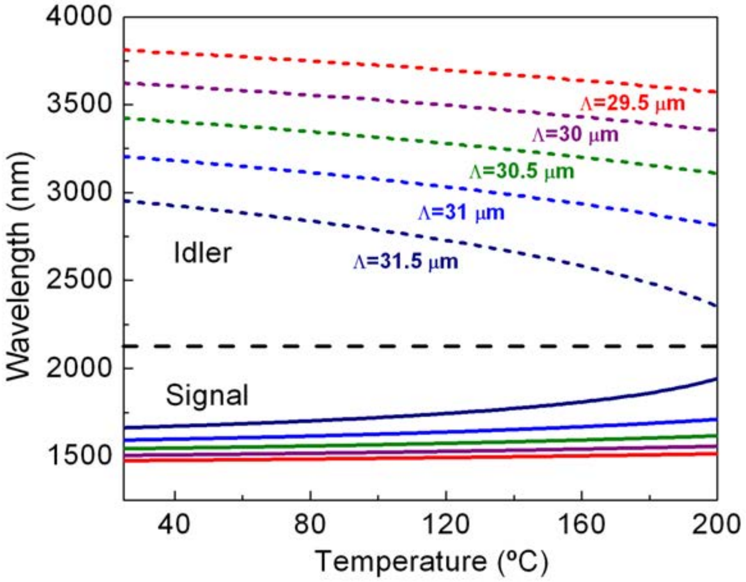

Figure 2.8: The tuning curves for signal and idler wavelengths for a 1-μm-pumped MgO:PPLN OPO.

2.8 Nonlinear materials

There are several important parameters that have to be taken into consideration when selecting a nonlinear crystal for developing an efficient frequency conversion source. For an OPO, the material of choice should be non-centrosymmetric, should have a broad transparency range at operating wavelengths, large nonlinearity, low spatial walk-off, a high optical damage threshold, good mechanical, chemical and thermal properties, phase-matching possibility in the wavelength range of interest, and availability in high optical quality, large size, and at a low cost. The nonlinear figure-of-merit, reperesented as

$$FOM = \frac{d_{eff}}{\sqrt{n_p n_s n_i}} \tag{2.42}$$

is another important factor, as it contains the physical parameters that are completely dependent upon the material. The larger the FOM, the better the material. For efficient transfer of energy to the generated waves, it is required that the material has a broad parametric gain bandwidth. The $sinc^2$ function describes the gain lineshape of the parametric medium, and the gain bandwidth of the nonlinear medium is defined by $|\Delta kl| \cong 2\pi$. The spectral ($\Delta\lambda_p$), angular ($\Delta\theta$) and temperature (ΔT) acceptance bandwidths are also the important parameters, as they indicates the maximum allowable pump linewidth, angular divergence and variation in temperature for efficient parametric generation [49]. The acceptance bandwidths are inversely proportional to the crystal length (l). This implies that shorter crystal lengths can tolerate larger deviations. For the attainment of maximum parametric gain and minimum OPO threshold, the use of nonlinear materials with large spectral, angular, and temperature acceptance bandwidths is advantageous.

Using a Yb-fiber laser at 1064 nm as the pump source, we performed SHG to generate output at 532 nm, in $LiTaO_3$ and $LiNbO_3$ crystals, in congruent and stoichiometric compositions, provided by HC photonics. The crystals are of equal lengths, l=10 mm. The pump beam was focussed at the centre of the crystals to beam waist radii of 32 μm, and the maximum available pump power, P_ω, was 27.8 W. Table 2.1 shows the various parameters of these nonlinear crystals, obtained from the measurements.

For a birefringent material under CPM condition, another factor to be considered is the spatial walk-off. The effective interaction length in the presence of walk-off is given by

$$l_{eff} = \frac{\sqrt{\pi}\omega_p}{\rho} \tag{2.43}$$

The effective length of the crystal can be increased by increasing the pump beam waist radius. However, efficient nonlinear optical processes require high pump intensity, and hence the pump beam waist needs to be well focused. As such, to achieve practical efficiencies, a good balance between the crystal length and beam radii must be maintained. Also, spatial walk-off can be overcome by using NCPM ($\theta = 90^o$).

Nonlinear crystal	**Max. SHG power (W)**	**Max. SHG efficiency (%)**	ΔT **(°C) @ P$_\omega$=9 °C**	ΔT **(°C) @ P$_\omega$=27.8 °C**	dT/dP_ω **(°C/W)**	**d$_{eff}$ (pm/V)**
VTE-SLT	2.58	9.37	3.49	3.04	-0.233	6.50
SLT	2.97	10.69	3.63	3.63	-0.033	6.87
SLT	2.83	10.23	3.51	3.46	-0.035	6.68
MCLT	1.60	5.75	3.53	3.06	-0.205	5.63
VTE-CLT	0.219	0.78	–	3.2	-0.120	1.80
SLN	2.42	10.84	2.63	1.52	-0.165	9.78

Table 2.1: Characterization of some nonlinear crystals. VTE-SLT: Vapor transport equilibration stoichiometric $LiTaO_3$, SLT: Stoichiometric $LiTaO_3$, MCLT: MgO-doped congruent $LiTaO_3$, VTE-CLT: Vapor transport equilibration congruent $LiTaO_3$, SLN: Stoichiometric $LiNbO_3$.

2.9 Cavity design

In addition to the proper choice of nonlinear crystal and the pump source, efficient operation of OPOs require a perfect resonator design. Figure 2.9 shows the typical cavity designs used for OPOs. The linear cavity, V-cavity and X-cavity are standing-wave cavities, while the ring cavity is a travelling-wave cavity. The pump beam is focused at the centre of the nonlinear crystal, and the mirrors used have radius of curvature to match the mode of the resonant wave to the pump mode. The standing-wave cavities offer the possibility of double-pass pumping to reduce the threshold in SROs. However, an optical isolator is required in such cases to avoid any back-reflection into the laser pump source. On the other hand, ring cavity has several advantages over other configurations, particularly for cw OPOs, which are more sensitive to losses. In the ring cavity, the single-pass of the resonating wave through the crystal for every round-trip reduces the losses due to material absorption and crystal coatings, which results in reduction of the threshold pump power. Additionally, it offers the possibility of introducing etalons for frequency selection, or suitable nonlinear crystals for intracavity frequency conversion, at the second beam waist of the cavity. For attaining optimum performance of an OPO, the confocal parameter of the pump beam, b_p, which is twice the Rayleigh range needs to be equal to that of the resonating beam, b_s ($b_p{\sim}b_s$). To achieve this, the focal point of the pump needs to be at the same position (at the center of the nonlinear crystal) as the focal point of the resonating beam. To design the above mentioned configurations, we used ABCD matrix, and calculated the effect of optical elements on the parameters of a Gaussian beam [55,56]. Using the Gaussian beam transformation matrices, the signal waist can be calculated at any position in the cavity.

The beam waist, $w(z)$, and the radius of curvature, $R(z)$, of a Gaussian

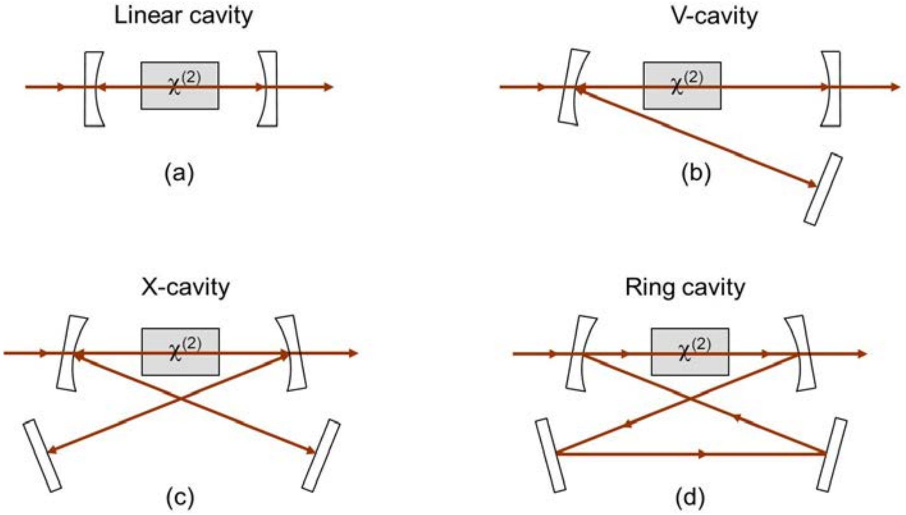

Figure 2.9: Various OPO cavity designs: (a) Linear cavity, (b) V-cavity, (c) X-cavity, (d) Ring cavity.

beam propagating in a straight line along z-axis are given by,

$$w(z) = w_0^2 \left(1 + \frac{z^2}{z_0^2}\right) \tag{2.44}$$

and

$$R(z) = z \left(1 + \frac{z_0^2}{z^2}\right) \tag{2.45}$$

where w_0 is the minimum beam waist at z=0, and z_0=$\pi n w_0^2/\lambda$ is known as Rayleigh range, n is the refractive index, and λ is the wavelength of the Gaussian beam. The confocal parameter is given by b=2z_0. Gaussian beam at a distance z can be expressed using a complex beam parameter, given as

$$q(z) = z - iz_0 \tag{2.46}$$

The complex parameter, $q(z)$, contains information on $w(z)$ and $R(z)$ both, and is expressed as

$$\frac{1}{q(z)} = \frac{1}{R(z)} - i\frac{\lambda}{\pi n w^2(z)} \tag{2.47}$$

The ABCD matrices, also know as ray matrices, relate the complex beam

Propagation over a distance, d	$\begin{pmatrix} 1 & d \\ 0 & 1 \end{pmatrix}$
Refraction at a flat surface separating two media of index, n_1 and n_2	$\begin{pmatrix} 1 & 0 \\ 0 & \frac{n_1}{n_2} \end{pmatrix}$
Thin lens of focal length, f	$\begin{pmatrix} 1 & 0 \\ -\frac{1}{f} & 0 \end{pmatrix}$

Table 2.2: Ray matrices

parameter, q_2, at a plane 2 to the value, q_1, at plane 1 as

$$q_2 = \frac{Aq_1 + B}{Cq_1 + D} \tag{2.48}$$

The general form of the ABCD matrix is given by

$$M = \begin{pmatrix} A & B \\ C & D \end{pmatrix} \tag{2.49}$$

where A, B, C, D are the ray matrix elements. The ray matrix analysis is a convenient way to describe the ray propagation through different media, such as lenses, nonlinear crystals and mirrors, as a sequence of events that can be combined by matrix multiplication to yield a final result. Some useful ray matrices are shown in the Table 2.2.

Using these ray matrices and satisfying the condition for stability of the cavity, -1$\leq(A + D)/2\leq$1, we can calculate the beam waist radius, starting from center of the nonlinear crystal, and design a stable cavity. The typical cavity design plot for ring configuration is shown in Fig. 2.10, from which the various design parameters such as the distance between the cavity mirrors and optimum position of the crystal can be estimated.

2.10 Active mode-locking

When the oscillating modes inside an optical oscillator, comprising a suitable gain medium, are forced to maintain equal frequency spacing with a fixed phase

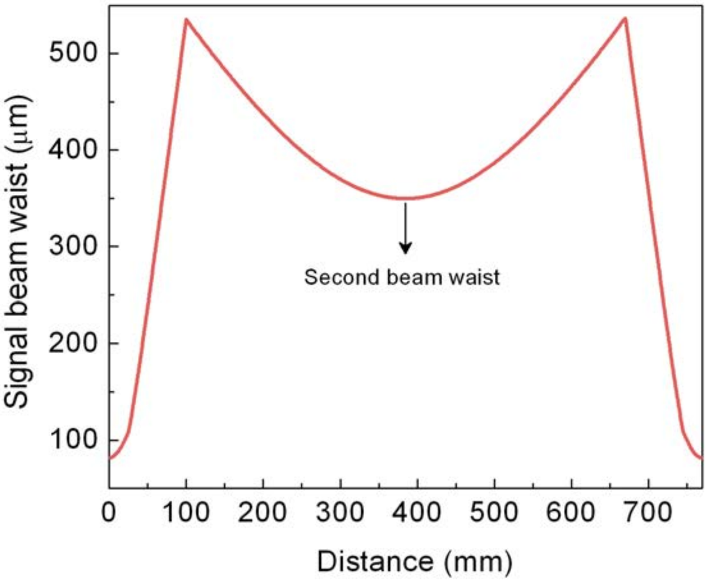

Figure 2.10: Signal beam waist along the ring cavity.

relationship to each other, the optical oscillator is said to be mode-locked. For generating short optical pulses, the mode-locking of laser oscillators are commonly used [57, 58]. However, as described in section 2.7.4, OPOs are the potential candidate to increase the wavelength tunability. For OPOs, it has been shown earlier [59] that synchronous pumping is the only option for generating ultrashort pulses, because a parametric device is not able to store the pump energy for use at later times. However, with the advent of QPM materials, it is now possible to actively mode-lock OPOs. It has been shown that there is a strong analogy between laser and OPO mode-locking, when the pump depletion is negligible [60]. The basic idea is to employ amplitude modulation or phase modulation. Here, we consider frequency modulation, as the work presented in this thesis is based on this method.

Treating the mode-locking process in the time domain, the optical pulse in the Gaussian form is given by [61]

$$E(t) = E_0 e^{-At^2} e^{\left[j\left(\omega t + Bt^2\right)\right]} \tag{2.50}$$

where A determines the Gaussian envelope of the pulse and jBt is a linear frequency shift during the pulse chirp. The product of pulse duration, $\Delta\tau$, and bandwidth, Δf, for the Gaussian pulse is given by

$$\Delta\tau\Delta f = \left(\frac{2ln2}{\pi}\right)\sqrt{1 + \left(\frac{B}{A}\right)^2} \tag{2.51}$$

For $|B| = A$, $\Delta\tau\Delta f = 0.626$. The pulse width is proportional to two parameters of the phase modulator, the modulation index, μ_m, and the modulation frequency, ν_m. This can be expressed as [62]

$$\Delta\tau \propto \left(\frac{1}{\mu_m}\right)^{\frac{1}{4}} \left(\frac{1}{\nu_m}\right)^{\frac{1}{2}} \tag{2.52}$$

The phase modulator drive power, P_m, varies the modulation index as,

$$\mu_m = \sqrt{P_m} \tag{2.53}$$

Hence, from equation 2.52,

$$\Delta\tau \propto P_m^{-\frac{1}{8}} \tag{2.54}$$

Equations 2.52 and 2.54 show that the pulses shorten very slowly with increased modulation drive, while the fastest way of pulse shortening is to increase the modulation frequency. The dependence of peak optical power, P_{pk}, on average optical power, P_{avg}, and on μ_m and ν_m is given by [62]

$$P_{pk} \propto \frac{P_{avg}\mu_m^{\frac{1}{4}}}{\nu_m^{\frac{1}{2}}} \tag{2.55}$$

In the frequency domain, the modulation index is given by [63]

$$\mu_m = \frac{\zeta\Delta\Omega}{\pi\Delta\nu} \tag{2.56}$$

where $\Delta\Omega = c/2L$ is the frequency separation between two modes, c is the speed of light in vacuum, L is the length of the cavity, ζ is single-pass phase retardation, and $\Delta\nu$ is the modulation frequency detuning, given by $\Delta\nu = \nu_m - \Delta\Omega$.

Chapter 3

High-power, cw, fiber-based source at 970 nm

This chapter constitutes the following publication:

1. *13.1 W, high-beam-quality, narrow-linewidth continuous-wave fiber-based source at 970 nm*
   K. Devi, S. Chaitanya Kumar, and M. Ebrahim-Zadeh
   Opt. Express **19**, 11631-11637 (2011)

3.1 Motivation

High-power, continuous-wave (cw) laser sources at 970 nm are of considerable interest for a variety of scientific and technological applications including pumping of solid-state and fiber lasers, spectroscopic detection of ozone, water-vapor, and CO_2 in the atmosphere, and various medical applications [64–67]. In particular, a narrow-linewidth source at 970 nm offers potential impact for bio-sensing applications [67]. Such sources could also be deployed in combination with nonlinear frequency up-conversion schemes such as second-harmonic-generation (SHG) to provide high-power cw blue radiation to replace bulky water-cooled argon-ion lasers, which inherently operate in multiple longitudinal modes [68]. For many such applications, a high spatial beam quality in addition to high output power is imperative. To date, the possible sources of 970 nm radiation are high-power diode lasers, but their beam quality still remains an important limitation [69, 70]. The Ti:sapphire laser can provide output radiation at 970 nm, but the low gain far from the emission peak results in low output power [71]. Optically-pumped semiconductor lasers are another alternative source of 970 nm radiation, but limited progress has been achieved in this direction so far [72]. High-power, cw, ytterbium (Yb)-doped photonic crystal fiber lasers have been recently demonstrated near 980 nm, but it has been shown that the beam quality factor degrades with the increase in output power [73]. Although these sources provide high conversion efficiencies and have proved highly effective [70, 72, 73], the attainment of good beam quality with good M^2 factor and narrow linewidth together with high-power at 970 nm, and in a simple design, still remains a challenge. It is, thus, desirable to explore alternative techniques for the generation of cw radiation at 970 nm in a simple, compact and cost-effective design to provide a practical high-power source with good spatial beam quality, mandatory requirements for many applications.

Advances in cw fiber lasers together with the development of quasi-phase-matched (QPM) ferroelectric materials provide a unique opportunity for the realization of high-power cw sources in new spectral regions using nonlinear frequency conversion techniques. In a particularly simple, compact and practical scheme, we recently reported direct single-pass (SP) SHG of cw Yb-fiber lasers in MgO-doped periodically-poled stoichiometric $LiTaO_3$ (MgO:sPPLT), providing 13 W of green radiation at an unprecedented conversion efficiency as high as 56% [44, 74]. With progress in cw thulium (Tm)-fiber laser technology near 2 μm, such techniques can now be effectively exploited for the generation of high-power cw radiation near 1 μm at high efficiency and in good beam quality. In the pulsed regime, Frith et al. [75] demonstrated frequency-doubling of gain-switched Tm-doped fiber laser at 1908 nm in periodically-poled $LiNbO_3$ (PPLN), generating $\sim$1 W of average power at 954 nm with 60% conversion efficiency.

In this chapter, we demonstrate the generation of multiwatt cw radiation at 970 nm by exploiting SP-SHG of a high-power cw Tm-fiber laser in combination with PPLN as the doubling crystal. Using a 40-mm crystal, we generate an output power of 13.1 W at 970 nm with a SP-SHG conversion efficiency of 32.7%. The output at 970 nm is in a TEM_{00} spatial mode with $M^2<1.6$ and exhibits narrow linewidth with passive power stability better than 1.4% (1σ value) over 1 hour. To the best of our knowledge, this is the first demonstration of SHG of cw Tm-fiber laser, which provides a compact, practical, and efficient source of high-power radiation at 970 nm in high beam quality and simplified design, and with competitive performance over alternative cw sources in this wavelength range.

3.2 Experimental setup

The schematic of the experimental setup is shown in Fig. 3.1. The fundamental source is a cw Tm-fiber laser (IPG Photonics, TLR-50-1940-LP), delivering up to 44 W of output power at 1940 nm in a linearly-polarized beam with a quality factor of $M^2=1.2$ and a measured linewidth of $\Delta\lambda\sim0.5$ nm. A Faraday isolator with an isolation of $\sim$23 dB is used at the output end of the fiber to prevent back-reflection into the laser. The frequency stability of the fiber laser at the maximum power is recorded to be better than 3.3 GHz over 2 hours. The nonlinear crystal is 40-mm-long, 11.5-mm-wide, 1-mm-thick, undoped PPLN sample with multiple gratings, ranging in period from $\Lambda=25.5$ to $\Lambda=28.7$ μm. The calculated spectral acceptance bandwidth of the PPLN crystal for SHG at

1940 nm is 3.52 nm.cm, resulting in 0.88 nm for the 40 mm interaction length used in this experiment [52]. This value is larger than the Tm-fiber laser fundamental linewidth, ensuring efficient SHG to 970 nm. The reflectivity of the crystal input face at 1940 nm is experimentally measured to be $R<6\%$, resulting in a small input loss at the fundamental. The crystal is housed in an oven with a stability of ± 0.1 ^{o}C, which can be tuned from room temperature to 200 ^{o}C. The fundamental beam is focused at the center of the crystal using a CaF_2 focusing lens. Although a fundamental power of up to 44 W is available at the output of the fiber laser, due to non-optimized optics used to deliver the pump beam, the maximum power at the input of the crystal is 40 W. We used the Λ=28.2 μm grating period only, as it is quasi-phase-matched for SHG at 970 nm at a temperature of 93.8 ^{o}C. A dichroic mirror ($R>99.8\%$ @ 1940 nm and $T>86\%$ @ 970 nm), is used to separate the unconverted fundamental from the second-harmonic output beam.

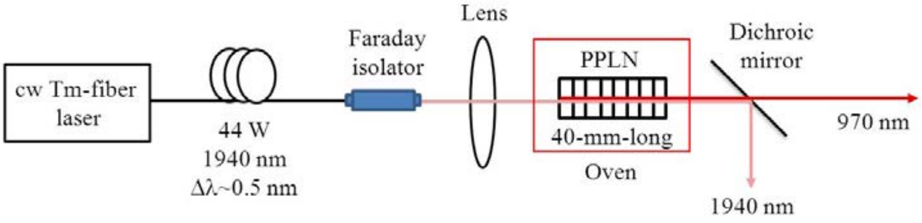

Figure 3.1: Schematic of the experimental setup.

3.3 Results and discussion

3.3.1 Optimization of the SHG operation

For the attainment of the highest SHG efficiency, we studied different spatial mode-matching conditions. Using lenses of different focal lengths, we focused the fundamental beam to waist radii of w_o~55.5, 45, 37.5, and 30.5 μm at the center of the crystal, corresponding to confocal focusing parameters of

$\xi = l/b$=1.88, 2.86, 4.12 and 6.23, respectively [76]. Here, l is the length of the crystal and b is the confocal parameter, which is twice the Rayleigh range. Figure 3.2 shows the maximum SHG efficiency achieved, at the maximum input fundamental power of 40 W, as a function of ξ. As evident, the SHG efficiency increases with the confocal focusing parameter, reaching as high as 32.7% at $\xi \sim 2.86$. Further increase in ξ value results in the drop in SHG efficiency. It is interesting to note that at $\xi \sim 2.86$, the maximum efficiency is achieved, which is almost equal to optimum focusing parameter, $\xi \sim 2.84$, predicted by Boyd and Kleinman in the cw limit [76].

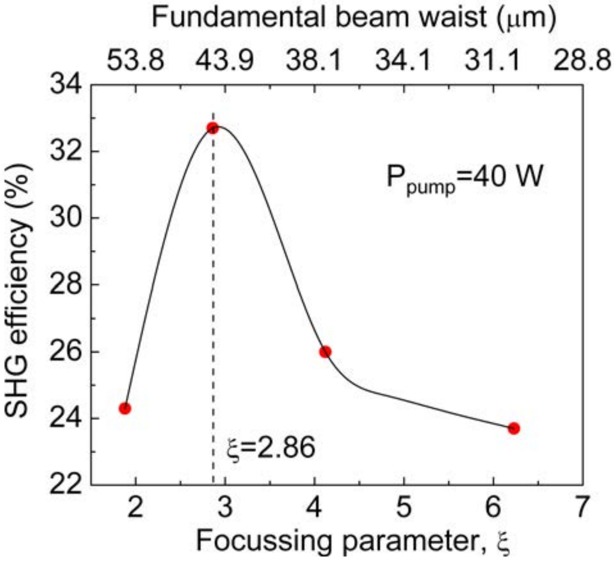

Figure 3.2: SHG efficiency at maximum fundamental power, as a function of focusing parameter, $\xi = l/b$.

3.3.2 Variation in phase-matching temperature with beam waist

At maximum fundamental power of 40 W, we recorded the phase-matching temperature, T_{QPM}, as a function of ξ, as shown in Fig. 3.3(a). As evident, the phase-matching temperature decreases with increase in ξ and has a steep fall towards tighter focusing. This may be attributed to the thermal effects arising from the tighter focusing of pump beam in the crystal, resulting in increase of thermal load, hence requiring a decrease in the required external heat applied to the crystal to achieve phase-matching. Another possible reason could be the increase in angular divergence of the beam with tighter focusing, which results in the propagation of the divergent components of the fundamental beam over longer grating periods, resulting in a shift in the peak phase-matching temperature. We calculated the propagation length of the divergent components, and the corresponding change in phase-matching temperature, for a propagation distance corresponding to grating period of Λ=28.2 μm along the crystal, as a function of beam waist radius. The results are shown in Fig. 3.3(b). It is found that under loose focusing (w_o~55.5 μm), the most divergent components of the fundamental beam propagate over an increased grating period of 28.20175 μm, while for tight focusing (w_o~30.5 μm) the increased grating period for the most divergent components is 28.20575 μm. Therefore, in reducing the beam waist from w_o~55.5 μm to w_o~30.5 μm, the grating period for the most divergent components increases by 4 nm, resulting in an average decrease in phase-matching temperature of the crystal with increased divergence and tighter focusing, as observed in Fig. 3.3(a). Using a wavemeter (Bristol, 721B-IR, absolute accuracy of 1 ppm), we measured the central wavelength (λ_ω) of the fundamental beam at 40 W to be λ_ω=1941.5 nm. Figure 3.3(c) shows the variation of theoretical predicted values of phase-matching temperature with focusing parameter, ξ, calculated for a single-frequency fundamental, using relevant Sellmeiers equation [77]. The theoretical T_{QPM} curve shows the same behavior as that of the experimental curve of Fig. 3.3(a).

To avoid any thermal contribution, we further measured the phase-matching temperatures for different beam waists, at low fundamental power. The results are shown in Fig. 3.3(d), where it is observed that at an input power of ~1 W, where thermal effects are negligible, the phase-matching temperature increases with loose focusing, as also seen for high fundamental power (Fig. 3.3(a)). With negligible contribution from thermal effects, the change in T_{QPM}

is attributed mainly to the fundamental beam divergence in the crystal.

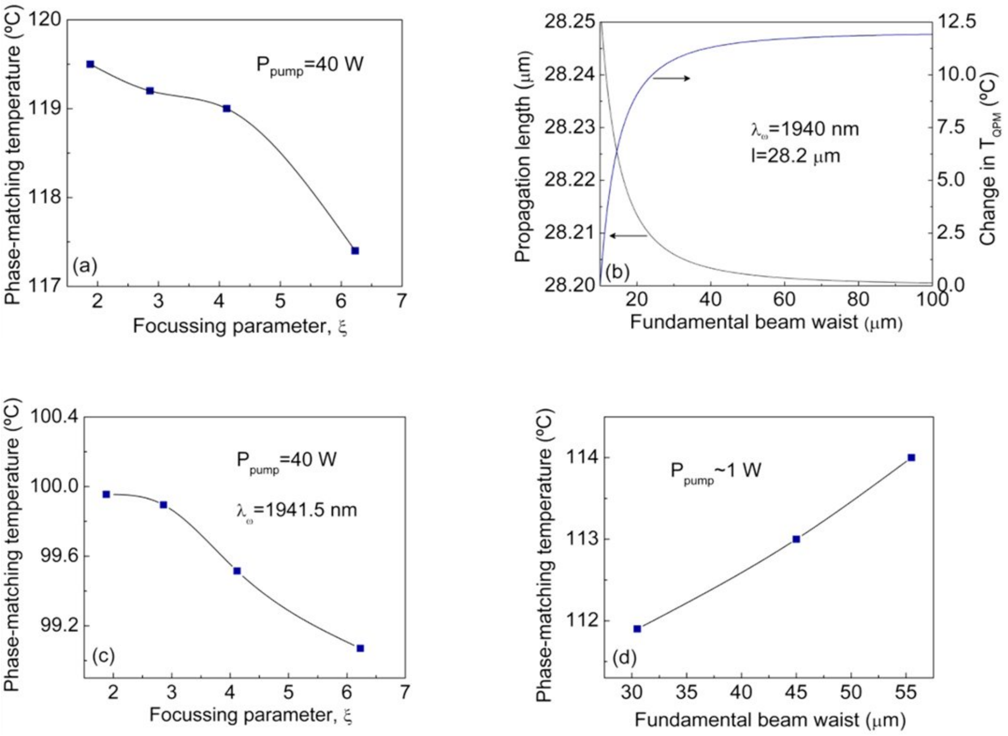

Figure 3.3: (a) Phase-matching temperature at maximum fundamental power, as a function of focusing parameter, ξ. (b) Theoretically calculated propagation length for divergent components and the corresponding change in phase-matching temperature, as a function of beam waist radius. (c) Theoretically calculated phase-matching temperature, as a function of focusing parameter, ξ. (d) Phase-matching temperature under different focusing conditions, at pump power of ∼1W.

3.3.3 Variation in phase-matching temperature with pumping level

Figure 3.4(a) shows the phase-matching temperature as a function of fundamental power for w_o∼45 μm (ξ∼2.86), where we observe a rise in phase-matching temperature with the increase in fundamental power. We obtain T_{QPM}∼112 ^{o}C at 0.8 W and 119.5 ^{o}C at 40 W, corresponding to a difference in phase-matching temperature of 7.5 ^{o}C. We measured the central wavelength of the fundamental output at different power levels using the wavemeter and found that the peak wavelength shifts towards the longer value with the rise in fundamental power. For example, λ_ω=1939.8 nm at ~1 W, and 1941.5 nm at ~40 W of fundamental power, which corresponds to a change of 1.7 nm in central wavelength. We theoretically calculated the phase-matching temperature as a function of fundamental wavelength considering negligible thermal effects [77]. As seen in Fig. 3.4(b), an increase in the fundamental wavelength by 1.7 nm corresponds to an increase of 7.4 ^{o}C in phase-matching temperature, thus confirming the observed rise in the phase-matching temperature with the increase in fundamental power.

3.3.4 Temperature acceptance bandwidth

To characterize the crystal under different focusing conditions, we measured the temperature acceptance bandwidths for different beam waists. The measurements were performed at low fundamental power, in order to avoid any thermal contributions. Figure 3.5(a) shows the result for optimum focusing (w_o~45 μm), together with the $sinc^2$ fit, at a fundamental power of ~1 W. The measured full-width-half-maximum (FWHM) temperature acceptance bandwidth (ΔT) is found to be 5.9 ^{o}C at T_{QPM}=113 ^{o}C. This is larger than the theoretical value of ΔT=3.8 ^{o}C at T_{QPM}=93.8 ^{o}C for the 40-mm crystal, which has been calculated for a single-frequency fundamental in plane-wave approximation without focusing, using the relevant Sellmeier equations [77]. The discrepancy between the experimental and theoretical value of ΔT could be in part due to the finite bandwidth of the fundamental ($\Delta\lambda$~0.5 nm), while the discrepancy in the value of T_{QPM} could be due to possible non-uniformity in the grating period along the crystal length. The difference between the experimental and theoretical values of ΔT could also in a large part be attributed to the focusing of the fundamental beam. As noted in section 3.3.2, this can give rise to an average increase in the grating period for all spatial components, which results in a decrease in the peak phase-matching tempera-

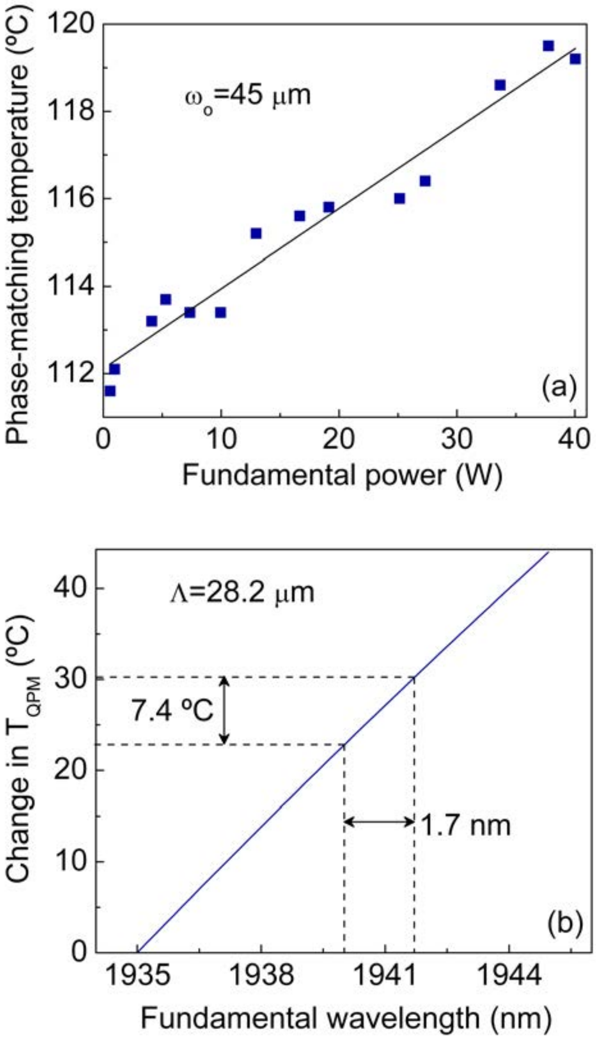

Figure 3.4: (a) Phase-matching temperature versus fundamental power. (b) Theoretically calculated change in phase-matching temperature versus fundamental wavelength for the grating period of Λ=28.2 μm.

ture, T_{QPM}, as well as a broadening of the phase-matching bandwidth towards lower temperatures, resulting in an increase in the experimental value of ΔT.

At the input power of ~1 W, we measured the variation of the FWHM temperature acceptance bandwidth as a function of fundamental beam waist radius. It is clear from Fig. 3.5(b) that for tighter pump focusing, the temperature acceptance bandwidth increases, as predicted. On the other hand, we also theoretically calculated the temperature acceptance bandwidth of the 40-mm-long PPLN crystal as a function of phase-matching temperature, in the plane-wave limit in the absence of focusing, and confirmed an increase in ΔT with the decrease in phase-matching temperature [52]. Therefore, the inherent variation of ΔT and T_{QPM} in the plane-wave limit combined with the focusing effects lead to the observed behavior in Fig. 3.3(d) and Fig. 3.5(b).

3.3.5 SHG power scaling and stability

The variation of SHG power and the corresponding efficiency up to the maximum available fundamental power for ξ~2.86 is shown in Fig. 3.6. We obtained 13.1 W of SHG power at 970 nm for 40 W of input power to the crystal, representing a single-pass efficiency of 32.7%. As seen in Fig. 3.6, the SHG power has a quadratic dependence on the fundamental power up to 18.5 W, beyond which it increases linearly, implying saturation of SHG efficiency at higher power. This can be attributed to pump depletion, back-conversion and thermal de-phasing effects in the PPLN crystal. However, we confirmed the role of thermal effects to be negligible, by performing power scaling measurements with tight focusing at w_o~37.5 μm (ξ=4.12) under quasi-cw condition. This measurement was performed by chopping the beam at 530 Hz with a duty cycle of 5%, and then comparing the results with that under cw condition. In both the cases, we found the SHG efficiency saturation at higher power, with a maximum efficiency of ~26%. Using the slope of the generated SHG power

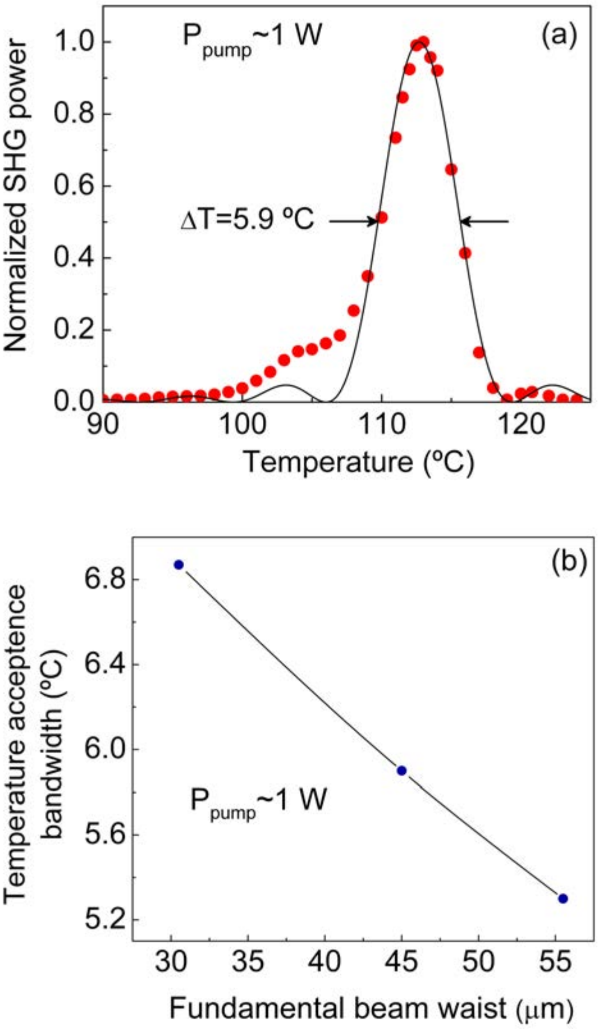

Figure 3.5: (a) Temperature phase-matching curve for SHG at w_o~45 μm, and (b) temperature acceptance bandwidth under different focusing conditions. Pump power is ~1 W.

versus square of the fundamental power curve, we also calculated the effective nonlinear coefficient for our PPLN crystal at 1940 nm wavelength [50], which we found to be d_{eff}~13.6 pm/V. Similar d_{eff} values were obtained from measurements at different beam waists and under quasi-cw condition.

We measured the power stability near the maximum SHG power at the fundamental power of 40 W. The result is shown in Fig. 3.7(a), where we obtained a passive stability better than 1.4% (1σ value) over 1 hour, without any precautions. The SHG power fluctuation is mainly attributed to the changes in the laboratory environment and also to some extent to the fluctuations in the input pump power with 0.9% (1σ value) over 1 hour, as seen in Fig. 3.7(b). Improved thermal and mechanical isolation of the system with proper temperature control and increased pump power stability can further enhance the SHG power stability.

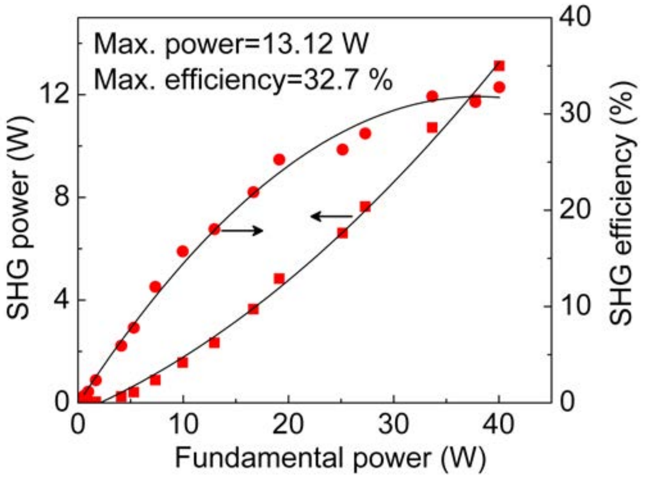

Figure 3.6: SHG power and the corresponding conversion efficiency as a function of incident fundamental power at w_o~45 μm.

3.3.6 SHG single-frequency operation and beam quality

We also recorded the spectrum of the generated SHG output at maximum power and found the linewidth ($\Delta\lambda_{2\omega}$) below 0.3 nm, as shown in Fig. 3.8,

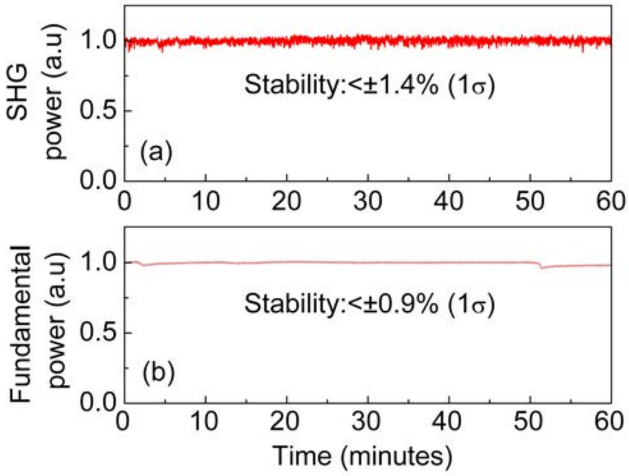

Figure 3.7: Time trace at maximum power of (a) generated SHG output, and (b) input fundamental over 1 hour.

limited by the resolution of our spectrum analyzer. The generated second-harmonic linewidth is thus narrower than that of the fundamental, as expected.

The far-field energy distribution of the SHG beam at maximum power together with the intensity profile is shown in Fig. 3.9. The slight asymmetry seen in the beam profile is due to the small tilt angle of the lens and separation mirror from the normal incidence. Using a f=100 mm focal length lens and a scanning beam profiler, the beam quality factor of the SHG beam at maximum power was measured to be ${M_x}^2{\sim}1.43$ and ${M_y}^2{\sim}1.6$, confirming the TEM$_{00}$ spatial mode.

We did not observe any photorefractive damage in the PPLN crystal up to the maximum SHG power, as evident from the output power stability and beam quality.

3.4 Conclusions

In conclusion, we have demonstrated, for the first time, efficient SP-SHG of a cw Tm-fiber laser, providing multiwatt cw radiation at 970 nm at high

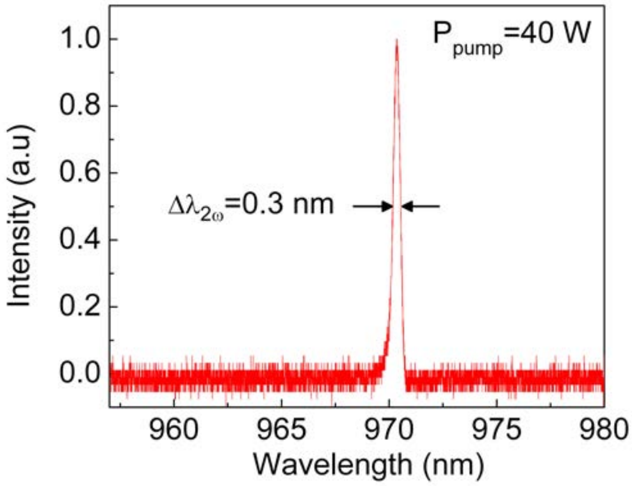

Figure 3.8: Spectrum of SHG output at maximum power.

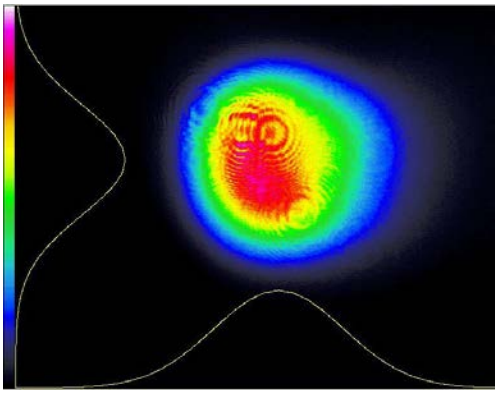

Figure 3.9: Far-field TEM_{00} energy distribution of the generated SHG beam. The thin curves are the intensity profiles along the two orthogonal axes.

efficiency, in narrow linewidth and high beam quality, and with good stability. By deploying a 40-mm-long PPLN crystal, we have generated 13.1 W of cw output power at 970 nm at single-pass conversion efficiency as high as 32.7%. The SHG output has a linewidth below 0.3 nm with a power stability better than 1.4% (1σ value) over 1 hour, and has a TEM_{00} beam profile with $M^2<1.6$. The absence of thermal effects suggest the possibility of further increase in cw SP-SHG output power and efficiency by using longer crystals, higher pump powers, and narrower fundamental linewidths. The exploitation of multicrystal scheme using several PPLN crystals in a cascade [44] could also lead to further increases in SP-SHG efficiency to >50%, providing >20 W of cw output power at 970 nm. The demonstrated fiber-based device offers a viable, compact and practical source of high-power, linearly-polarized, narrow-linewidth, and high-beam-quality cw radiation at 970 nm, with competitive performance over alternative sources in this wavelength range, and offering promise for a variety of applications.

Chapter 4

Interferometrically output-coupled cw SRO

This chapter constitutes the following publication:

1. *Antiresonant ring output-coupled continuous-wave optical parametric oscillator*
   K. Devi, S. Chaitanya Kumar, A. Esteban-Martin,
   and M. Ebrahim-Zadeh
   Opt. Express **20**, 19313-19321 (2012)

4.1 Motivation

Continuous-wave (cw) optical parametric oscillators (OPOs) in singly-resonant oscillator (SRO) configuration are now firmly established as viable sources of tunable high-power coherent radiation [5], nearly two decades after their first demonstration [30]. Due to the substantially lower intensities available from cw pump lasers, resulting in lower nonlinear gain and high oscillation threshold, the development of cw OPOs in SRO design remained particularly challenging for many years. However, with the advent of quasi-phase-matched (QPM) nonlinear materials, together with advances in high-power pump sources, particularly fiber lasers, cw SROs with wide tuning range and high output power have been realized, covering spectral regions from the visible to mid-infrared [41, 46, 78–82]. The high optical nonlinearity together with long interaction lengths and noncritical phase-matching in QPM materials has enabled operation of cw SROs at practical pump power thresholds (watt-level) and elevated output power levels (>10 W) [41, 81]. Operation of cw SROs based on QPM materials is now sufficiently robust that for the attainment of highest extracted power, limited output coupling of the resonant signal wave can be tolerated [83]. This enables substantial enhancement not only in the total (signal plus idler) output power and external efficiency, but also in the usable tuning range. At the same time, the use for signal output coupling has been shown to be imperative at increased pump powers, where the high intracavity signal intensities can lead to significant thermal loading in the nonlinear crystal, limiting conversion efficiency and degrading output power, wavelength stability and beam quality [39, 84, 85]. As such, the deployment of signal output coupling represents an important strategy to achieve optimum performance in cw SROs with regard to several important operating parameters. As in laser oscillators, the conventional technique for the attainment of output coupling in cw SROs relies on the use of different output coupler (OC) mirrors with discrete transmission values at the resonant wavelength [41]. However, this approach requires the search for different OC mirrors to obtain the optimum value of output coupling. Moreover, under different cw SRO operating conditions, such as the resonant wavelength and pumping level, the optimum value of output coupling can change, making absolute optimization of output power at all wavelengths and under all operating conditions difficult, costly, and time-consuming.

Recently, an alternative new approach for absolute optimization of extracted power from optical oscillators was demonstrated using an antiresonant ring (ARR) interferometer as an output coupler, and the concept was realized for the first time in a femtosecond OPO [86]. Later, the technique was extended to traveling-wave oscillators, where optimum output coupling in a picosecond OPO configured in a ring resonator was demonstrated [87]. The ARR interferometer essentially consists of two highly reflecting mirrors (M), and a beam-splitter (BS) with a transmittance, T, and reflectance, R, as shown in Fig. 4.1. The BS splits the incident optical beam (E_{in}) into clockwise (dotted) and anticlockwise (solid) beams. These counter-propagating beams, after propagation inside the ring, are then again transmitted and reflected at the BS. The new pairs of fields, (${E_r}^{ccw}$;${E_t}^{cw}$) and (${E_t}^{ccw}$;${E_r}^{cw}$), thus formed, interfere, and give rise to reflected, $E_r={E_r}^{ccw}+{E_t}^{cw}$, and transmitted, $E_t={E_t}^{ccw}+{E_r}^{cw}$, output fields. The power reflected back is given by $R_{ARR}=4RT$, while the power transmitted out of the ARR is given by $T_{ARR} = |R - T|^2$, implying that the reflected fields from the ARR and the transmitted fields through the ARR interfere constructively and destructively, respectively. The ARR output coupling technique exploits the ability to adjust the T:R ratio of the BS simply by varying the angle of incidence (θ_{BS}) on the BS. This results in a change in the transmitted power, T_{ARR}, from the ARR, which can then be used as a means to vary the optical feedback into an optical oscillator incorporating the ARR.

In this chapter, we demonstrate, for the first time, the integration of an ARR interferometer into a cw SRO, for the attainment of optimum output coupling. While the technique has been previously demonstrated in pulsed optical oscillators [86, 87], where high levels of output coupling (>50%) can be readily supported, the integration of such an ARR into a cw SRO can be challenging due to the low tolerance of cw SROs to loss and output coupling (typically <5%). We demonstrate that despite the high sensitivity to loss and output coupling, the ARR offers a unique and practical approach to achieve

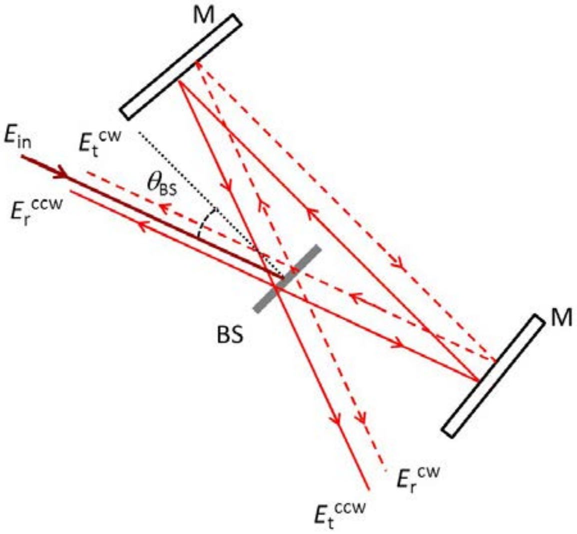

Figure 4.1: Antiresonant ring interferometer.

fine, adjustable, and in situ optimization of output power from cw SROs.

4.2 ARR output-coupled cw SRO

4.2.1 Experimental setup

The schematic of the experimental setup is shown in Fig. 4.2. The fundamental pump source is a cw Yb-fiber laser (IPG Photonics, YLR-30-1064-LP-SF), delivering up to 30 W of output power at 1064 nm in a single-frequency, linearly-polarized beam with a spatial quality factor of M^2~1.01 and a nominal linewidth of 89 kHz. A Faraday isolator (FI) with an isolation of ~25 dB was used at the output end of the fiber to prevent back-reflection into the laser. To maintain stable output characteristics, we operated the pump laser at maximum output power and attenuated the power using a combination of a half-wave plate (HWP) and a polarizing beam-splitter (PBS). A second HWP was used to control the pump polarization for phase-matching in the nonlinear crystal, which is a 50-mm-long, 6.2-mm-wide, 1-mm-thick, 5% MgO-doped periodically-poled LiNbO$_3$ (MgO:PPLN). The crystal was housed in an oven with a stability of ±0.1 ^{o}C and adjustable from room temperature to 200 ^{o}C. The crystal contains five gratings with periods ranging from Λ=29.5 μm to Λ=31.5 μm, in steps of 0.5 μm. However, we only used the Λ=31.5 μm grating period in this work, providing a theoretical wavelength tuning range of 1663-1944 nm for the signal and 2954-2350 nm for the idler, for the crystal temperature varying from 25 ^{o}C to 200 ^{o}C. A lens of focal length, f=250 mm, was used to focus the fundamental beam at the centre of the crystal. The OPO was configured in a standing-wave cavity, comprising two concave mirrors, M$_1$ and M$_2$ (r=150 mm), one plane mirror (M$_3$) in one arm, and an ARR interferometer formed by two plane mirrors (M$_4$ and M$_5$) and a BS integrated into the other arm. For the BS, we used a standard, low-cost, commercial fused silica plate available in our laboratory. The plate was 3-mm-thick with broadband coating over 0.9-2.6 μm. Such a BS could allow output coupling optimization over a broad spectral range, given the simplicity and effectiveness of the ARR technique. However, in this work we only performed the measurements at a fixed signal wavelength, using a single grating period to demonstrate the concept in a cw SRO, for the first time. All the OPO mirrors (M$_{1-5}$) were

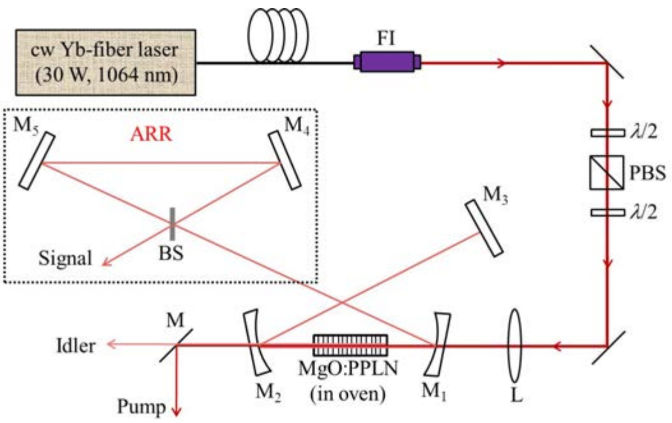

Figure 4.2: Schematic of the experimental setup. FI: Faraday isolator, $\lambda/2$: Half-wave plate, PBS: Polarizing beam-splitter, L: Lens, M$_{1-5}$: Mirrors, M: Dichroic mirror, BS: Beam-splitter.

highly reflective (R>99%) for the signal (1.3-1.9 μm) and highly transmitting (T>90%) for the idler (2.2-4 μm), ensuring SRO operation. The mirrors are also highly transmitting (T>92%) for the pump. A dichroic mirror, M, was used to separate the pump from the generated idler beam. The total SRO cavity length was L_{SRO}=183 cm, which was the sum of the standing-wave cavity length ($2L_{linear}$=166.8 cm) and length of the ARR interferometer (L_{ring}=16.2 cm).

4.2.2 Design and optimization of the cavity

In order to optimize the SRO, we used a focusing parameter [76],

$$\xi = \frac{l}{bp} \tag{4.1}$$

where b_p is the confocal parameter of the pump, defined as

$$b_p = \frac{k}{w_p} \tag{4.2}$$

with

$$k = \frac{2\pi n_p}{\lambda_p} \tag{4.3}$$

Here, l=50 mm is the length of the nonlinear crystal, n$_p$, λ_p, w_p are the refractive index, wavelength and waist radius of the pump beam inside the nonlinear crystal, respectively. In this experiment, the pump beam is confocally focused to a beam waist radius of w_p=63 μm, corresponding to a focusing parameter of ξ=l/b_p∼1, while the design of the SRO cavity resulted in a signal beam waist radius of w_s=76 μm at the centre of the nonlinear crystal. Thus, the cavity design ensures optimum overlap of pump and resonant signal at the center of the crystal (b_p∼b_s).

4.3 Results and discussion

4.3.1 Conventional 5% output-coupled SRO

Power scaling

Initially, we performed the power scaling of the cw SRO with a conventional 5% OC mirror in place of the ARR output coupler (ARR-OC). The total SRO cavity length was $2L_{linear}$=2×91.5 cm = 183 cm, equal to that of the ARR output-coupled SRO (ARR-OC-SRO). In both configurations, we used the same focusing condition for the pump and adjusted the cavity for optimum overlap between the pump and the signal beam in the cold cavity. We operated the SRO at the center of the tuning range for the Λ=31.5 μm grating, and generated a signal wavelength of λ_{signal}=1706 nm and a corresponding idler wavelength of λ_{idler}=2826 nm, maintaining the crystal temperature at 88.5 ^{o}C. Figure 4.3 shows the variation of signal, idler and the total power (signal plus idler) as a function of pump power for the conventional 5% output-coupled SRO (OC-SRO). We obtained a signal power of 4.56 W and idler power of 4.09 W at a maximum pump power of 28.6 W. The total power extracted at the maximum pump power was thus 8.65 W.

4.3.2 Variable output coupling

In order to perform output coupling optimization using the ARR technique, we first characterized the ARR interferometer prior to integration into the cw SRO by evaluating the transmission of output signal wavelength through the ARR at different angles, θ_{BS}, external to the SRO cavity. We measured the input power into the ARR and the output power from the ARR at a fixed signal wavelength (1706 nm), and estimated the ARR transmission as a function of the incident angle, θ_{BS}, on the BS. The result is shown in Fig. 4.4, where it can be seen that with the increase in θ_{BS} from 20^{o} to 40^{o}, the transmission

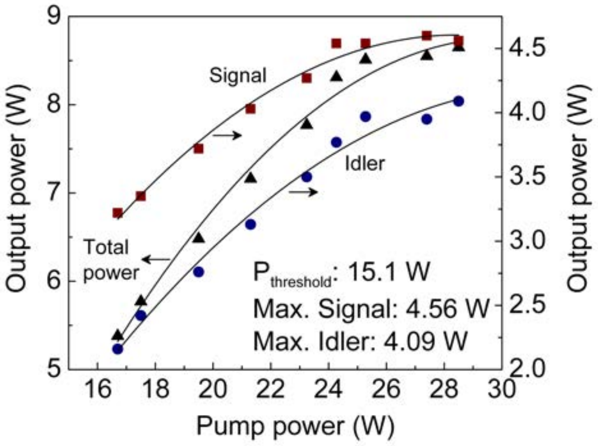

Figure 4.3: Variation of signal and idler power along with the total power extracted from the OPO using conventional 5% OC as a function of input pump power.

of the ARR increases continuously from 0.8 to 7.3%. Since the performance of cw SRO depends strongly on the cavity losses, we estimated the additional average loss due to the ARR elements. By measuring the transmitted and reflected power from the BS at different θ_{BS}, the total average BS loss at 1706 nm was found to be ~1.5% throughout the BS angular range, while the extra mirror (M_5) introduced an additional coating loss of ~0.5%. Therefore, with the available BS and mirror M_5, the characterization of the ARR-OC-SRO, as described below, was performed in the presence of an additional loss background of ~2%. By using a more optimum BS and mirror combination with lower insertion loss, we expect significant improvements in ARR-OC-SRO performance with regard to output power and pump threshold.

After external characterization, we integrated the ARR into the cw SRO cavity. In order to determine the optimum ARR-OC value for the signal, we varied θ_{BS} continuously, as we did in external characterization. We performed power scaling measurements for different angles of incidence, θ_{BS}, at a signal wavelength of 1706 nm (idler at 2826 nm), by recording the signal output power from the ARR-OC-SRO, and the corresponding single-pass idler power from the oscillator.

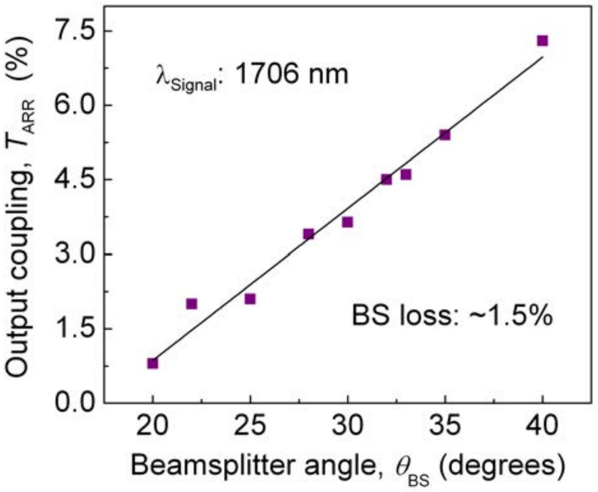

Figure 4.4: Transmission from ARR interferometer as a function of BS angle, θ_{BS}.

4.3.3 Output coupling optimization at different pumping levels

Experimental

To study the behavior of simultaneously extracted signal and idler power with the increase in the ARR transmission, and hence to obtain the absolute value of optimum ARR-OC at different pumping levels, we optimized the cw ARR-OC-SRO for input powers of 15.9 W and 23.2 W. Figures 4.5(a) and 4.5(b) show the output coupling optimization of signal at pump powers of 15.9 W and 23.2 W, respectively, by varying the BS angle, θ_{BS}. As seen in Fig. 4.5(a), the signal power increases from 0.54 W at θ_{BS}=20^o (T_{ARR}=0.8%) to a maximum value of 1.22 W at θ_{BS}=22^o (T_{ARR}=2%). Further increasing the BS angle beyond θ_{BS}=22^o results in the drop of signal power to 0.87 W at θ_{BS}=25^o (T_{ARR}=2.1%), confirming 2% as the optimum ARR-OC value for the signal at 15.9 W of pump power. Measurements beyond θ_{BS}=25^o were not possible due to the increase in the threshold power. Similarly, at a pump power of 23.2 W, seen in Fig. 4.5(b), the signal power increases from 1.15 W to a maximum value of 2.28 W at θ_{BS}=33^o (T_{ARR}=4.6%). Further increasing the BS angle results in the drop of signal power to 1.64 W at θ_{BS}=40^o (T_{ARR}=7.3%), confirming

4.6% as the optimum ARR-OC value for the signal at 23.2 W of pump power. This clearly shows the potential of the ARR technique for in situ optimization of output power from the cw SRO (or any optical oscillator) under different operating conditions, including different pumping levels.

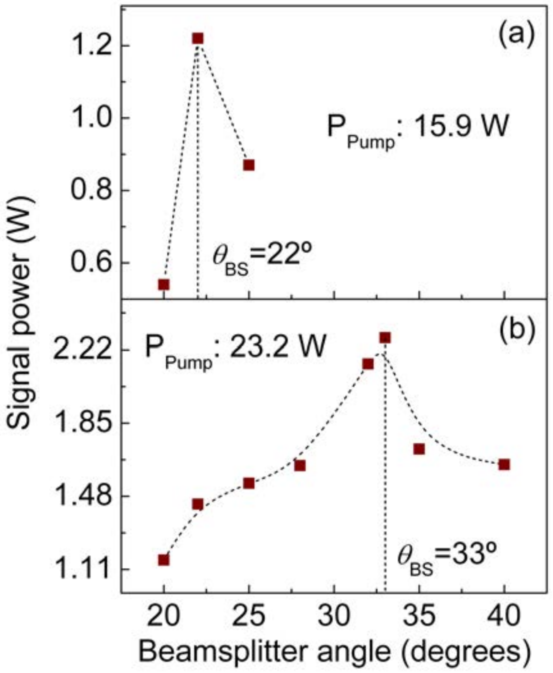

Figure 4.5: Optimization of signal power versus BS angle, θ_{BS}, at input pump power of (a) 15.9 W, and (b) 23.2 W.

Figure 4.6(a) and 4.6(b) show the simultaneously extracted single-pass idler power at pump powers of 15.9 W and 23.2 W, respectively, as a function of BS angle. As evident from Fig. 4.6(a), at a pump power of 15.9 W, the idler power decreases from 2.35 to 1.79 W for an increase in θ_{BS} from 20^o to 25^o. Similarly, at a pump power of 23.2 W, the idler power decreases gradually from 3.36 to 3.15 W for an increase in θ_{BS} from 20^o to 32^o, and has a sharp fall with further increase of θ_{BS} beyond the optimum angle of θ_{BS}=33^o, up to 40^o. The decrease in the idler power with the increase in θ_{BS} can be attributed to the increasing output coupling loss of the resonating signal wave with increase in ARR transmission, resulting in reduced intracavity signal intensity to mix with the pump to generate the single-pass idler. Thus, the idler output power is reduced with increasing θ_{BS} (higher signal output coupling) for all pump powers, indicating that the idler power is not necessarily maximized at the optimum signal output coupling. Hence, the ARR also enables the possibility of exploring the idler output power as a function of output coupling as well as independently maximizing the signal and idler output power, which are difficult to study with conventional discrete output couplers.

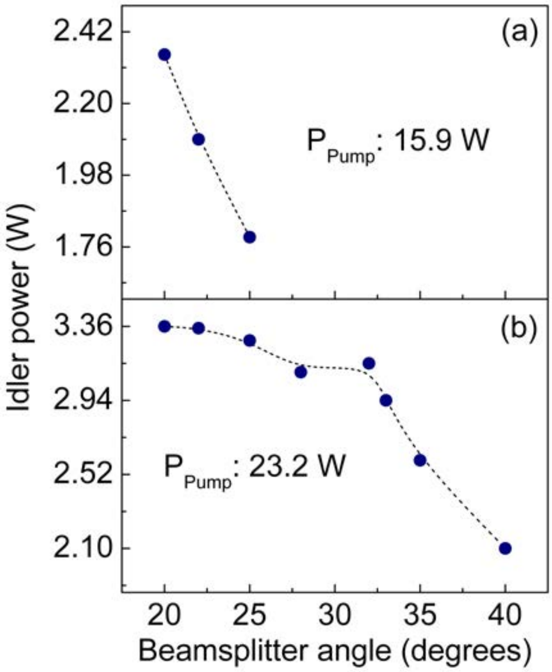

Figure 4.6: Optimization of simultaneously extracted single-pass idler power versus BS angle, θ_{BS}, at input pump power of (c) 15.9 W, and (d) 23.2 W.

Theoretical

In order to compare the observed behavior of signal and idler power in Figs. 4.5(a) and 4.5(b), and Figs. 4.6(a) and 4.6(b) with theory, we also performed calculations to obtain the variation of extracted signal power, and the corresponding idler power, as a function of signal output coupling. We performed the calculations for a conventional cw OC-SRO deploying a partially transmitting mirror, while considering a fixed background cavity loss of 2%, a pump depletion of 70%, a Gaussian pump beam profile, and assuming no thermal effects [88–90]. The results are shown in Fig. 4.7(a) and 4.7(b) for a fixed pump power of 15.9 W and 23.2 W, respectively. As evident, at pump power of 15.9 W and 23.2 W, the optimum output coupling for the signal is attained at 3.6% and 4.8%, respectively, and the corresponding idler power decreases with increase in output coupling. The maximum idler power is obtained at the minimum signal output coupling value for both the pumping levels, as also observed in Fig. 4.6(a) and 4.6(b).

It is also evident from theoretical curves, Fig. 4.7(a) and 4.7(b), that with increase in pump power, the output coupling optimization curve for signal is broadened, which is also observed in Fig. 4.5(a) and 4.5(b). The theoretical variation of signal and idler power as a function of output coupling in Fig. 4.7 are thus in good agreement with the experimental results shown in Fig. 4.5 and Fig. 4.6, confirming that the ARR behaves in the same way as a conventional output coupler.

To obtain a clearer picture, we calculated the signal output power optimization curve at a low pump power of 5 W and a high pump power of 28.6 W, with the results shown in Fig. 4.8. As seen, at high pump power the range of optimum output coupling values is significantly broader than at the low pump power, where the attainment of optimum output coupling is critical.

4.3.4 Power scaling

At ARR-OC value of 33^o

At the ARR-OC value of 4.6%, the power scaling of the ARR-OC-SRO is shown in Fig. 4.9, depicting the variation of signal power, the corresponding idler power, and the total output power as a function of input pump power. The

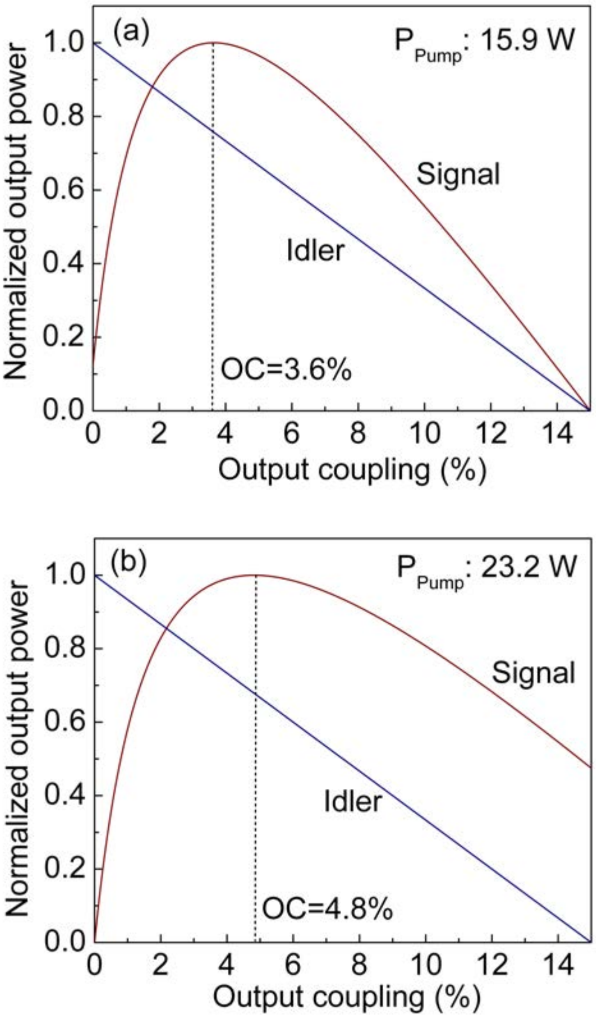

Figure 4.7: Theoretically calculated optimization curves for signal and idler power as a function of output coupling at input pump power of (a) 15.9 W, and (b) 23.2 W.

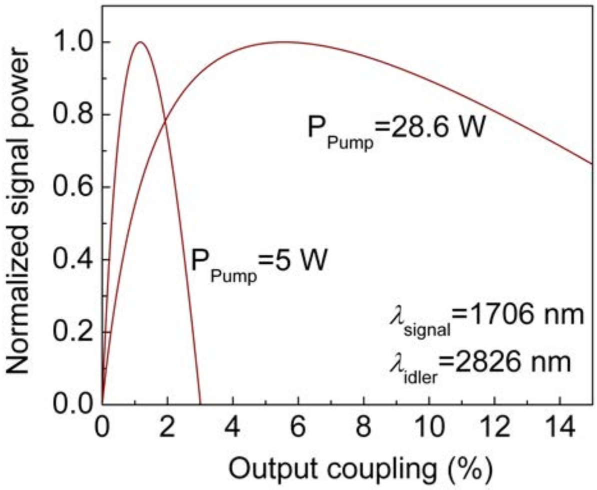

Figure 4.8: Theoretically calculated optimization curves for signal power as a function of output coupling at low pump power of 5 W and high pump power of 28.6 W.

maximum signal and idler power achieved are 2.81 W and 3.88 W, respectively, corresponding to a maximum achieved total output power (signal plus idler) of 6.69 W, representing a total extraction efficiency of 23.4%. The signal and idler power vary linearly up to the maximum pump power of 28.6 W. The variation of the total output power as a function of pump power also confirms the linear dependence. It is to be noted here that although no sign of saturation in the output power for higher pump power has been observed at the ARR-OC value of 4.6% (θ_{BS}=33^o), we have also not observed any evidence of saturation at lower output coupling values (smaller BS angles). This is attributed mainly to the background loss present at all the BS angles.

The lower output power obtained from the optimal ARR-OC-SRO at 23.2 W of pump power as compared to that with the conventional non-optimal 5% OC-SRO (see Fig. 4.3) is attributed to the extra insertion loss induced by the un-optimized BS and mirror coatings used in the present experiment, as noted previously. Although, the maximum output power from optimal ARR-OC-SRO has not been achieved, a background loss is present for all BS angles, indicating θ_{BS}=33^o (T_{ARR}=4.6%) as the optimum angle for maximum

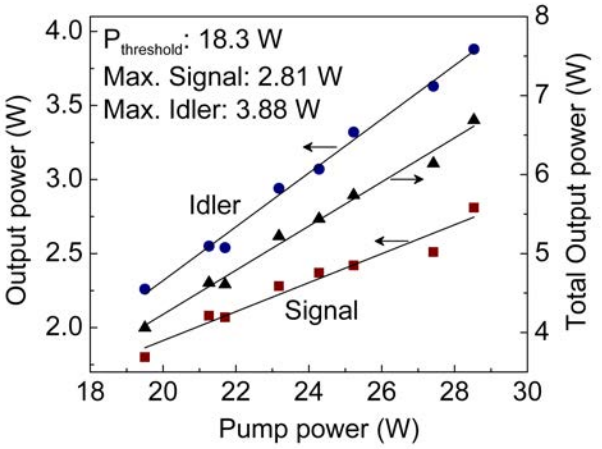

Figure 4.9: Signal and corresponding idler along with total output power scaling at BS angle, θ_{BS}=33^o.

output power extraction. The optimum ARR-OC value of 4.6% together in the presence of the background insertion loss associated with the ARR results in reduced intracavity signal power, leading to a lower maximum signal power extraction (see Fig. 4.9) than with the 5% conventional output coupler (see Fig. 4.3), and without any saturation in power scaling (see Fig. 4.9). By using a BS and mirrors with improved coatings, the absolute highest signal power can be extracted at optimum ARR-OC value. Further, with reduced insertion loss, we can expect similar output power in the ARR-OC-SRO to that in the conventional OC-SRO of the same output coupling.

At optimum ARR-OC values

Figure 4.10 shows the signal power extracted from the cw ARR-OC-SRO at the optimum output coupling value versus pump power. Each data point represents the maximum signal power at a given pump power, obtained by measuring the extracted signal power as a function of BS angle, while keeping the pump power fixed. As seen, the optimum signal power increases almost linearly, reaching 2.81 W for a maximum input power of 28.6 W. The inset of

Fig. 4.10 shows the theoretical power scaling of the signal for a conventional cw OC-SRO, calculated at the corresponding theoretical optimum output coupling values [88–90]. As can be seen, the theoretical power scaling shows the same behavior as the experimental variation of Fig. 4.10.

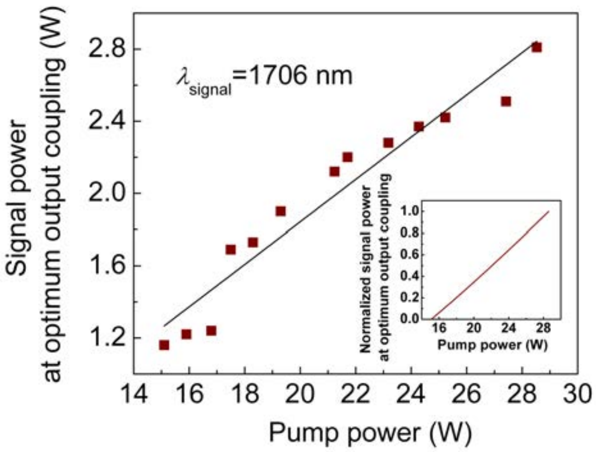

Figure 4.10: Signal power scaling at optimum signal output coupling values. Inset: Corresponding theoretical plot.

We also measured the extracted idler power as a function of pump power at minimum signal output coupling values corresponding to maximum idler power, for different pumping levels, as shown in Fig. 4.11. The output coupling for the signal, at which the idler power is maximum, always corresponds to the lowest value (T_{ARR}=0.8%) at θ_{BS}=20^o for all pump powers. The maximum idler power achieved is 4.2 W for a pump power of 28.6 W. The curve depicts the linear dependence of idler power on the input pump power. The calculated theoretical power scaling for the maximum idler [88–90] under minimum signal output coupling is also shown in the inset of Fig. 4.11, confirming a linear behavior similar to the experimental variation in Fig. 4.11.

4.3.5 Pump depletion, threshold pump power and beam quality

Figure 4.12 shows the corresponding pump depletion for the cw ARR-OC-

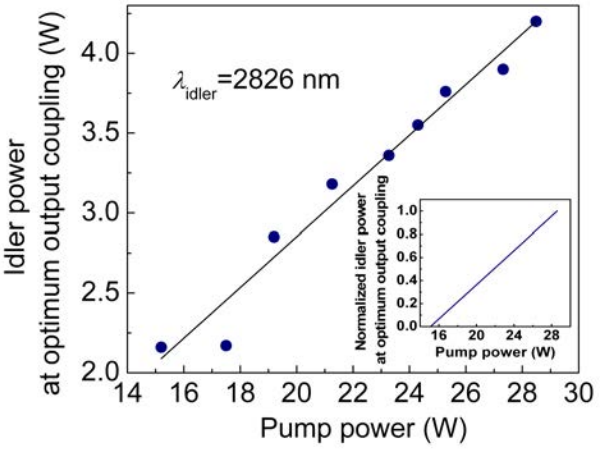

Figure 4.11: Idler power scaling at minimum signal output coupling values. Inset: Corresponding theoretical plot.

SRO at a fixed pump power of 23.2 W, for different BS angle. As seen, pump depletion decreases gradually from 56.6% to 51% for an increase in θ_{BS} from 20^o to 32^o, and has a sharp fall with further increase of θ_{BS} beyond the optimum angle (θ_{BS}=33^o) of signal power extraction. It has been observed that the pump depletion follows a similar behavior to the variation of idler power as a function of BS angle, and thus signal output coupling, as seen in Fig. 4.6(b).

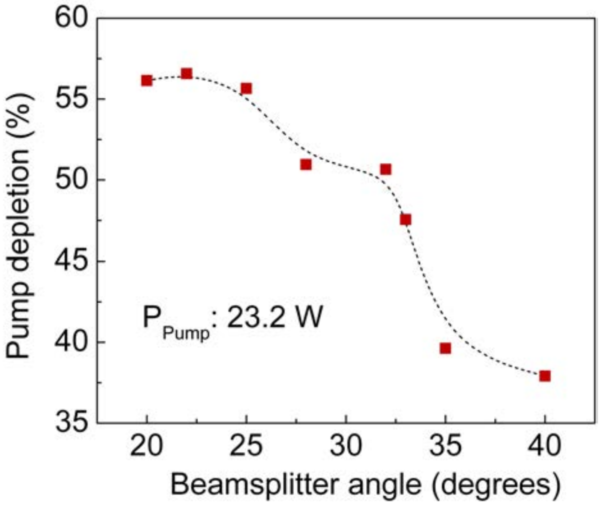

Figure 4.12: Pump depletion as a function of BS angle, θ_{BS}, at input pump power of 23.2 W.

We also recorded the cw ARR-OC-SRO threshold pump power for different values of ARR-OC, with the results shown in Fig. 4.13. By increasing the output coupling from 0.8% to 7.3%, the threshold pump power for the ARR-OC-SRO rises from 12.3 to 22.1 W, with the corresponding intracavity power estimated to decrease from 187 to 28 W at the maximum pump power of 28.6 W. The loss due to the ARR is also evident from the comparison of threshold power for the cw 5% OC-SRO and that for the 4.6% ARR-OC-SRO, which are measured to be 15.1 W and 18.3 W, respectively. With reduced insertion loss, we can expect similar pump power threshold for the ARR-OC-SRO to that in the conventional OC-SRO of the same output coupling.

We also recorded the far-field energy distribution of the output signal from the cw ARR-OC-SRO with θ_{BS}=33^o at 23.2 W of pump power, as shown in inset of Fig. 4.13. Using a f=100 mm focal length lens and a scanning beam profiler, the quality factor of the signal beam was measured to be $M_x{}^2{\sim}1.9$ and $M_y{}^2{\sim}1.9$, confirming TEM$_{00}$ spatial mode. We have not observed any degradation in output beam quality due to the integration of the ARR into the cw SRO. We do not expect any change in the beam quality with other ARR-OC values, as we have not observed any thermal effects at lowest as well as highest output coupling values.

4.4 Conclusions

In conclusion, we have demonstrated, for the first time to our knowledge, a versatile technique based on the use of an ARR interferometer for continuous fine adjustment of output coupling and in situ optimization of the output power in cw SROs. With fine adjustment of the ARR transmission, optimum output coupling value for signal and idler can be attained at different input pumping levels. The experimental results have also been shown to be in good agreement with the theoretical modeling. By deploying a custom-made BS and a mirror

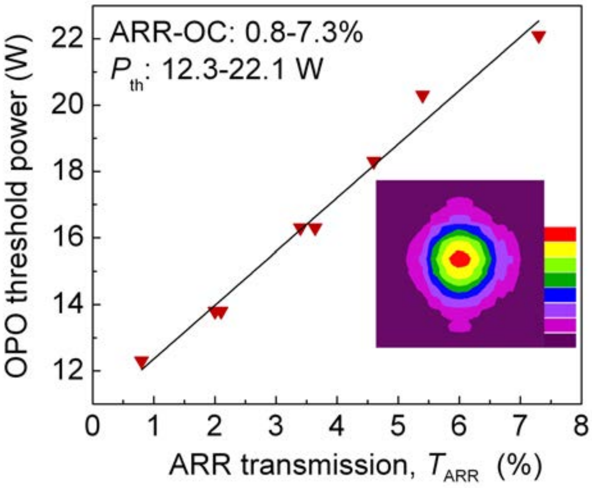

Figure 4.13: The cw SRO threshold power, P_{th}, as a function of signal output coupling with the ARR. Inset: far-field energy distribution of extracted signal with optimum ARR-OC value of 4.6% at 23.2 W of input pump power.

with improved coatings, resulting in lower insertion loss, the same maximum signal output power is expected from the cw ARR-OC-SRO as with a conventional cw OC-SRO of the same optimum output coupling. The technique is wavelength-independent, and so can be used over an extended spectral range with a single ARR setup. With advances in QPM materials, together with the available broadband-coated beam-splitters, the present set up can be further deployed over a wide wavelength range using fanned or multiple grating structures in combination with temperature tuning, indicating the potential use of this technique for widely tunable OPOs. This proof-of-principle demonstration also opens up new possibilities for other applications of the technique in cw optical oscillators in general, for example in the implementation of coupled cavities or cavity dumping and mode-locking, as first suggested in the context of lasers nearly four decades ago [91–94].

Chapter 5

All-periodically-poled, tunable, cw, near-infrared source

This chapter constitutes the following publication:

1. *High-power, continuous-wave, single-frequency, all-periodically-poled, near-infrared source*
   K. Devi, S. Chaitanya Kumar, and M. Ebrahim-Zadeh
   Opt. Letters **37**, 5049-5051 (2012)

5.1 Motivation

Tunable, continuous-wave (cw), single-frequency sources covering the 700–1000 nm spectral region are of considerable interest for diverse range of applications from spectroscopy and biomedicine to pumping of optical parametric oscillators (OPOs) [34, 95]. The Ti:sapphire laser, the workhorse of the near-infrared region, is the primary source in this spectral range, catering for the majority of applications. However, the need for bulk solid-state pump lasers and water-cooling increases complexity, cost, and size of the Ti:sapphire laser. It would be desirable to consider alternative new strategies for the generation of tunable near-infrared radiation while overcoming such limitations. Deploying compact, robust, and efficient fiber-laser-based pump sources in the green is a practical alternative to partly reduce the complexity of the Ti:sapphire laser [96, 97], but direct nonlinear frequency conversion using second-harmonic-generation (SHG) or techniques based on OPOs are other attractive alternatives to access the Ti:sapphire wavelength range. Earlier reports on cw nonlinear frequency conversion into the Ti:sapphire wavelength range include the generation of high-power cw radiation at 970 nm based on single-pass SHG of a Tm-fiber laser in periodically-poled $LiNbO_3$ (PPLN) [98], tunable signal radiation from an output-coupled singly-resonant OPO (SRO) based on MgO-doped stoichiometric periodically-poled $LiTaO_3$ (MgO:sPPLT) pumped in the green [83], and frequency-doubling of the idler output from a cw green-pumped OPO using external enhancement [99]. Further, a narrowly tunable 629 nm source based on a cw OPO using sum-frequency-mixing in a dual-grating PPLN crystal was also demonstrated [100]. However, achieving tunability in combination with high output power has remained challenging. Another attractive approach to generate tunable radiation in 700–1000 nm spectral range is the intracavity SHG of the resonant signal wave in SROs pumped by high-power laser sources near 1 μm. This approach has been demonstrated in a Yb-laser-pumped picosecond OPO [101]. In cw SROs based on quasi-phase-matched (QPM) nonlinear materials such as multigrating MgO-doped periodically-poled $LiNbO_3$ (MgO:PPLN) [41], offering wide signal tuning range and high circulating powers, internal SHG can be similarly exploited to achieve wavelength extension into the near-infrared at high efficiency and over a broad spectral range. Moreover, with the advances in QPM materials and mature fabrication technology, it is now possible to readily access crystals such as MgO:PPLN and MgO:sPPLT with different grating designs. In particular, MgO:sPPLT, offering high resistance to photorefractive damage below 1 μm, relatively high nonlinearity (d_{eff}~9 pm/V), and interaction lengths up to 30 mm, are now commercially available in fanout-grating design, providing additional advantage of continuous tuning at a fixed temperature [37]. Thus, the combination of newly available QPM material designs, together with latest generation of fiber lasers, can lead to the realization of efficient, compact, and tunable cw sources for the 700–1000 nm spectral range, as a potential future alternative to the Ti:sapphire laser for a variety of applications.

In this chapter, we demonstrate this potential by describing a high-power, single-frequency, all-periodically-poled, near-infrared source tunable across 775–807 nm, based on intracavity SHG of a cw SRO and pumped by a Yb-fiber laser at 1064 nm. The device, which uses a multigrating MgO:PPLN crystal for OPO and a MgO:sPPLT crystal fanout grating for intracavity SHG, provides cw single-frequency radiation tunable across 775–807 nm, with >3.0 W of output across 56% of the tuning range, together with >3.8 W of mid-infrared power over 77% of the idler tuning range of 3125–3396 nm for 27.4 W of fiber pump power.

5.2 Experimental setup

The schematic of the experimental setup is shown in Fig. 5.1. The pump source is a cw Yb-fiber laser (IPG Photonics, YLR-30-1064-LP-SF), delivering up to 30 W of output power at 1064 nm in a single-frequency, linearly-polarized beam with M^2~1.01 and a nominal linewidth of 89 kHz. The nonlinear crystal used for OPO is a 48-mm-long, 6.2-mm-wide, 1-mm-thick, multigrating MgO:PPLN sample (HC Photonics, Taiwan). The crystal contains five gratings with periods ranging from Λ=29.5–31.5 μm, in steps of 0.5 μm, with the end faces antireflection (AR)-coated over 1450–1750 nm (R<1%), 2500–3700 nm (R<3%) and 1064 nm (R<3%). For intracavity SHG, we used 30-mm-long, 16-mm-wide, 0.5-mm-thick, MgO:sPPLT crystal (HC Photonics, Taiwan) with fanout grating, Λ=19.6–22.3 μm, across the 16 mm width. The crystal end faces are AR-coated over 1500–1600 nm (R<1%) and 750–800 nm (R<1%). The crystals are housed in two ovens with stability of 0.1^{o}C, which can be controlled independently from room temperature to 200 ^{o}C. The OPO cavity is configured in a folded ring, comprising four concave mirrors, M_{1-4}(r=150 mm) and two plane mirrors, $M_{5,6}$. All mirrors (Laseroptik, Germany) are highly reflective (R>99.6%) for the signal (1250–1800 nm) and highly transmitting (T>90%) for the idler (2200–4000 nm), ensuring SRO operation. Mirror M_4 is also highly transmitting (T>97%) over 600–800 nm. A lens of focal length, f=200 mm, was used to focus the pump beam to a waist radius of w_p=66 μm, corresponding to confocal focusing parameter of ξ_p~0.87, while the design of the SRO cavity resulted in a primary signal waist radius of w_{s1}=80 μm at the center of the MgO:PPLN crystal ($b_p \sim b_{s1}$) between mirrors M_1 and M_2, and secondary signal radius of w_{s2}=117 μm (ξ_{s2}~0.26) at the center of the MgO:sPPLT crystal, between mirrors M_3 and M_4. Dichroic mirrors, M′ and M″, were used to separate the pump from the generated idler beam through M_2, and the generated SHG beam from the leaked-out signal through M_4, respectively.

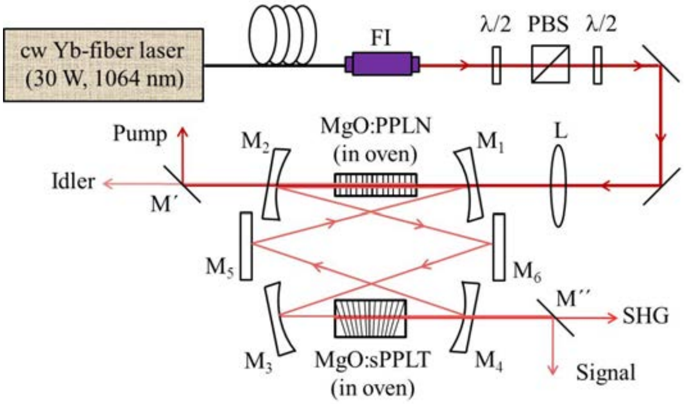

Figure 5.1: Schematic of the intracavity frequency-doubled cw OPO. FI: Faraday isolator, $\lambda/2$: Half-wave plate, PBS: Polarizing beam-splitter, L: lens, M_{1-6}: Cavity mirrors, M′ and M″: Dichroic mirrors.

Photograph of the intracavity frequency-doubled cw OPO system operating in our laboratory is shown in Fig. 5.2. The resonator mirrors and nonlinear crystals are marked in accordance with the schematic of the experimental configuration as shown in Fig. 5.1.

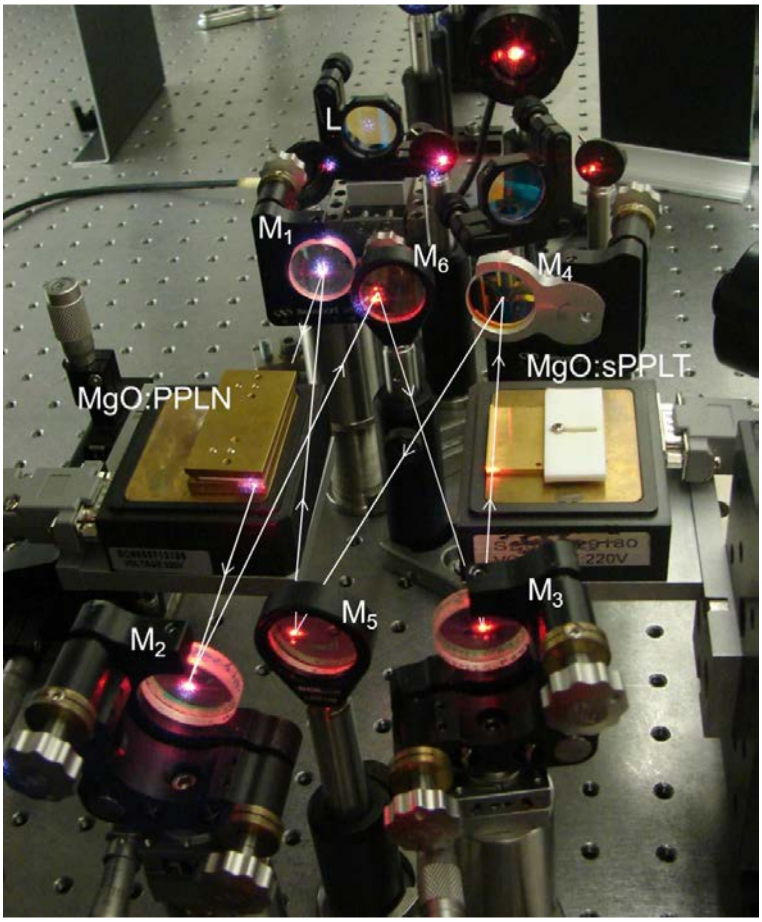

Figure 5.2: Photograph of the all-periodically-poled, near-infrared source operating in our laboratory.

5.3 Results and discussion

5.3.1 Power across the tuning range

In this work, we used the Λ=30.5 μm grating period in the MgO:PPLN crystal, providing a signal tuning range of ∼1544–1618 nm and an idler range of ∼3423–3107 nm, for a change in the crystal temperature from 25 ^{o}C to 200 ^{o}C. We initially varied the temperature of the MgO:sPPLT crystal (T_{SHG}) keeping the crystal fixed at the longer grating periods, while maintaining the temperature of the MgO:PPLN crystal (T_{OPO}) at 177 ^{o}C (λ_{signal}=1602 nm). At a fixed pump power of 27.4 W, we measured the QPM temperature for SHG to be 129 ^{o}C, confirming the longer grating period under use to be Λ_{SHG}=22.12 μm.

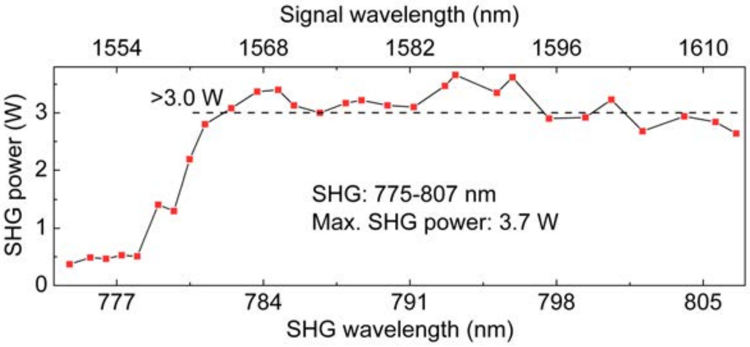

Figure 5.3: Variation of SHG power as a function of SHG wavelength.

The SHG tuning in the present device can be achieved by varying the grating period or temperature of the MgO:sPPLT crystal, while keeping either parameter fixed. Initially, SHG coverage across 775–801 nm was achieved by simultaneously varying temperature of MgO:PPLN crystal, T_{OPO}, over 57 ^{o}C–177 ^{o}C, and the grating period of MgO:sPPLT (Λ_{SHG}), at a fixed MgO:sPPLT temperature of T_{SHG}=129 ^{o}C. The SHG tuning range was then further extended up to 807 nm by increasing T_{OPO} to 195 ^{o}C, for a fixed Λ_{SHG}=22.12 μm, with corresponding increase in T_{SHG} from 129 ^{o}C to 200 ^{o}C. This resulted in an overall idler tuning over 271 nm, across 3125–3396 nm, corresponding to a resonant signal wavelength range of 1550–1613 nm, and tunable SHG coverage over 775– 807 nm. Figure 5.3 shows the measured SHG power across the tuning range for a fixed pump power of 27.4 W. As evident, the SHG is continuously tunable over the entire tuning range, providing >3 W of output power over 56% of the SHG tuning range with a maximum of 3.7 W at λ_{SHG}=793 nm. Figure 5.4 shows the calculated SHG tuning curves, (a) and (b), using the relevant Sellmeier equations [102], where good agreement with the experimental data in Fig. 5.3 has been confirmed. The simultaneously measured idler power across the tuning range is shown in Fig. 5.5. We achieved >3.8 W of output power over 77% of the idler tuning range with a maximum of 4.3 W at λ_{idler}=3133 nm. The pump depletion remains above 61% over 67% of the idler tuning range, and follows the similar behavior to the idler power over the entire tuning range, as shown in Fig. 5.5.

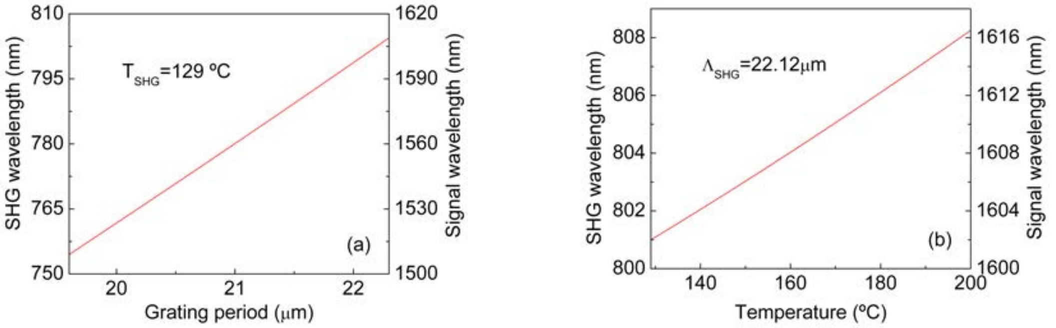

Figure 5.4: Theoretical SHG (a) grating tuning range and (b) temperature tuning range in present setup.

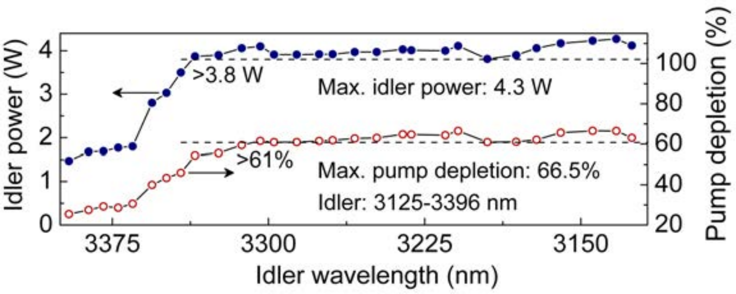

Figure 5.5: Variation of idler power and corresponding pump depletion across the idler tuning range.

5.3.2 Power scaling

In order to investigate the performance of the device near 800 nm, we performed simultaneous power scaling measurements of SHG output and the corresponding idler at the SHG wavelength of 801 nm, as shown in Fig. 5.6(a). The SHG power shows quadratic dependence up to ∼17 W of pump power, beyond which it grows linearly, with a maximum of 3.2 W generated for 27.4 W of pump power. The corresponding maximum idler power obtained is 4.1 W at λ_{idler}=3168 nm, representing a total extraction efficiency of 26.6%. We obtained the maximum overall extraction efficiency of 28% at a SHG wavelength of 793 nm, which corresponds to SHG power of 3.7 W together with an idler power of 4.0 W at 3232 nm. The pump power threshold of the cw SRO with intracavity SHG is recorded to be 7.5 W. The corresponding pump depletion reaches a maximum of ∼65% at 24.6 W of pump power, as shown in Fig. 5.6(a).

Figure 5.6(b) shows the variation of the signal power leaked-out through mirror M_4, as a function of pump power. The signal power has a linear dependence on pump power up to ∼17 W, beyond which there is evidence of saturation. The effect of saturation at higher pump power could be attributed to the non-optimal mode matching. Considering the signal leakage through other OPO cavity mirrors as well, we expect a total signal output power of ∼370 mW at maximum pump power. Using the leaked-out signal power and transmission of mirror M_4 at 1602 nm, we calculated the intracavity signal power at maximum pump power to be 23.5 W, resulting in a single-pass SHG conversion efficiency of 13.6%.

5.3.3 Power stability

We also recorded the passive power stability of the generated SHG at 801 nm and the corresponding idler, simultaneously, for the maximum pump power of 27.4 W, under free-running conditions. The results are shown in Figs. 5.7(a) and 5.7(b), where the SHG power is recorded to exhibit passive rms stability

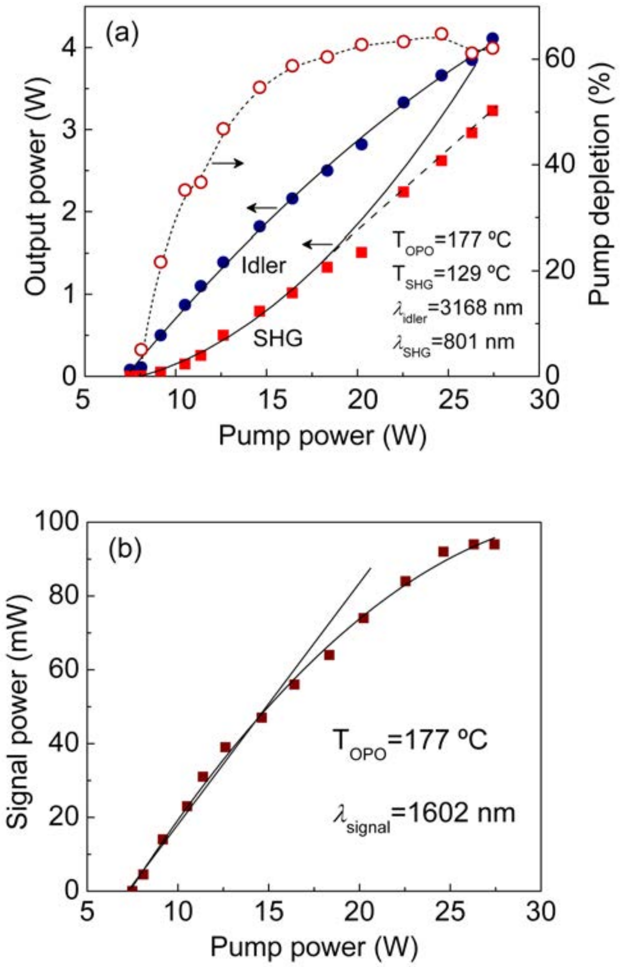

Figure 5.6: Variation of (a) SHG power, idler output power, pump depletion, and (b) signal power as a function of pump power.

better than 3.5%, while the idler power stability is recorded to be better than 1.3% over more than 1 minute. The power stability of the system is expected to be improved with active control, and using thermal and mechanical-vibration isolation.

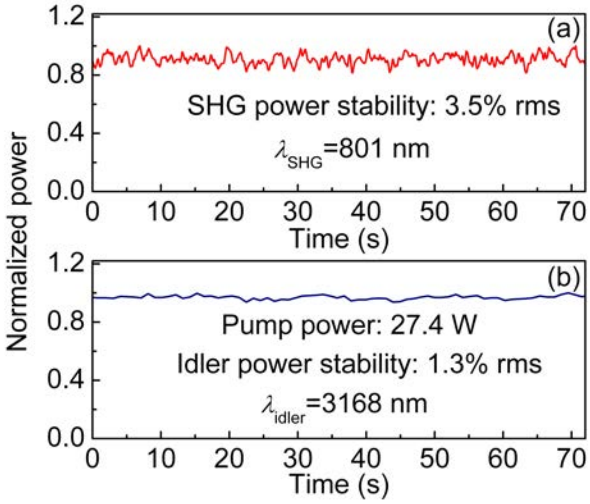

Figure 5.7: Simultaneously recorded passive power stability of (a) SHG and (b) idler output from the SRO.

5.3.4 Single-frequency operation and beam quality

Further, we analyzed the single-frequency spectrum of the SHG output using a confocal Fabry–Perot interferometer (FSR=1 GHz, finesse=400). The measurement was performed at 801 nm and at maximum SHG power. The transmission spectrum confirms single-frequency operation with an instantaneous linewidth of 8.5 MHz, as shown in Fig. 5.8. Similar behavior was observed across the full SHG tuning range.

Figure 5.9 shows the recorded far-field energy distribution of the SHG output at 801 nm, together with the orthogonal intensity profiles, at maximum pump power. The data confirm Gaussian distribution with a beam circularity >90%. For different pumping levels, and across the tuning range, we have observed similar behavior. We measured the M^2 factor of the SHG beam at maximum pump power using a lens and scanning beam profiler, and found $M_x{}^2<1.4$ and $M_y{}^2<1.4$, confirming TEM_{00} spatial mode.

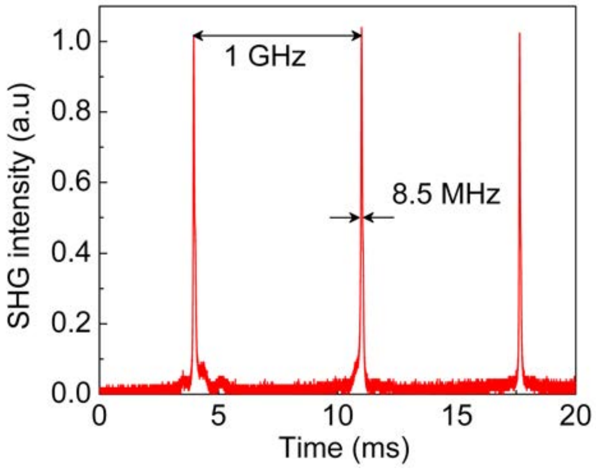

Figure 5.8: Single-frequency spectrum of generated SHG at 801 nm for pump power of 27.4 W.

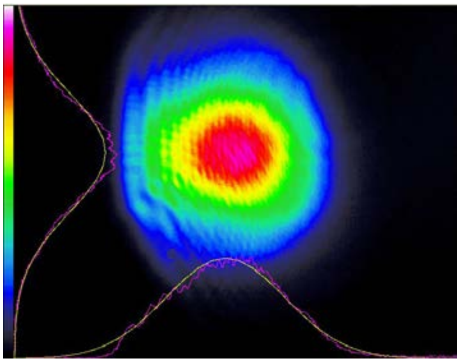

Figure 5.9: Far-field energy distribution of generated SHG at 801 nm for pump power of 27.4 W.

5.4 Conclusions

In conclusion, we have demonstrated a high-power, single-frequency, high-beam-quality, cw source tunable across 775–807 nm using intracavity frequency-doubling of a cw SRO based on all-periodically-poled materials. Together with SHG, idler tuning across 3125–3396 nm has also been achieved, providing high output power. With improved thermal isolation and active control, the power stability could be further improved. The SHG tuning can be further extended to cover almost the entire Ti:sapphire wavelength range (∼740–972 nm) using different grating periods of the employed MgO:PPLN crystal and simultaneously varying the grating of the MgO:sPPLT crystal. In order to further extend the tunability in signal wavelength range, partial signal output coupling can be implemented [41, 103], but at the cost of lower output SHG power. Given the power scaling capability of fiber lasers, the described approach also offers clear potential for even higher SHG output powers with increased pump powers.

Chapter 6

Continuous-wave ultraviolet source based on BiB_3O_6

This chapter constitutes the following publication:

1. *Stable, continuous-wave, Yb-fiber-based single-pass ultraviolet source*
   S. Chaitanya Kumar, **K. Devi**, and M. Ebrahim-Zadeh
   Opt. Letters, submitted (2013)

6.1 Motivation

Continuous-wave (cw) ultraviolet (UV) sources are of great interest for variety of applications including photolithography, optical data storage, flow cytometry and other life science applications. For many years, access to the UV spectral region was possible mainly by bulky, complex and power-hungry gas lasers [104].

Crystal	**PM**	**Type/ Interaction**	**PM angle**	**d$_{eff}$ (pm/V)**	**FOM**	α_{UV} **(cm^{-1}) @ 355 nm**	**$\Delta\rho$ (mrad)**
LBO	Birefringent	Type-I (ooe)	θ=90^o, ϕ=37.2^o	0.7	0.12	0.003	0
BBO	Birefringent	Type-I (ooe)	θ=31^o	2.0	0.87	<0.1	0
BIBO	Birefringent	Type-I (eeo)	θ=146.2^o, ϕ=90^o	3.9	2.42	0.02 (o-ray)	3.23
MgO:sPPLT	3rd-order QPM	Type-0 (eee)	Noncritical	2.7	0.67	<1	–

Table 6.1: Phase-matching (PM) properties of some nonlinear crystals for UV generation.

With the advent of nonlinear materials such as LiB_3O_5 (LBO) and β-BaB_2O_4 (BBO), optical frequency conversion proved an attractive alternative to reach the UV wavelength range, even enabling recent commercial realization of all-solid-state cw UV sources. Owing to the relatively small nonlinearity of LBO and BBO, as well as the low nonlinear gain available in the cw regime, such sources typically employ intracavity sum-frequency-generation (SFG) or cascaded second-harmonic-generation (SHG) in external resonant enhancement cavities, both requiring complex system architectures and mandatory active stabilization. On the other hand, single-pass schemes are simple, compact and robust, and can directly transfer the frequency and power stability of the input to the frequency converted output without the need for active stabilization. However, the material of choice should possess sufficiently high nonlinearity to generate practical output powers. Hence, the choice of the nonlinear material is very crucial for efficient UV generation in a single-pass scheme. The phase-matching (PM) properties of some promising nonlinear materials for UV generation are listed in Table 6.1. The most widely established materials for UV generation are birefringently phase-matched LBO [105] and BBO [106], but their low nonlinearity precludes single-pass SFG. The quasi-phase-matched (QPM) nonlinear material such as MgO-doped periodically-poled stoichiometric $LiTaO_3$ (MgO:sPPLT) with high nonlinearity and no spatial walk-off, also has wide transparency range into the UV. It has been successfully deployed in single-pass SHG configuration to generate high-power cw single-frequency green radiation [44, 74, 107]. However, 1^{st}-order QPM SFG into the UV requires a grating period of ~ 2 μm, which is quite challenging to fabricate. As a result 3^{rd}-order QPM, with a reduced effective nonlinear coefficient of 2.7 pm/V has been used to generate UV radiation under temperature phase-matching [108, 109]. On the other hand, the birefringent material, BiB_3O_6 (BIBO), belonging to the borate family of nonlinear crystals, possesses unique linear and nonlinear optical properties for frequency conversion from the UV to the infrared [110–112]. It can be phase-matched, at room temperature for UV generation under type-I ($ee\rightarrow o$) interaction for SFG of infrared and green. As the two input beams at 1064 nm and 532 nm are extraordinarily polarized, they experience a spatial walk-off of 64.8 mrad and 68 mrad, respectively, corresponding to a small relative walk-off, $\Delta\rho\sim$3.2 mrad. Its high nonlinearity ($d_{eff}\sim$3.9 pm/V) [111], bulk UV damage threshold (50 MW/cm^2) [113] and low UV absorption coefficient ($\alpha_{UV}<$0.02 cm^{-1}) [110, 111] makes it an attractive alternative material for SFG into the UV. Its nonlinear figure-of-merit, FOM is >20 times higher as compared to that of LBO. As such, BIBO offers a highly attractive material for cw UV generation using SFG of 1064 nm and 532 nm radiation.

In this chapter, we demonstrate this capability in a single-pass SFG scheme, and in a fiber-based format, by using a cw Yb-fiber laser at 1064 nm as the input pump source. By deploying MgO:sPPLT as the SHG crystal [44, 107] and BIBO for SFG, up to 68 mW of cw UV single-frequency radiation at 354.7 nm has been generated. The generated UV output exhibits a passive power stability better than 3.2% rms over 2 hours and frequency stability better than 437 MHz over >2.5 hours, in a TEM$_{00}$ spatial beam profile. To our knowledge, this is the first demonstration of fiber-based single-pass cw SFG into the UV using BIBO.

6.2 Experimental setup

The schematic of experimental setup for single-pass UV generation is shown in Fig. 6.1. The fundamental pump source is a cw Yb-fiber laser (IPG Photonics, YLR-30-1064-LP-SF) delivering up to 30 W of output power at 1064 nm in a single-frequency, linearly-polarized beam with $M^2\sim$1.01 and a nominal linewidth of 89 kHz. An isolator at the output end of the fiber protects the laser from any back-reflections. The power from the fiber laser is adjusted by using a combination of half-wave plate (HWP) and polarizing beam-splitter (PBS) cube. A second HWP is used to obtain the required polarization for phase-matching in the nonlinear crystal. The setup essentially consists of a SHG stage and a SFG stage. We used a 30-mm-long, 2-mm-wide and 1-mm-thick MgO:sPPLT crystal with a single grating period of 7.97 μm, housed in an oven with a temperature stability of $\pm 0.1\ ^{o}$C, for the SHG stage. The SFG stage comprises a 10-mm-long, 3-mm-wide and 3-mm-thick BIBO crystal, cut at θ=146.3^{o} and ϕ=90^{o} for type-I ($ee \rightarrow o$) phase-matched sum-frequency-mixing of 1064 and 532 nm radiation to generate UV radiation at 354.7 nm. The SHG stage is temperature phase-matched, while the SFG stage is angular phase-matched. The end faces of both the crystals are antireflection (AR)-coated (R<1%) at 1064 nm and 532 nm, while BIBO is also AR-coated for high transmission at 354.7 nm. Using a lens of focal length, f=125 mm, the fundamental beam at 1064 nm is focused to a waist radius of $w_{F1}\sim$30 μm at the center of the MgO:sPPLT crystal for SHG into the green at 532 nm. The generated green and the undepleted fundamental are again collimated and refocused by using, M_1 and M_2 in the SFG stage [44, 107]. The angle of incidence on these mirrors is limited by the mechanical constrains and are kept as small as possible. All the concave mirrors are AR-coated for high reflectivity (R>99%) at 1064 nm and 532 nm and are mounted on translation stages, so as to adjust the inter-crystal spacing. The radius of curvature of M_1 and M_2 are 150 mm and 200 mm, respectively, resulting in an estimated fundamental and generated SHG beam waist radii of $w_{F2}\sim$43 μm and $w_{SHG2}\sim$30 μm at the center of the BIBO crystal, corresponding to a Rayleigh range of >1 cm for both the beams. Rayleigh range, considering the refractive index of BIBO, is $\sim$2 cm in both the cases. It is well-known that in order to achieve effective interaction, the two beams must have same Rayleigh range [76]. In practice, optimum efficiency for SFG is achieved when the two interacting beam overlap as much as possible through the length of the crystal. The generated

UV radiation is separated using dichroic mirrors, M, and a piece of Scott glass (UG-11), F is used to filter out any residual fundamental and second-harmonic while measuring UV power. Figure 6.2 shows the picture of the single-pass UV generation setup operating in our laboratory, where the mirrors and nonlinear crystals are marked. The picture of the generated UV beam is also shown.

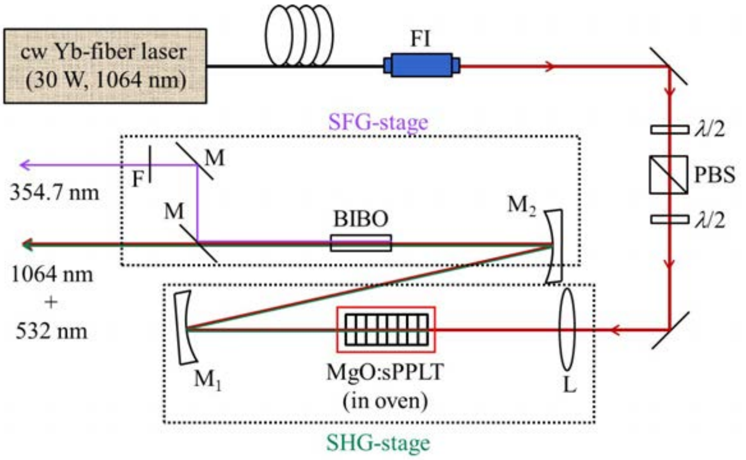

Figure 6.1: Schematic of experimental setup for the fiber-laser-based single-pass UV source. FI: Faraday isolator, $\lambda/2$: Half-wave plate, PBS: Polarizing beam-splitter, L: Lens, M: Mirrors, F: Filter.

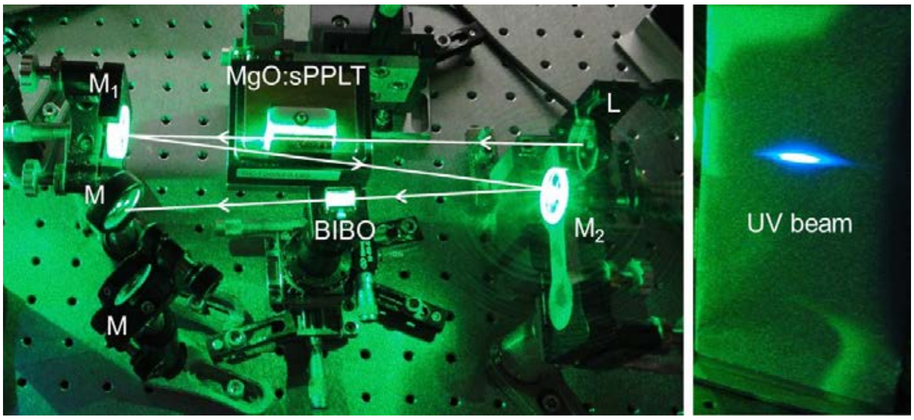

Figure 6.2: Picture of the cw UV source operating in our laboratory (left) and the generated UV beam (right).

6.3 Results and discussion

6.3.1 Power scaling

In order to characterize our UV source, we performed the power scaling measurement of the generated UV radiation at the output of the SFG stage. Figure 6.3 shows the variation of single-pass UV power generated in BIBO as a function of input fundamental power to the SHG stage, where it can be seen that we achieved as much as 68 mW of UV power at 354.7 nm for a fundamental power of 27.8 W at 1064 nm. During the measurements, as the fundamental power is increased, the phase-matching temperature of MgO:sPPLT crystal is always adjusted to generate maximum UV power. Also shown in Fig. 6.4 is the power and efficiency scaling measurement of single-pass SHG at 532 nm, in MgO:sPPLT crystal. While generating maximum UV power, the SHG power is recorded to be 8.2 W at the input to the SFG stage. At higher fundamental powers beyond 20 W, SHG efficiency is observed to be saturated providing a maximum SHG efficiency of 29%. The ratio of SHG to the fundamental power varied from 0 to 0.3 during the UV power scaling measurement. In order to study the effect of SHG to fundamental power ratio, we changed the temperature of the MgO:sPPLT crystal away from optimum phase-matching condition, thereby reducing the SHG power and increasing the undepleted fundamental, while pumping at the maximum available fundamental power of 27.8 W. However, we found that UV power is always maximized when the SHG is maximum, indicating that the generated UV power is limited by the available SHG power. Further, fixing the phase-matching temperature at its optimum value to generate maximum SHG power, and pumping beyond 20 W of fundamental power, we found that the generated UV power is strongly affected by the depletion in the fundamental power, resulting in a >5% drop in the UV power associated with fundamental beam quality degradation, which soon reached a stable, steady state condition with no further reduction in the output UV power. Under certain conditions we were able to generate UV power >70 mW, however it was not stable.

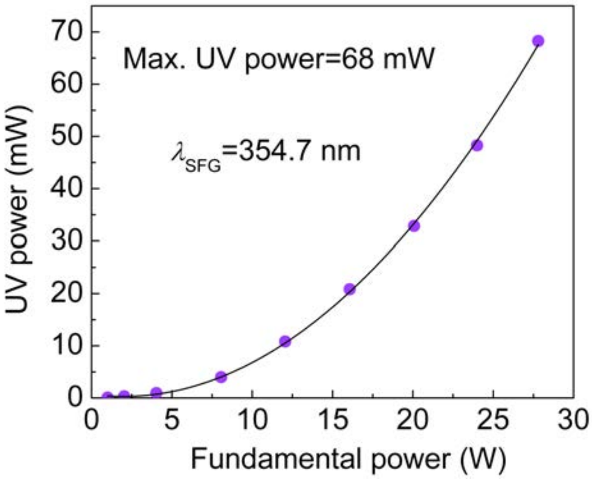

Figure 6.3: Variation of the cw UV power as a function of fundamental power at the output of the SFG stage.

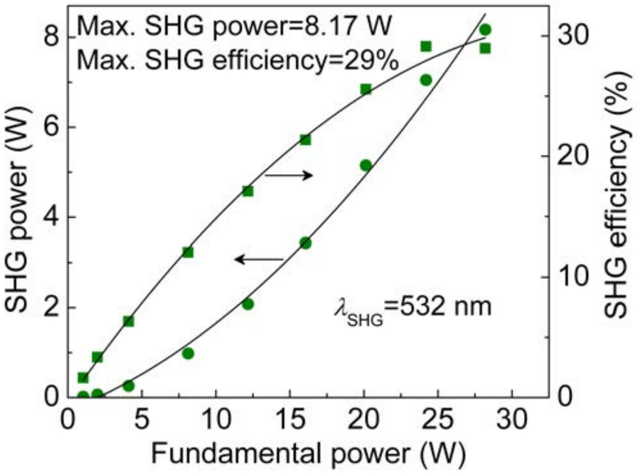

Figure 6.4: Dependence of the measured cw SHG power and the corresponding conversion efficiency on the incident fundamental power at the output of SHG stage.

6.3.2 Power stability and spectrum

After continuous operation of the UV source over >10 hours at maximum fundamental power, we observed a ~30% drop in the UV power, which could be retrieved by translating the BIBO crystal, to use a new portion of the crystal. This drop in the output UV power is attributed to the AR-coating damage on the exit face of the BIBO crystal which was also previously observed in well-established materials such as LBO [114]. Further studies are necessary to understand the origin of this damage. In order to avoid any further damage to the BIBO crystal, we limited the UV power to ∼50 mW with reduced fundamental power in the rest of our measurements.

We have recorded the long-term power stability of the generated UV at ∼50 mW of output power. The results are presented in Fig. 6.5, where it can be seen that the UV output exhibits a passive power stability better than 3.2% rms over 2 hours and 1.5% rms over 50 minutes. Also shown in the inset of Fig. 6.5 is the spectrum of the generated UV radiation centered at 354.7 nm, measured using a spectrometer with a resolution of 0.27 nm (OceanOptics, HR4000). As the fundamental and the SHG are measured to be single-frequency with a linewidth of 89 kHz and 6.5 MHz, respectively, it is expected that the generated UV is also single-frequency. However, we were not able to measure the linewidth of the UV output due to a lack of suitable optics for our Fabry-Perot interferometer.

6.3.3 Frequency stability and beam quality

In order to study the frequency deviation of our single-pass UV source, we recorded the output wavelength as a function of time. The frequency stability of the generated UV radiation, measured at ∼50 mW of output power using a wavemeter (High finesse, WS/U-30) with a resolution of 5 MHz, is shown in Fig. 6.6. Under free-running conditions and in the absence of thermal isolation, the UV output exhibits a peak-to-peak frequency deviation <437 MHz over the >2.5 hours, measured at a central wavelength of 354.7945 nm.

The far-field energy distribution of the UV beam at 354.7 nm, together

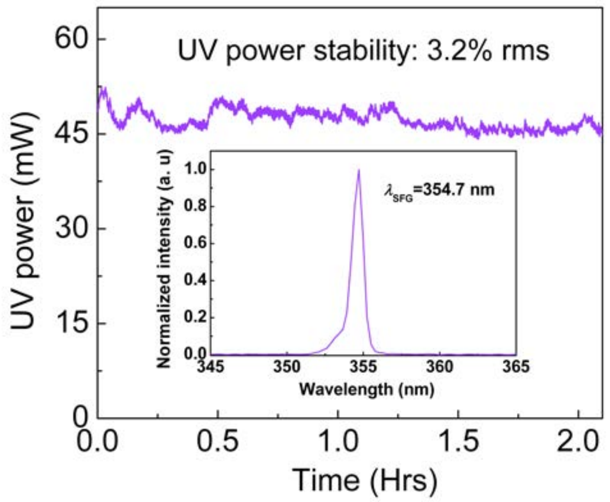

Figure 6.5: UV output power stability at 50 mW over >2 hours. Inset: UV spectrum measured at maximum output power.

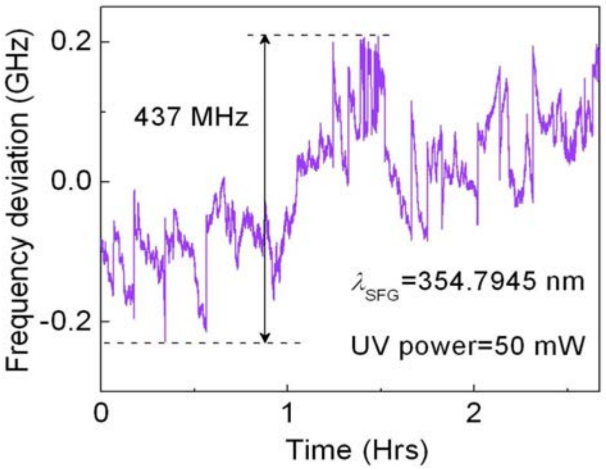

Figure 6.6: Long-term frequency stability of the generated UV output at 354.7945 nm, over a period of >2.5 hours.

with the intensity profiles and the Gaussian fits along the two orthogonal axes measured at the output of the SFG stage are shown in Fig. 6.7. The UV beam exhibits an ellipticity of 66% due to the spatial walkoff between the fundamental, green and UV beams, but can be readily circularized using suitable cylindrical optics. In order to confirm a Gaussian distribution, we measured the M^2 factor of the UV beam at the highest available fundamental power, using a f=100 mm focusing lens and scanning beam profiler, resulting in $M_x{}^2<1.6$ and $M_y{}^2<1.8$, indicating a TEM_{00} spatial mode.

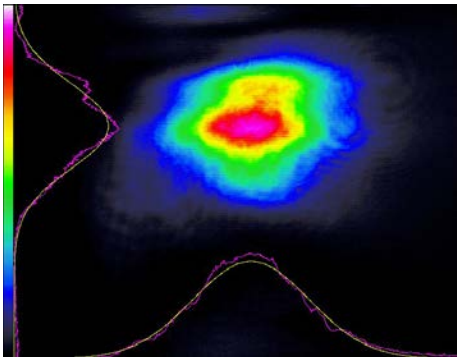

Figure 6.7: Far-field energy distribution and intensity profiles of the generated UV beam at maximum output power.

6.4 Conclusions

In conclusion, we have demonstrated for the first time, a compact Yb-fiber-laser-pumped cw UV source based on BIBO using single-pass SFG of fundamental at 1064 nm and second-harmonic radiation at 532 nm generated by 1^{st}-order QPM interaction in MgO:sPPLT. The cw UV source provides as much as 68 mW of single-frequency power at 354.7 nm with a passive stability better than 3.2% rms over 2 hours and frequency stability better than 437 MHz over >2.5 hours in an elliptic TEM_{00} spatial mode with $M_x{}^2<1.6$ and $M_y{}^2<1.8$, which can be readily improved using suitable cylindrical beam shaping optics. The practical output power and compact fiber-based design together with high stability and good beam quality make the device viable source of cw UV radiation for many applications.

Chapter 7

Dual-wavelength, ARR-coupled, cw OPO

This chapter constitutes the following publication:

1. *Dual-wavelength interferometrically-coupled continuous-wave optical parametric oscillator*
   K.Devi, S. Chaitanya Kumar, A. Esteban-Martin,
   and M. Ebrahim-Zadeh
   Laser and Photonics Reviews, submitted (2013)

7.1 Motivation

For many scientific and technological applications such as spectroscopy, frequency metrology, differential absorption lidar, and nonlinear frequency conversion, high-power coherent dual-wavelength light sources are of great interest. In particular, the ability to produce two closely spaced tunable wavelengths is important for generation of terahertz radiation [29,115,116]. Optical parametric oscillators (OPOs) are well-established coherent sources, capable of providing tunable wavelengths from the ultraviolet to mid-infrared [5]. The generated wavelengths in an OPO are determined simultaneously by energy conservation and phase-matching conditions. Thus, in a conventional OPO, the closest signal and idler wavelengths can be generated only near degeneracy, but in practice this is challenging due to instabilities associated with double resonance. On the other hand, away from degeneracy, signal and idler pairs with arbitrary wavelengths cannot be generated, due to the constraints imposed by energy conservation and phase-matching. In order to overcome these limitations, various schemes based on dual-crystal parametric amplification, double-pass in a single crystal and pump-enhanced OPO have been reported earlier [115, 116]. However, these configurations suffer from drawbacks such as pump beam quality degradation affecting the efficiency, thermal effects and damage to the nonlinear crystal. Recently, to overcome these limitations, a dual-wavelength continuous-wave (cw) OPO using two nonlinear crystals has been reported, generating signal (idler) pairs with frequency separation down to 0.55 THz. In this scheme, the minimum wavelength separation is limited by the parametric gain overlap of the nonlinear crystals [117]. As such, one may also consider alternative approaches that would avoid coherent coupling between the two resonant waves in close proximity, thus permitting the generation of signal (idler) wavelength pairs with indefinitely close separation.

In this chapter, we demonstrate such a technique by using an antiresonant ring (ARR) interferometer to couple two cw OPO cavities. Recently, such an approach has been demonstrated in femtosecond OPOs [118]. In cw regime, we have demonstrated the use of the ARR interferometer for optimum output coupling [103], as discussed in chapter 4, and mode-locking [119], which will be discussed in section 8.1. Here, we demonstrate the use of the ARR interferometer for dual-wavelength generation in cw OPOs, for the first time, providing two distinct signal (idler) wavelength pairs that can be independently and arbitrarily tuned to indefinitely close separation, through degeneracy, and beyond. Using two cw singly-resonant OPOs connected with a common ARR interferometer, we generate signal waves with frequency separation of 0.8 THz, limited by measurement and show their overlap at 951 nm. The architecture provides high intracavity power at both signal waves within the ARR, while avoiding coupling between the two circulating fields.

7.2 Experimental setup

The configuration of ARR-coupled cw OPO is shown in Fig. 7.1. The single pump source used in the experiment is frequency-doubled, diode-pumped cw Nd:YVO_4 laser (Coherent, Verdi V-10), delivering up to 10 W of output power at 532 nm in a single-frequency, linearly-polarized beam with M^2<1.1. The pump radiation is divided into two beams (P_1 and P_2), using a combination of a half-wave plate (H_1) and a polarizing beam-splitter (PBS), and the two beams then separately pump two OPOs (OPO-1 and OPO-2). The half-wave plates, H_2 and H_3, are used to control the pump polarization for phase-matching in the two nonlinear crystals, X_1 and X_2. The crystals are identical 30-mm-long MgO:sPPLT, each with a single grating period of Λ=7.97 μm. They are housed in separate ovens, whose temperature can be controlled from room temperature to 200 ^{o}C with a stability of ±0.1 ^{o}C. The crystal faces are antireflection-coated (R<0.5%) over 850–1064 nm, with high transmission (T>98%) at 532 nm. The residual reflectivity of the coating over the idler range of 1064–1400 nm is 0.5%–15%. Using two identical lenses, L_1 and L_2 (f=150 mm), we focused the pump beams to waist radii, $w_{p1}\sim w_{p2}\sim$31 μm, at the center of X_1 and X_2. The OPO-1 is configured in a standing-wave cavity comprising two concave mirrors, M_1 and M_2, with an ARR in the folded arm. The ARR consists of a beam-splitter (BS) and two plane mirrors, M_3 and M_4. The OPO-2 is also configured in standing-wave cavity identical to OPO-1, using two concave mirrors, M_5 and M_6, and shares the same ARR incorporated in the folded arm. However, unlike OPO-

1, in order to integrate the ARR into OPO-2, we used three additional plane mirrors, M_{7-9} in the folded arm. All mirrors were highly reflecting for the signal (R>99.7% @ 840-1020 nm), and transmitting for the pump (T>98% @ 532 nm) and idler (T>97% @ 1100-1400 nm), thus ensuring single-pass pumping and singly-resonant signal oscillation in both OPOs. The total cavity length of OPO-1 is L_{OPO-1}=106.6 cm, which is the sum of the standing-wave cavity length ($2L_{linear-1}$=2x45.5 cm) and the length of the ARR (L_{ring}=15.6 cm), while for OPO-2 it is $L_{OPO-2}=2L_{linear-2}+L_{ring}$=112.6+15.6=128.2 cm. The BS is a UV fused silica plate (12.5-mm-diameter, 3-mm-thick) with broadband coating over 700–1100 nm, available in our laboratory The alignment of the ARR is similar to that demonstrated in chapter 4, except that here, in order to couple the two OPOs while avoiding any perturbation in one due to the other, we arrange the incident angle (θ_{BS}) on the BS for near-zero output coupling. Thus, the ARR behaves as two interlaced, but independent mirrors, highly reflecting at signal wavelength for both OPOs.

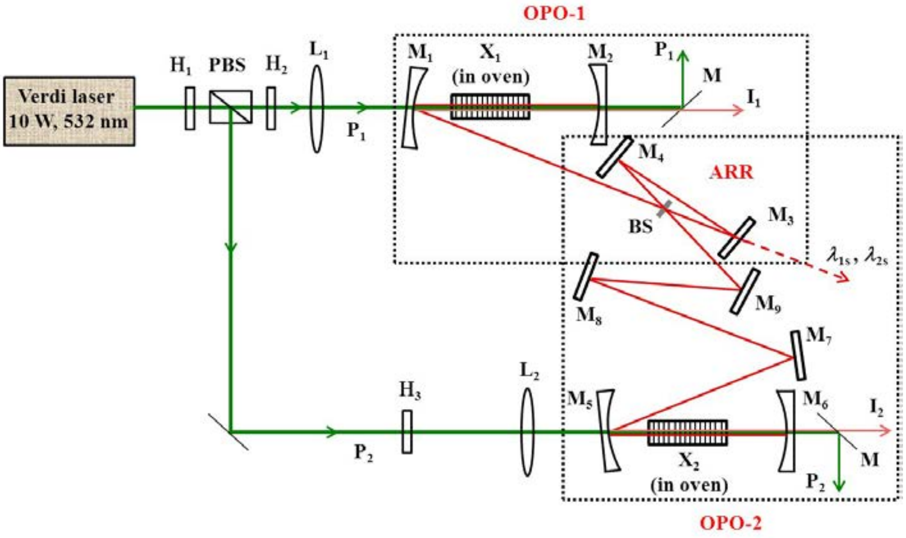

Figure 7.1: Experimental setup of the ARR-coupled cw OPO. H_{1-3}: Half-wave plates, PBS: Polarizing beam-splitter, P_1, P_2: Pump beams, $L_{1,2}$: Lens, M_{1-9}: Cavity mirrors, $X_{1,2}$: MgO:sPPLT crystals, M: Dichroic mirrors, BS: Beam-splitter, λ_{1s}, λ_{2s}: Dual signal wavelengths leaked through M_3, $I_{1,2}$: Idler beams.

Photograph of the ARR-coupled cw OPO system operating in our laboratory is shown in Fig. 7.2. The resonator mirrors, nonlinear crystals, OPO-1, OPO-2, and ARR interferometer are marked in accordance with the schematic of the experimental configuration as shown in Fig. 7.1.

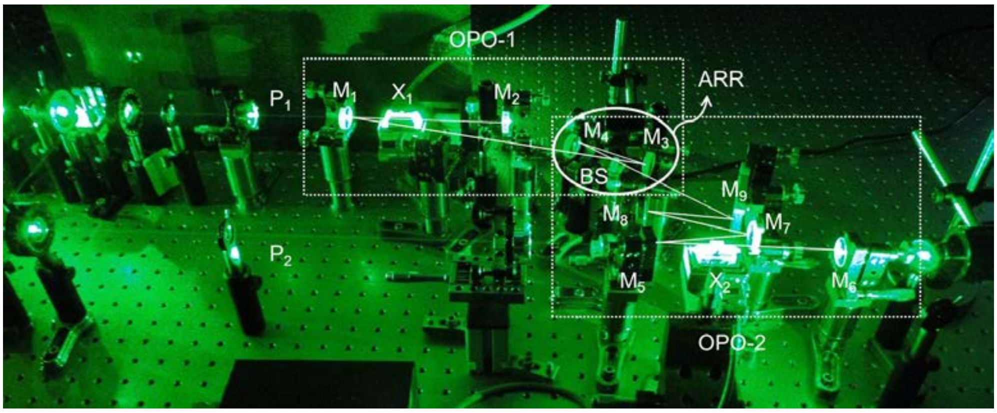

Figure 7.2: Picture of the ARR-coupled cw OPO operating in our laboratory.

7.3 Results and discussion

7.3.1 Charaterization of the ARR interferometer

To determine near-zero output coupling angle for the BS, we initially characterized the ARR externally. As the 1^{st} surface of BS faces OPO-1 and 2^{nd} surface faces OPO-2, we performed the characterization consecutively in both directions, as perceived by the signal beams from the two OPOs. We measured the input power to the ARR and the output power from the ARR at different angles, θ_{BS}, and calculated the transmission of the ARR, T_{ARR}, at a fixed signal wavelength of 951 nm. Figure 7.3 shows the ARR transmission as a function of θ_{BS} for both BS surfaces. With the 1^{st} surface, the transmission remains minimum (T_{ARR}=0.3%) at smaller angles of $5^o<\theta_{BS}<15^o$. With further increase of θ_{BS} beyond 15^o, T_{ARR} increases to 3.3% at $\theta_{BS}=35^o$. The transmission of the ARR with input from the 2^{nd} surface at large angles

(θ_{BS}>25^o) is qualitatively the same as that with input from the 1st surface. However, in this case, the minimum transmission was measured to be 0.7% for angles 5^o<θ_{BS}<15^o. The difference in the ARR transmission is attributed to the broadband coating only on the 2^{nd} surface of the BS. Thus, we fixed θ_{BS}=12^o for minimum transmission through both surfaces and incorporated the ARR inside OPO-1 and OPO-2.

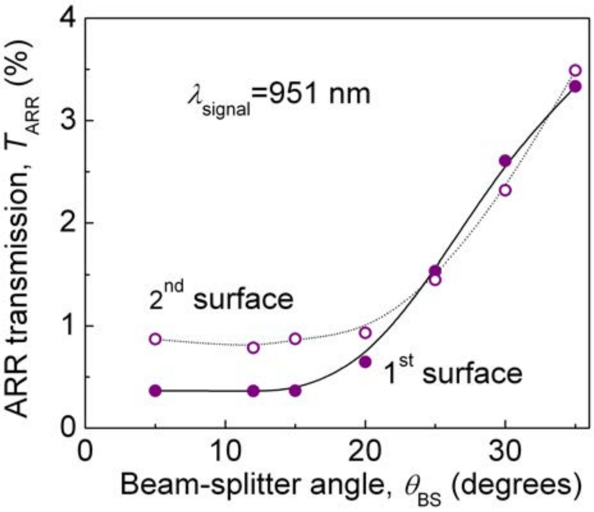

Figure 7.3: Transmission of the ARR interferometer as a function of BS angle.

Figure 7.4 shows the direction of signal waves from OPO-1 and OPO-2, and within the ARR. As seen, the architecture provides high intracavity powers for both resonant wavelengths in the same direction, inside the ARR.

7.3.2 Tuning capability of ARR-coupled cw OPO

We optimized OPO-1 and OPO-2 to achieve equal idler powers of >1W, while pumping simultaneously with pump power of 4.3 W and 5.7 W, respectively. In order to demonstrate versatile tuning capabilities of the ARR-coupled cw OPO, we systematically temperature tuned each OPO and recorded the spectrum of the signal leaking through the ARR mirror (M_3), where high-power, dual-wavelength operation is expected. OPO-1 is temperature tuned from

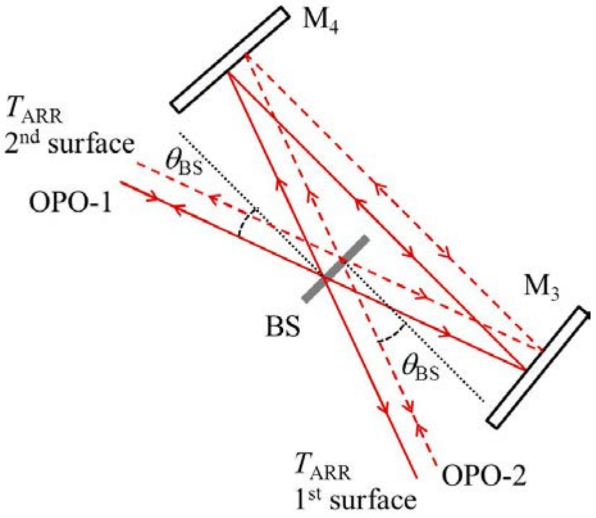

Figure 7.4: Direction of the dual wavelength signal beams to and from the OPOs, and within the ARR.

T$_1$=110 ^{o}C down to 90 ^{o}C, while OPO-2 is tuned from T$_2$=90 ^{o}C up to 110 ^{o}C. The results are shown in Fig. 7.5. As evident, this systematic variation of the temperature enables smooth and continuous tuning of the resonant signal wavelengths with a frequency difference from 6.6 THz, indefinitely down, until they completely overlap and tune through degeneracy, up to 7 THz. At T$_1$=102 ^{o}C (λ_{1s}=949.9 nm) and T$_2$=98 ^{o}C (λ_{2s}=952.5 nm), the difference between the resonant signal frequencies is as low as 0.8 THz, limited by the measurement with the spectrometer. The frequency difference is further reduced by decreasing T$_1$ towards 101 ^{o}C and increasing T$_2$ towards 100 ^{o}C, finally leading to two identical resonant signal wavelengths at 951 nm (T$_1$=101 ^{o}C, T$_2$=100 ^{o}C) oscillating independently in each OPO. The 1 ^{o}C difference in crystal temperatures to generate the same signal wavelength is mainly due to the small difference in the design and calibration of the two ovens. Further decrease in T$_1$ and increase in T$_2$ lead to the crossover of the resonant wavelengths from the two OPOs, confirming arbitrary tuning enabled by the ARR coupling. As seen, the frequency difference between the resonant waves then increases from 1.8 THz (T$_1$=98 ^{o}C, T$_2$=102 ^{o}C) to 7 THz (T$_1$=90 ^{o}C, T$_2$=110 ^{o}C).

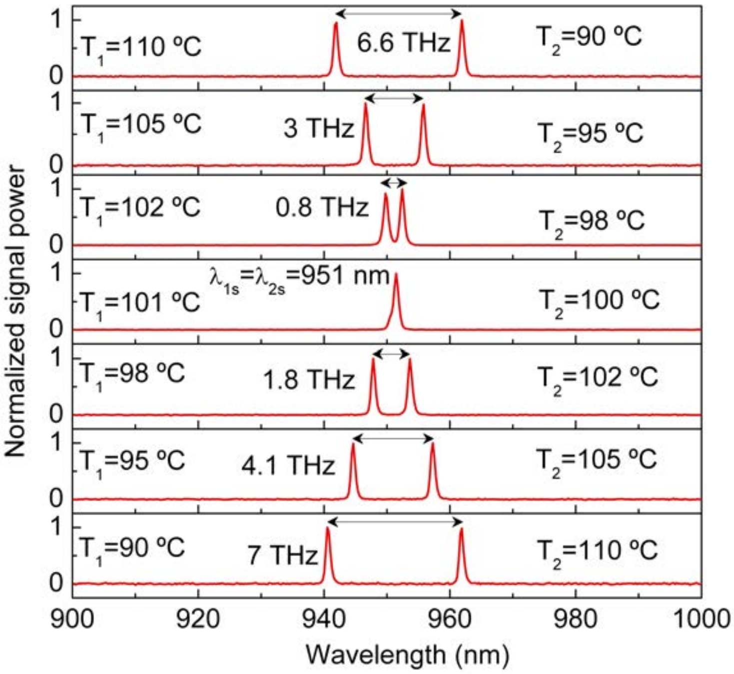

Figure 7.5: Signal spectra from the ARR-coupled, dual-wavelength OPO at independently tunable crystal temperatures, T_1 and T_2.

7.3.3 Single-frequency operation

Maintaining the crystal temperatures at T_1=101 ^{o}C and T_2=100 ^{o}C, we observed the spectrum of the resonant signal waves (λ_{1s}=λ_{2s}=951nm), leaked through the same ARR mirror (M_3), using a confocal Fabry-Perot interferometer (FSR=1GHz, finesse=400). The results are shown in Fig. 7.6. By blocking P_2 and operating OPO-1 at a pump power of 4.3 W, we recorded the typical fringe pattern of the transmitted signal, confirming single-frequency operation of OPO-1 with an instantaneous linewidth of ~20 MHz. Similarly, by blocking P_1 and operating OPO-2 pumped at 5.7 W of pump power, we confirmed single-frequency operation of OPO-2 with a linewidth of ~20 MHz. We further recorded the instantaneous transmission spectrum of both waves together, using the same Fabry-Perot interferometer, and measured the frequency separation of ~220 MHz between the two signal waves relative to each other, as shown in Fig. 7.6. In order to confirm the isolation provided by the ARR at degeneracy, we have measured the output power during simultaneous and individual operation of the OPOs. We have not observed any change in the output idler power from the OPOs. Also, the threshold pump power remains same.

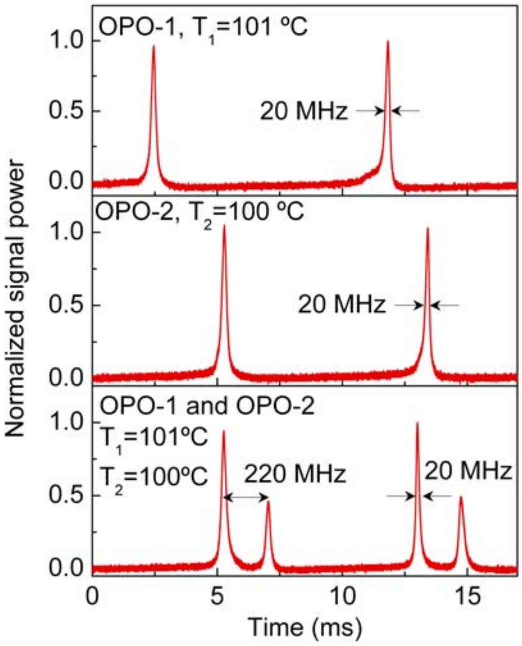

Figure 7.6: Fabry-Perot transmission spectra of the dual signal wavelengths.

7.3.4 Power scaling

To show power scalability of the system, we measured the idler output power as a function of input pump power for both OPOs when oscillating simultaneously, keeping T_1=101 ^{o}C and T_2= 100 ^{o}C. The results are shown in Fig. 7.7(a). For OPO-1, the idler power increases linearly up to a 4.5 W of pump power, while for OPO-2 it is linear up to 5 W of pump, beyond which there is slight evidence of saturation, which could be attributed to thermal effects, pump depletion and backconversion. We achieved a maximum idler power of 1.6 W from OPO-1 for a pump power of 6.3 W, while OPO-2 is close to threshold using the remaining 3.7 W of pump. Similarly, 1.4 W of idler is generated from OPO-2 for 7 W of pump power, with OPO-1 operating near threshold at a pump power of 3 W. Further increasing the pump power to one OPO makes the other OPO unstable until it finally ceases operation. OPO-1 and OPO-2 have an operation threshold power of 2.8 W and 3.2 W, respectively.

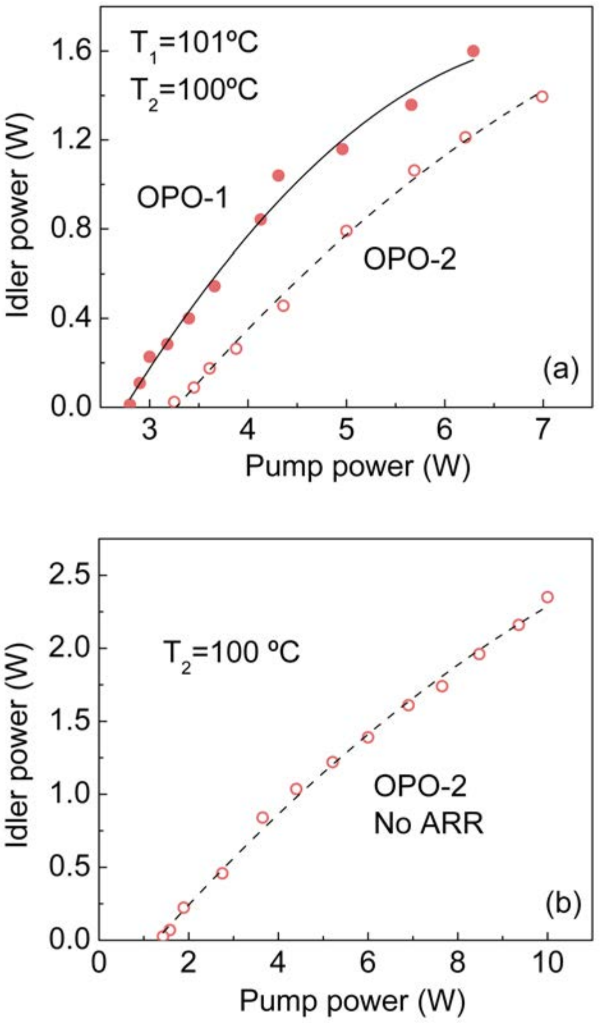

Figure 7.7: (a) Idler output power from OPO-1 and OPO-2 versus pump power, with both OPOs in simultaneous operation. (b) Power scaling of OPO-2 without the ARR.

We also performed power scaling for both OPOs in the short v-cavity configuration by placing highly reflecting mirrors (at signal) in place of the ARR. Each OPO without the ARR was configured with a cavity length of 63 cm.

Both OPOs without ARR showed similar performance, providing maximum idler power of ∼2.3 W for a pump power of ∼10 W with an operation threshold of ∼1.4 W. Figure 7.7(b) shows the power scaling results for OPO-2 without the ARR. As evident, OPO-1 with the ARR incorporated in it shows similar output power as that of the OPO without ARR, at same pump power. However, the lower output power from OPO-2 with the ARR incorporated is due to the longer cavity length and additional mirrors (M_{7-9}) used. Further, the increase in threshold power for both OPOs with the ARR incorporated, as compared to that of without ARR, is attributed to the additional losses due to the ARR elements, which can be further reduced.

We also confirmed that the incorporation of the ARR did not have any adverse effect on output beam quality, with the signal beam from both OPOs exhibiting TEM_{00} spatial profile.

7.4 Conclusions

In conclusion, we have described a dual-wavelength, ARR-coupled, cw OPO with signal (idler) wavelength pairs which can be independently and arbitrarily tuned through degeneracy and beyond. We have demonstrated frequency separation from 7 THz down to ∼220 MHz at identical signal wavelengths, although there is no limit to the minimum attainable wavelength separation, even to exact degeneracy. Both circulating signal waves provide high intracavity power and narrow linewidth, making the technique particularly attractive for efficient generation of widely tunable terahertz radiation, as well as other potential applications. The approach can also be extended to other spectral regions and operating time-scales.

Chapter 8

Mode-locked, cw OPOs

This chapter constitutes the following publications:

1. *Frequency-modulation-mode-locked optical parametric oscillator*
   A. Esteban-Martin, G. K. Samanta, **K. Devi**, S. Chaitanya Kumar, and M. Ebrahim-Zadeh
   Opt. Letters **37**, 115-117 (2012)
2. *Mode-locked, continuous-wave, singly resonant optical parametric oscillator*
   K. Devi, S. Chaitanya Kumar, and M. Ebrahim-Zadeh
   Opt. Letters **37**, 3909-3911 (2012)
3. *Directly phase-modulation-mode-locked doubly-resonant optical parametric oscillator*
   K. Devi, S. Chaitanya Kumar, and M. Ebrahim-Zadeh
   Opt. Express, submitted (2013)

8.1 Motivation

Since the first indication of mode-locking in ruby laser by Gurs and Muller

[120], there has been tremendous development in the field of mode-locked lasers in terms of mode-locking methods and understanding [57, 58]. For the past few decades, generation of ultrashort pulses has been a primary source of interest due to its manifold of applications in different areas such as material processing, metrology, spectroscopy, optical microscopy, medical domain and nonlinear frequency conversion processes [121, 122]. From active to passive, many mode-locking methods have been exploited for short pulse generation. However, except the Ti:sapphire laser [97, 123] known as the workhorse in the ultrafast regime and the Yb-doped fiber laser, the mode-locked lasers still suffer from the general lack of widespread availability and are tunable in particular wavelength regime only. Hence, efforts have been made to increase their tunability and spectral coverage by deploying nonlinear frequency conversion techniques. The optical parametric oscillators (OPOs) have indeed proved to be a promising candidate towards this goal, as they are the viable sources of widely tunable radiation for spectral regions inaccessible to lasers, operating in all time scales from continuous-wave (cw) to ultrafast femtosecond domain. Due to the lack of gain storage, operation of OPOs in the ultrafast picosecond and femtosecond regime has traditionally relied on the technique of synchronous pumping by using mode-locked pump lasers and careful matching of the OPO cavity length to the pump laser repetition rate. However, given the high complexity and cost of the mode-locked lasers as compared to cw lasers, the synchronous pumping approach often result in elaborate system design, increased cost and large size for ultrafast OPOs. It would be desirable, therefore, to consider novel alternative methods for the development of ultrafast OPOs that do not rely on synchronous pumping with mode-locked pump lasers. One such technique could be direct mode-locking of cw OPOs. This approach could enable the generation of tunable ultrashort pulses over wide spectral regions using OPOs by deploying widely available cw pump lasers, thus circumventing the need for ultrafast laser sources and synchronous pumping. Such an ap-

proach was previously attempted in a doubly-resonant oscillator (DRO) under quasi-cw pumping [47] using an acousto-optic modulator (AOM) as the active mode-locking element, where steady-state pulses with nanosecond duration were generated. Also, attempts were made under cw pumping using an AOM in a ring-cavity singly-resonant oscillator (SRO), again providing nanosecond pulses in steady-state operation [60].

In this chapter, we demonstrate for the first time, direct active mode-locking of a cw OPO in both DRO as well as SRO configuration, generating picosecond pulses. In section 8.3, we demonstrate a hybrid mode-locking technique based on the use of an intracavity electro-optic phase modulator (EOM) in combination with an antiresonant ring interferometer (ARR), providing phase-to-amplitude conversion, thus enabling ultrashort pulse generation. A cw DRO has been used and operated near degeneracy to initiate broad signal-idler bandwidths. Using the technique, we generate 730 ps pulses at 160 MHz and 450 ps pulses at 80 MHz. In section 8.4, we demonstrate the direct active mode-locking of the cw DRO, only by deploying intracavity phase modulation, without the use of an ARR interferometer, generating 533 ps pulses at 80 MHz and 471 ps pulses at 160 MHz. In spite of the large spectral signal-idler bandwidths available under near-degeneracy operation, which could be desirable for ultrashort pulse generation, cw DROs suffer from mode-hoping and non-monotonous tuning, which ultimately limit stability in mode-locked operation. On the other hand, cw SROs offer higher passive spectral, temporal, and output power stability, which could result in robust operation under mode-locking. Because of their intrinsic frequency stability, the SROs can also be the favorable design when used together with resonant phase modulators, which are specified for narrowband or single-frequency operation. The combination of cw SRO together with a resonant phase modulator could thus potentially enable the generation of shorter pulses. Hence, it is worthwhile to explore direct mode-locking of cw SROs using resonant phase modulation. In section 8.5, we demonstrate direct active mode-locking of a cw OPO in SRO configuration, based on pure phase-modulation, using the EOM as the single mode-locking element, generating stable pulses of 230 ps duration at 80 MHz repetition rate.

8.2 External charaterization of the EOM

For active mode-locking, in the context of lasers, phase modulators with different modulation frequencies have been used in the past [62, 124–129]. To our knowledge, till date the lowest modulation frequency with EOM used as a single mode-locker for direct active mode-locking is 100 MHz. The resonant EOM (New Focus, Model 4003) used in the present work has central resonant frequency of ν=80 MHz with tunability of ±5 MHz, typical bandwidth of 0.8-1.6 MHz, and quality factor of 36. It is based on a 40-mm-long MgO:$LiNbO_3$ electro-optic crystal with a clear aperture of 2 mm. It has both the faces antireflection (AR)-coated over 1–1.6 µm. In order to study the performance of the EOM, we initially characterized the EOM individually and externally. An Yb-doped fiber laser (IPG Photonics, YLR-30-1064-LP-SF), providing 30 W of single-frequency, linearly-polarized radiation at 1064 nm has been used as the input laser source to the EOM. With 1 W of input power, we observed the single-pass output from the EOM in frequency domain and also in time domain at different modulation depth and modulation frequency. Figure 8.1(a) and 8.1(b) shows the transmission spectrum of the single-pass output through the EOM, measured using a confocal Fabry-Perot interferometer, FPI (Free Spectral Range, FSR=1 GHz, finesse=400) for different modulation depth and frequency, by keeping either of the parameter fixed, respectively. As seen in (i) of Fig. 8.1(a), at minimum modulation depth, μ_1 and resonant frequency of ν=80 MHz, single-frequency spectrum is seen, with instantaneous linewidth of 4.6 MHz. With increase in modulation depth to μ_2 in (ii), keeping ν constant, the amplitude of the central frequency begins to fall and side bands appears on both sides of the central frequency. The amplitude of the side bands increases with increase in modulation depth to μ_3 in (iii). With further increase in modulation depth to μ_4 in (iv), the central frequency starts disappearing, with no central carrier frequency at maximum available modulation depth of μ_5 in (v). The modulator produces 2 side bands on either side of the central frequency, with side band spacing of ~80 MHz. The side band spacing has been observed as independent of the modulation depth. Figure 8.1(b) shows the effect of increase in modulation frequency with modulation depth kept fixed at μ_3. It has been observed that at minimum modulation frequency of ν_1 in (i), the spectrum remains single-frequency with instantaneous linewidth of 4.7 MHz. However, as the modulation frequency is increased, prominent and maximum side bands are seen at ν in (iii) with less significant side bands at other frequencies (ν_2, ν_3 and ν_4).

We also monitored the output from the EOM in time domain using an InGaAs photodetector (20 GHz, 18.5 ps) and a fast oscilloscope (3.5 GHz, 40 GS/s). It is to be noted that the modulation signal applied to the EOM using a RF driver is sinusoidal. At a modulation frequency of ν=80 MHz and increasing the modulation depth from μ_1 to μ_4, we have not observed any modulation in the output. However, keeping the modulation frequency fixed at ν and increasing modulation depth further to the maximum, a slight modulation at a repetition rate of 160 MHz and width of 3 ns has been observed.

We have further calculated the values of different modulation depth, which is the optical phase shift induced by the EOM used. The amplitude of the central carrier frequency is given by $[J_0(\mu)]^2$, where J_0 is the Bessel function of zero order and argument μ is the optical phase shift or the modulation depth [124]. The sidebands seen in Fig 8.1(a) for different modulation depth, shows the Bessel function amplitudes, as shown in Fig. 8.2. Comparing the amplitude of the central carrier frequency obtained from the transmission spectrum at different modulation depth of EOM in Fig. 8.1(a), with the amplitude of $[J_0(\mu)]^2$ from the theoretical Bessel plot in Fig. 8.2, the modulation depth of

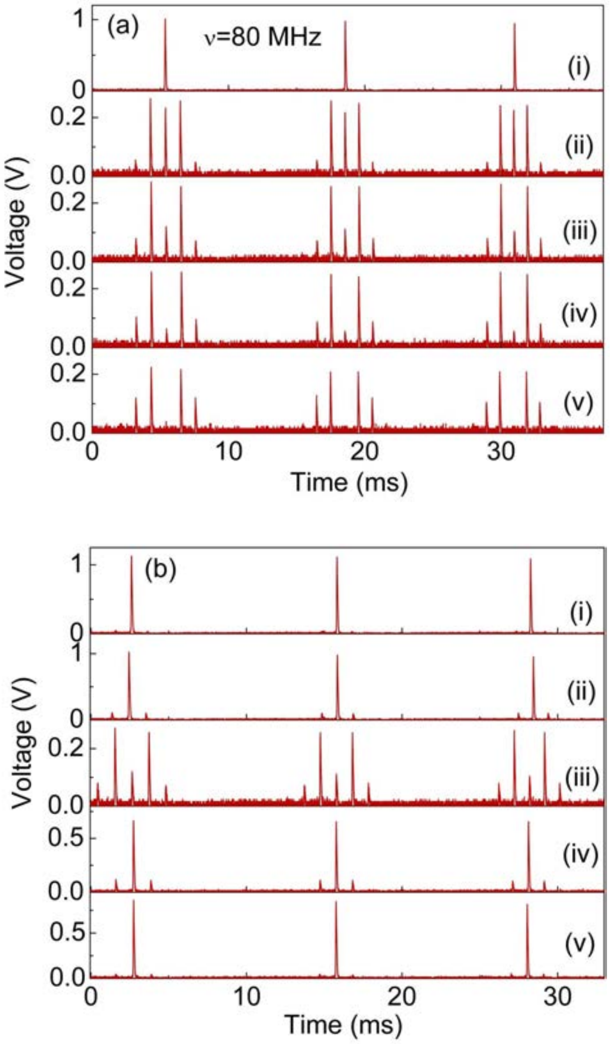

Figure 8.1: Single-pass EOM output spectrum (a) at ν=80 MHz for different modulation depth (μ_1<μ_2<μ_3<μ_4<μ_5) of (i) μ_1 (ii) μ_2 (iii) μ_3 (iv) μ_4 (v) μ_5 and (b) for fixed modulation depth of μ_3 at different modulation frequency (ν_1<ν_2<ν<ν_3<ν_4) of (i) ν_1 (ii) ν_2 (iii) ν (iv) ν_3 (v) ν_4.

μ_1, μ_2, μ_3, μ_4 and μ_5 has been calculated to be 0, 1.63, 1.83, 1.99 and 2.4 radians, respectively.

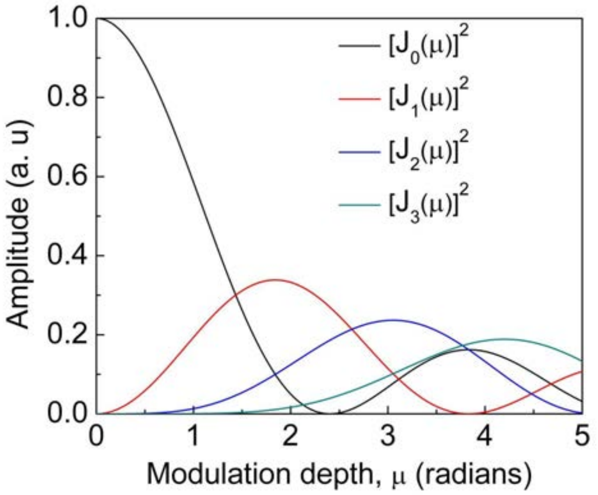

Figure 8.2: Bessel function amplitude of order 0, 1, 2 and 3, representing the amplitudes of carrier frequency, 1^{st}, 2^{nd}, and 3^{rd} side bands, respectively, with modulation depth as argument.

8.3 Mode-locking of cw DRO using ARR interferometer

8.3.1 Experimental setup

The schematic of the experimental setup is shown in Fig. 8.3. The fundamental pump source used is frequency-doubled, diode-pumped cw Nd:YVO$_4$ laser (Coherent, Verdi V-10), delivering up to 10 W of output power at 532 nm in a single-frequency, linearly-polarized beam with M^2<1.1. To maintain stable laser output characteristics, we operated the pump laser at maximum power and used a combination of a half-wave plate (HWP) and a polarizing beam-splitter (PBS) cube as power attenuator. A second HWP was used to adjust the pump polarization relative to the crystal orientation. The nonlinear crystal is 30-mm-long MgO:sPPLT with a single grating period of 7.97 μm, housed in an oven with a temperature stability of ±0.1 ^{o}C. The crystal faces are antireflection-coated (R<0.5%) over 850–1064 nm, with high transmission (T>98%) at 532 nm. The residual reflectivity of the coating over the idler range of 1064–1400 nm is 0.5%– 15%. Using a lens of focal length, f=150 mm, the pump beam is focused to a waist radius of ~31 μm ($\xi\sim1.2$) at the center of the crystal. The OPO cavity design ensures optimum overlap of pump and resonant waves at the center of the crystal ($b_p \sim b_{s/i}$), with a signal/idler waist radius of ~46 μm, where b_p, $b_{s/i}$ are the confocal parameters of the pump and signal/idler, respectively. The OPO is configured in a standing-wave cavity comprising two concave mirrors, M_1 and M_2 (r=100 mm), a plane mirror (M_3) in one arm, a concave mirror, M_4 (r=1000 mm) and an ARR interferometer formed by two plane mirrors (M_5 and M_6) and a beam-splitter (BS) integrated into the other arm. The EOM, described in section 8.2, is incorporated into the ARR. Mirror, M_3, is mounted on a translation stage to adjust the length of the OPO, and the beam diameter through the aperture of the EOM inside the ARR is adjusted using mirror M_4. All the mirrors are highly transmitting (T>97%) for the pump and highly reflecting (R>99%) for the signal and idler over 1000-1080 nm, thus ensuring DRO operation. The BS is a UV fused silica plate (12.5-mm-diameter, 3-mm-thick) with a broadband coating over 700–1100 nm. We arranged the incident angle (θ_{BS}) on the BS for minimum transmission from the ARR. The DRO is operated near degeneracy by keeping the crystal temperature at 51.5 ^{o}C. The total optical length (L_{DRO}) of the DRO cavity including the linear arm, L_{linear}=143 cm, and ARR ring, L_{ring}=90 cm, when synchronized to the modulation frequency (ν=80 MHz) of the EOM, is 3.7 m, where $L_{DRO}=2L_{linear}+L_{ring}=c/\nu$, and c is the speed of light. Figure 8.4 shows the picture of the mode-locked cw DRO operating in our laboratory, where the DRO cavity mirrors, ARR elements and the nonlinear crystal are marked.

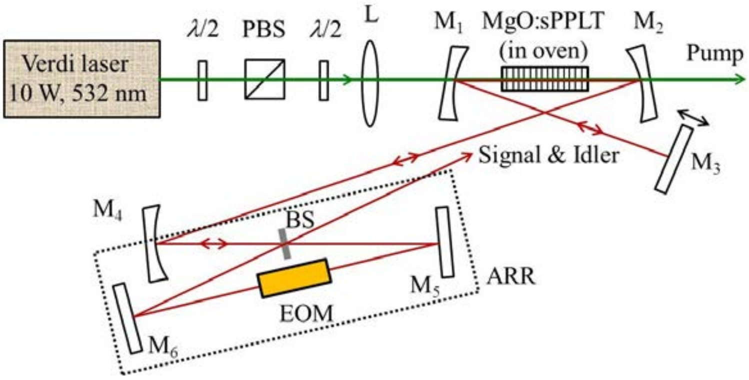

Figure 8.3: Schematic of the continuous-wave, mode-locked DRO. $\lambda/2$: Half-wave plate, PBS: Polarizing beam-splitter, L: Lens, M_{1-6}: Cavity mirrors, EOM: Electro-optic phase modulator, BS: Beam-splitter.

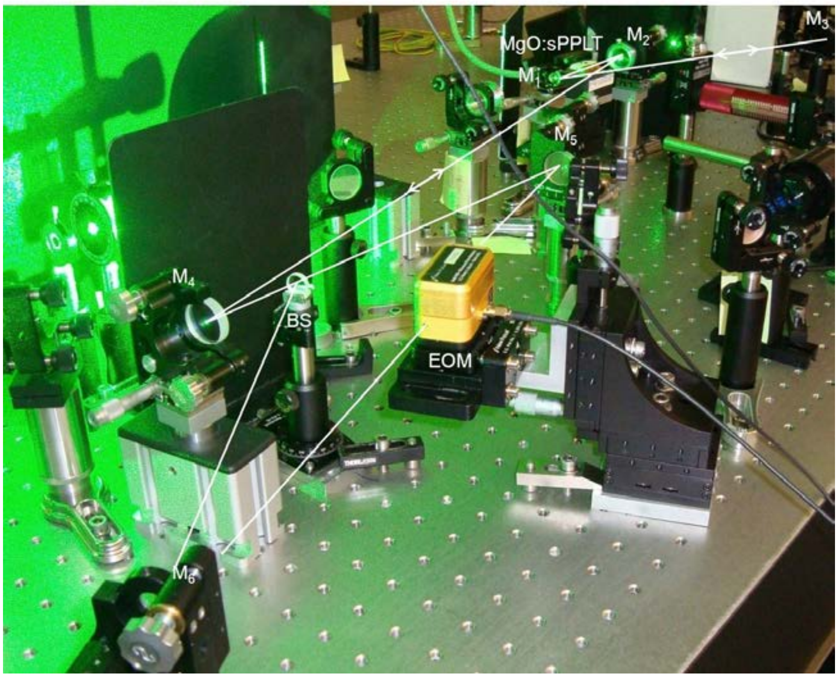

Figure 8.4: Picture of the setup operating in our laboratory.

8.3.2 Phase-to-amplitude modulation conversion

We performed external characterization of the ARR interferometer with the EOM placed at the centre of the ARR between mirrors M_5 and M_6, prior to integration into the cw DRO. We operated the cw DRO near degeneracy, providing signal wavelength, λ_{signal}=1053 nm, and idler wavelength, λ_{idler}=1075 nm, and used the output of the cw DRO as the input to the ARR. The output from the cw DRO (~1W) was extracted using an output coupler (OC) of transmission ~3% placed between M_2 and M_4. We observed the output from the ARR in time domain using the InGaAs photo-detector (20 GHz, 18.5 ps) and the fast oscilloscope (3.5 GHz, 40 GS/s). The result is shown in Fig. 8.5(a). The moment the EOM is switched ON, a finite electric field at 80 MHz is applied to the electro-optic crystal of the EOM, which in turn slightly modulates the output of the ARR. However, after a while, as seen, the ARR output is nearly constant when the modulation depth of the EOM is kept at μ_1=0 while adjusting the modulation frequency to ν=80 MHz. With the increase in modulation depth from 0 to maximum, the ARR produces distinct output modulation with constant repetition rate, but increasing amplitude. As evident from Fig. 8.5(b), at the maximum modulation depth, μ_5=2.4 rads, the output pulse duration is 3.9 ns at 80 MHz, determined by the resonant frequency of the EOM.

In a conventional ARR, as described in section 4.1 of chapter 4, the power transmitted out of the ring (T_{ARR}) and the power reflected from the ring towards the input beam (R_{ARR}) are constant and depend on the ratio of transmittance (T) and reflectance (R) of the beam-splitter. However, by modulating the phase of the clockwise and counter-clockwise beams in the ARR, one can introduce a time delay in the modulated signals. The recombination of these clockwise and counter-clockwise phase-modulated signals then leads to the conversion of internal phase modulation into amplitude modulation. This

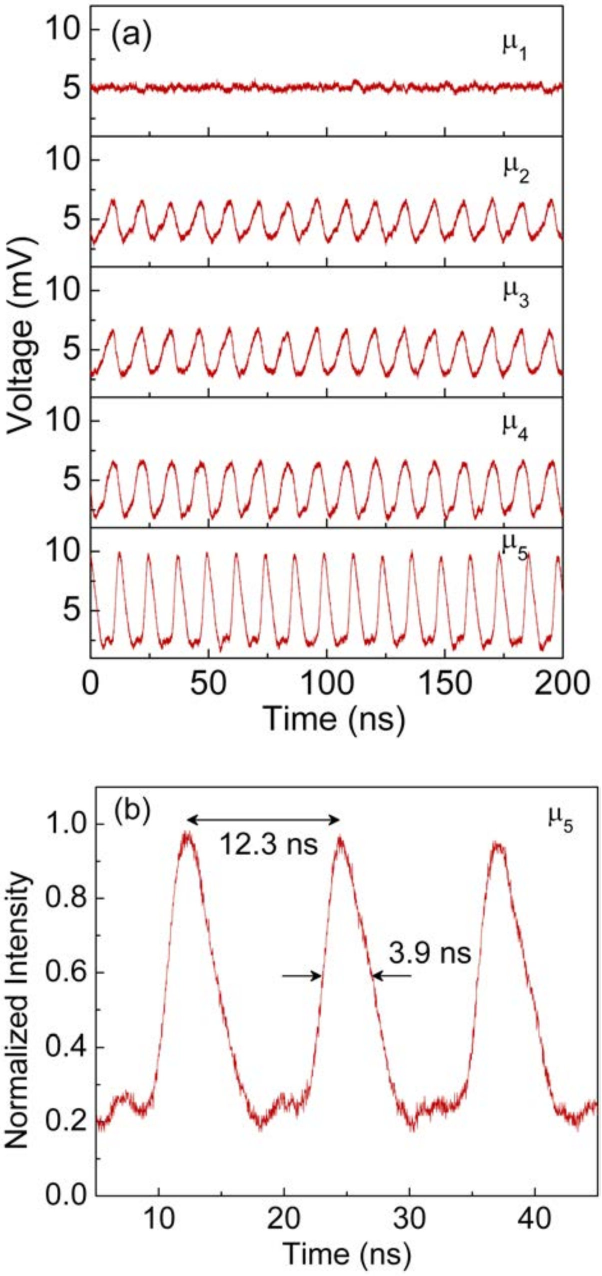

Figure 8.5: (a) Temporal output of the phase-modulated ARR when deployed external to the DRO. (b) Zoomed temporal output for maximum modulation depth.

concept has been earlier reported in the context of lasers [91].

8.3.3 Mode-locked pulse generation

In order to actively mode-lock the cw DRO, we incorporated the phase-modulated ARR into the DRO cavity. With the crystal temperature kept at 51.5 ^{o}C, the cw DRO with the ARR and EOM incorporated provides an output power of 262 mW for 9.7 W of pump power and has an oscillation threshold of 3.5 W. The higher oscillation threshold power as compared to conventional DRO cavity is mainly attributed to the losses introduced by EOM, ARR elements and longer cavity length.

We then activated the EOM, and systematically changed the modulation depth of the EOM, while monitoring the modulation frequency simultaneously. The output of the DRO from ARR is monitored in time domain for different modulation depths at modulation frequency of $\nu \pm \Delta\nu$. This change in modulation frequency ($\Delta\nu$) on either side of the EOM resonant frequency is very small and is of the order of kHz. Figure 8.6(a) shows the temporal output. At μ_1=0, some perturbation is seen, however with the increase in modulation depth to μ_2=1.63 rads, pulses of 780 ps duration with 160 MHz repetition rate are observed. These pulses even shorten down to 730 ps when we increase the modulation depth to μ_3=1.83 rads. With the increase in modulation depth to μ_4=1.99 rads, pulses with alternatively equal amplitude are observed with high intensity pulses at 790 ps and low intensity pulses at 580 ps duration. Further increase in modulation depth to the maximum value leads to the generation of pulses with repetition rate of 80 MHz and pulse duration of 450 ps. Figure 8.6(b) and 8.6(c) shows the zoomed version of stable pulses at repetition rate of 160 MHz and 80 MHz, respectively.

Pulses with 80 MHz repetition rate are also observed when modulation depth is kept fixed at μ_3=1.83 rads and modulation frequency is changed to

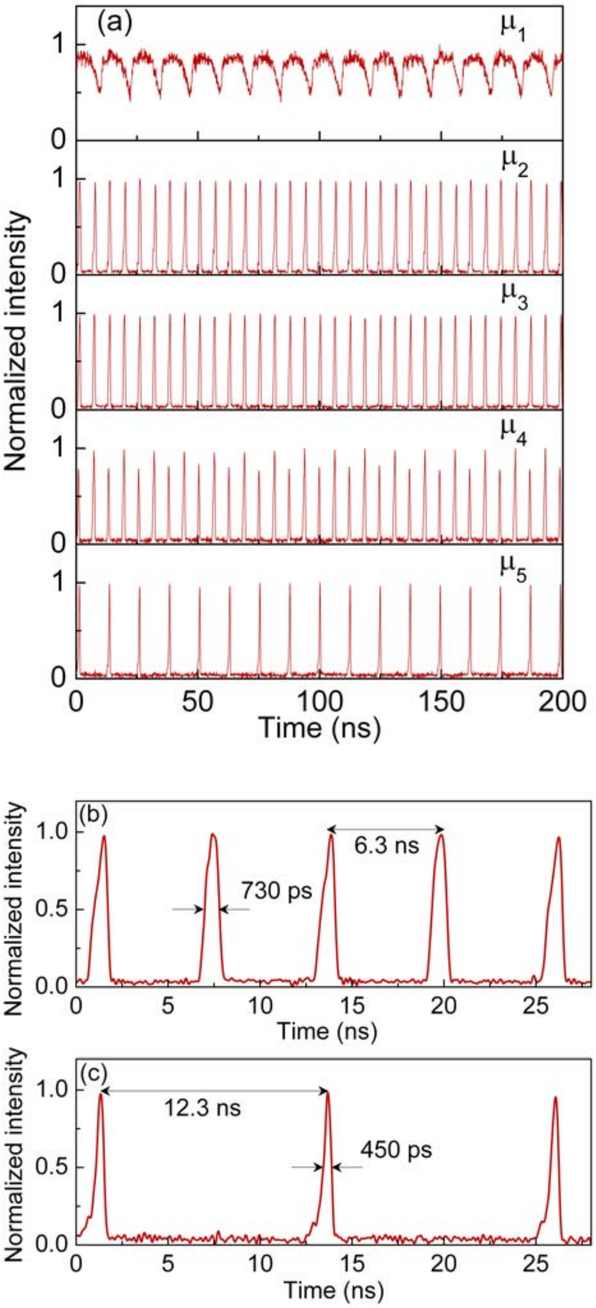

Figure 8.6: (a) Pulse train obtained with increase in modulation depth, at modulation frequency of $\nu \pm \Delta\nu$. (b) Zoomed 730 ps pulses at 160 MHz repetition rate. (c) Zoomed 450 ps pulses at 80 MHz repetition rate.

$\nu \pm \Delta\nu'$. The change in modulation frequency, $\Delta\nu'$, is again of the order of kHz, where $\Delta\nu' > \Delta\nu$. The effect of change in modulation frequency, while keeping modulation depth fixed at μ_3=1.83 rads, is shown in Fig. 8.7.

As evident, at $\nu - \Delta\nu'$, stable pulses of 450 ps duration at 80 MHz repetition are generated. If the modulation frequency is increased to ν, which is the resonant frequency of the EOM, a strong perturbation is observed, without any pulse formation. However, with further increase in modulation frequency to $\nu + \Delta\nu'$, stable pulses at 80 MHz repetition rate with pulse duration of 550 ps are observed again.

It is thus evident that to obtain stable short pulses at 160 MHz and 80 MHz repetition rate, a careful adjustment of the modulation frequency or precise change in cavity length over a narrow zone at higher value of modulation depth is required.

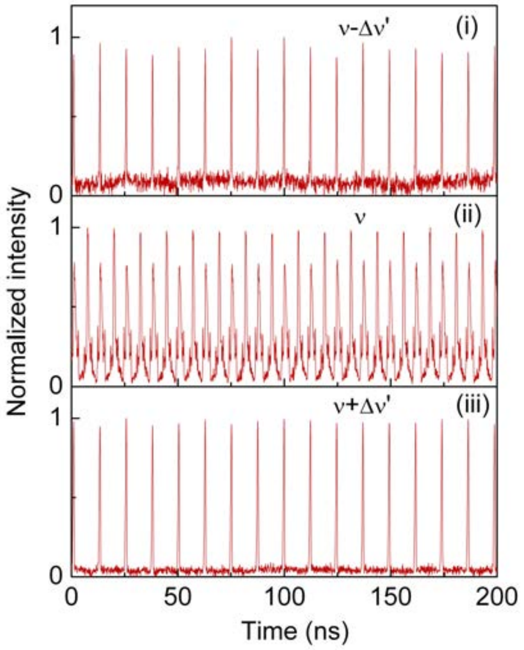

Figure 8.7: Temporal output at modulation depth of μ_3=1.83 rads and modulation frequencies of (i) $\nu - \Delta\nu'$, (ii) ν, and (iii) $\nu + \Delta\nu'$.

8.3.4 Output spectrum

We also measured the DRO output spectrum under three operating conditions, cw operation (EOM switched OFF), and mode-locked when generating 160 MHz and 80 MHz repetition rate pulses. The results are shown in Fig. 8.8. In cw operation, we recorded relatively narrow signal and idler spectra centered at 1053 nm and 1075 nm, respectively. However, for the 160 MHz pulses spectral broadening over 12 nm is observed about signal (1045-1057 nm) and idler (1071-1083 nm). On the other hand, for the 80 MHz pulses the signal and idler branches lock together and form a single broadband spectrum spanning 34 nm over 1047-1081 nm. Similar broadening of the spectra is observed when the separation between the signal and idler wavelengths is slightly varied by temperature tuning the cw DRO away from degeneracy. If we tune the cw DRO to degeneracy by tuning the temperature to 50 ^{o}C, further bandwidth broadening is observed. Figure 8.9 shows the results at degeneracy. As seen, during cw operation, the signal and idler are centered at 1058 nm and 1070 nm, respectively. However, under mode-locked operation the signal and idler become locked and broadened over 1045-1083 nm and 1054-1074 nm for 160 MHz and 80 MHz pulses, respectively. The difference in the amplitude of signal and idler spectrum is attributed to the difference in crystal coating losses and mirror reflectivities. Assuming Gaussian pulse shape and a time-bandwidth product of 0.44, the transform limited pulse duration for 34 nm bandwidth spectrum has been calculated to be $\sim$48 fs. Clearly, the observed broadband spectrum is not fully contributing to the generation of the output ps pulses. Further reduction in pulse width may require higher modulation frequency as well as dispersion control.

8.3.5 Confirmation of true mode-locked operation

To confirm true mode-locked operation, we performed external single-pass

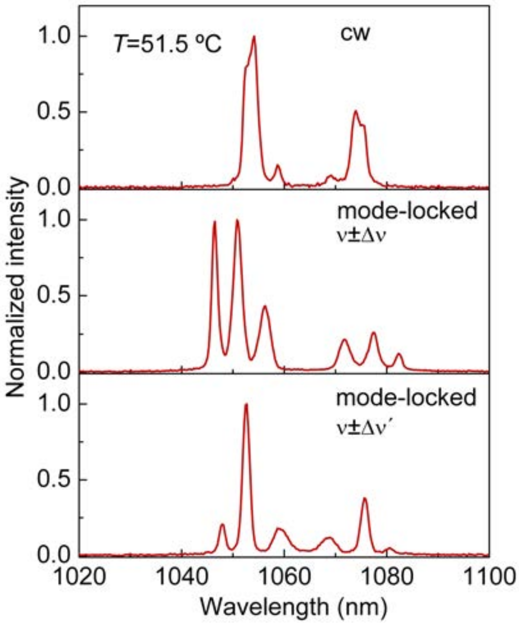

Figure 8.8: Spectrum of the cw, and mode-locked signal corresponding to 160 MHz ($\nu \pm \Delta\nu$) and 80 MHz ($\nu \pm \Delta\nu'$) pulses, extracted from the DRO near degeneracy at T=51.5 ^{o}C.

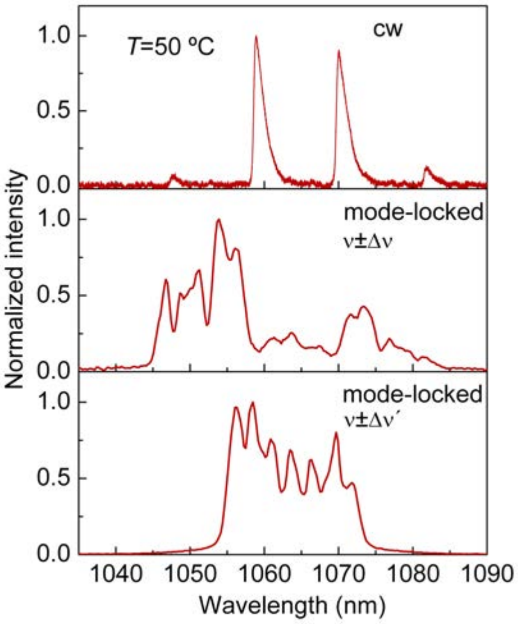

Figure 8.9: Spectrum of the cw, and mode-locked signal corresponding to 160 MHz ($\nu \pm \Delta\nu$) and 80 MHz ($\nu \pm \Delta\nu'$) pulses, extracted from the DRO at T=50 ^{o}C.

second-harmonic-generation (SHG) of DRO output in a 10-mm-long β-BaB$_2$O$_4$ (BBO) crystal cut at θ=26^o, ϕ=0^o. Using a GaAsP photodetector, we recorded the SHG output for cw and mode-locked operation corresponding to 160 MHz and 80 MHz repetition rate pulses. For a fixed average input power to the BBO crystal, we recorded ~4 times enhancement in the measured SHG output under mode-locked operation at both 160 MHz and 80 MHz compared to cw operation, indicating the real achievement of energy concentration resulting from mode-locked operation. The results are shown in Fig. 8.10(a) and 8.10(b). However, the lower than theoretically predicted SHG enhancement could be attributed to the limited wavelength acceptance bandwidth of the 10-mm-long BBO crystal compared to the spectral width of the OPO output.

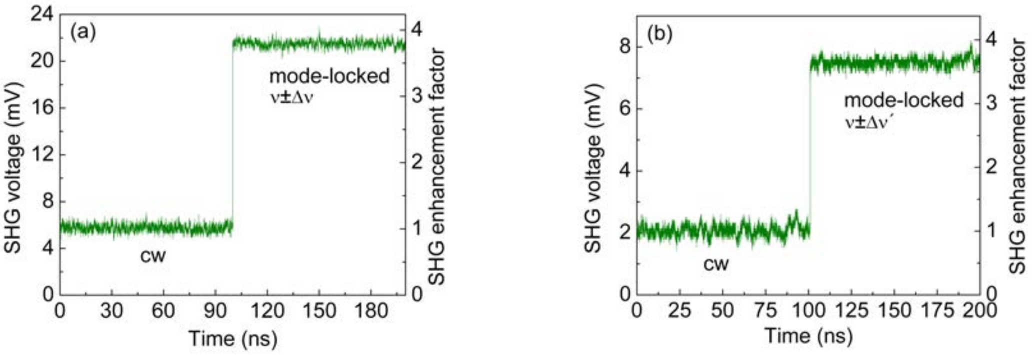

Figure 8.10: Enhancement of the SHG output for mode-locked operation with respect to cw operation, detected using a photodetector for (a) 160 MHz pulses ($\nu \pm \Delta\nu$) and (b) 80 MHz pulses ($\nu \pm \Delta\nu'$).

8.4 Phase-modulation-mode-locked cw DRO

8.4.1 Experimental setup

The schematic of the experimental setup is shown in Fig. 8.11. The fundamental pump source used is similar to that described in section 8.3.1. To maintain stable output characteristics of the laser, we operated the pump laser at maximum power and used a combination of a HWP and a PBS cube as power attenuator. A second HWP is used to adjust the pump polarization for phase-matching in the nonlinear crystal. The nonlinear crystal used is identical to that described in section 8.3.1. The crystal is housed in an oven, with a stability of ±0.1^{o}C, which can be tuned from room temperature to 200 ^{o}C. Using a lens of focal length f=150 mm, the pump beam is focused to waist radius w_p=31 μm corresponding to a confocal focusing parameter of $\xi\sim$1.2, with signal/idler beam waist radius of $w_{s/i}$=46 μm at the center of the nonlinear crystal, resulting into optimum mode matching. The cw DRO is configured in a standing-wave cavity comprising of two concave mirrors M_1 and M_2 (r=100 mm), one plane mirror M_3, one concave mirror M_4 (r=1000 mm), and one OC, M_5. Mirrors M_1 and M_2 are highly reflecting (R>99%) for signal and idler at 1000-1090 nm and transmitting (T>93%) at 532 nm, while mirrors M_3 and M_4 are highly reflecting at 1000-1233 nm (R>99.9%) and 1000-1165 nm (R>99.7%) wavelength range, respectively. The OC has a reflectivity of $R\sim$96.5% at 1064 nm. Thus, the reflectivity of the mirrors ensures doubly-resonant oscillation near degeneracy. The output of the DRO is extracted through the OC. The EOM, described in section 8.2, is introduced inside the cavity close to the OC. The distance between the EOM end face and OC is z_0=1 cm. The beam diameter through the EOM can be adjusted using mirror M_4. Mirror, M_3 has been mounted over a translation stage, so as to adjust the cavity length to synchronize with the modulator resonant frequency. The total optical length of the DRO, when synchronized with resonant frequency of the phase modulator, is $L=2L_{linear}$=3.7 m.

8.4.2 Output power and threshold

With the crystal temperature (T) kept at 51.5 ^{o}C, the DRO without EOM provides an output power of 526 mW for 9.7 W of pump power and has an oscillation threshold of 1.1 W. However, with the insertion of the EOM, the

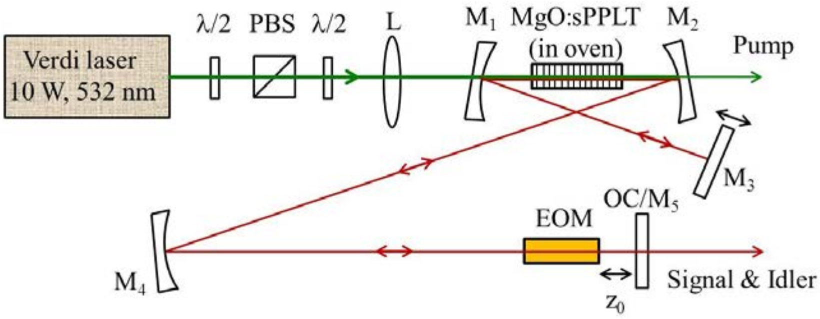

Figure 8.11: Schematic of the experimental setup. $\lambda/2$: Half-wave plate, PBS: Polarizing beam-splitter, L: Lens, M: Cavity mirrors, OC: Output coupler; EOM: Electro-optic phase modulator.

oscillation threshold increases to 1.9 W and the cw DRO provides 484 mW of output power for a pump power of 9.7 W. The increase in threshold power is attributed to the EOM insertion loss. It is to be noted that the oscillation threshold power for DRO in standing-wave configuration having shorter cavity length, comprising of three high reflecting mirrors and one OC is 700 mW. The increase in threshold pump power from 700 mW to 1.1 W is attributed to the additional cavity mirror. At T=51.5 ^{o}C the generated signal and idler wavelengths are λ_{signal}=1049 nm and λ_{idler}=1079 nm, respectively. At these wavelengths, the parametric gain curve of the nonlinear crystal is calculated to have a FWHM bandwidth of 3 THz.

8.4.3 Mode-locked pulse generation

When the EOM is switched ON, with modulation depth of 1.83 rads and frequency, ν exactly matching with the cavity length, some perturbation is seen in the output in time domain, but no mode-locked pulses are observed. However, when the modulation frequency is slightly detuned by $\Delta\nu$, on either side of ν, 471 ps pulses at 160 MHz repetition rate are observed. Figure 8.12(a) shows the temporal output from DRO, at modulation frequency of $\nu \pm \Delta\nu$, depicting the effect of change in modulation depth. As evident, in (i) at minimum modulation, some perturbation is seen, but with increase in modulation depth to 1.63 rads in (ii), 871 ps pulses at 160 MHz are observed, which then shortens to 471 ps at 1.83 rads of modulation depth in (iii). With further increase in modulation depth to 1.99 rads in (iv), alternatively equal amplitude pulses at 160 MHz are observed with high intensity pulses at 473 ps duration and low intensity pulses at 437 ps duration. In (v), with the modulation frequency kept fixed at $\nu \pm \Delta\nu$, if we further increase the modulation depth to maximum at 2.4 rads, 533 ps pulses at 80 MHz are observed. Pulses at 80 MHz with 533 ps duration are also observed, as shown in Fig. 8.12(b), when the modulation depth is kept fixed at μ_3=1.83 rads and modulation frequency is detuned by $\Delta\nu'$, on either side of ν, where $\Delta\nu' > \Delta\nu$. The values for $\Delta\nu'$ and $\Delta\nu$ and difference between them, are of the order of kHz. Hence, to obtain stable short pulses at 80 MHz, a careful adjustment of the modulation frequency or precise change in cavity length over a narrow zone at moderate value of modulation depth is required. The use of a piezoelectric transducer (PZT)-driven self-tuning mirror as one of the cavity mirror could be very helpful, not only to fine tune the cavity length to achieve the required repetition rate, but also to actively stabilize the cavity length, thus reducing the possibility of any arbitrary switching of the repetition rate between 80 MHz and 160 MHz, if that may occur. The inset of Fig. 8.12(b) shows the zoomed version of the stable pulses with 533 ps duration at 80 MHz repetition rate obtained at modulation depth of 1.83 rads and modulation frequency of $\nu \pm \Delta\nu'$. Unlike the earlier report with cw pumping [60], we have not observed any cw background in the output pulse intensity.

Depending upon the temporal characteristics, the region of operation of the DRO can be divided into two. The two regions can be shown to represent a series of pulses with one having a repetition rate equal to the modulation frequency and other at twice that of modulation frequency. As also observed earlier in the context of lasers [129], here when the train of pulses at 160 MHz

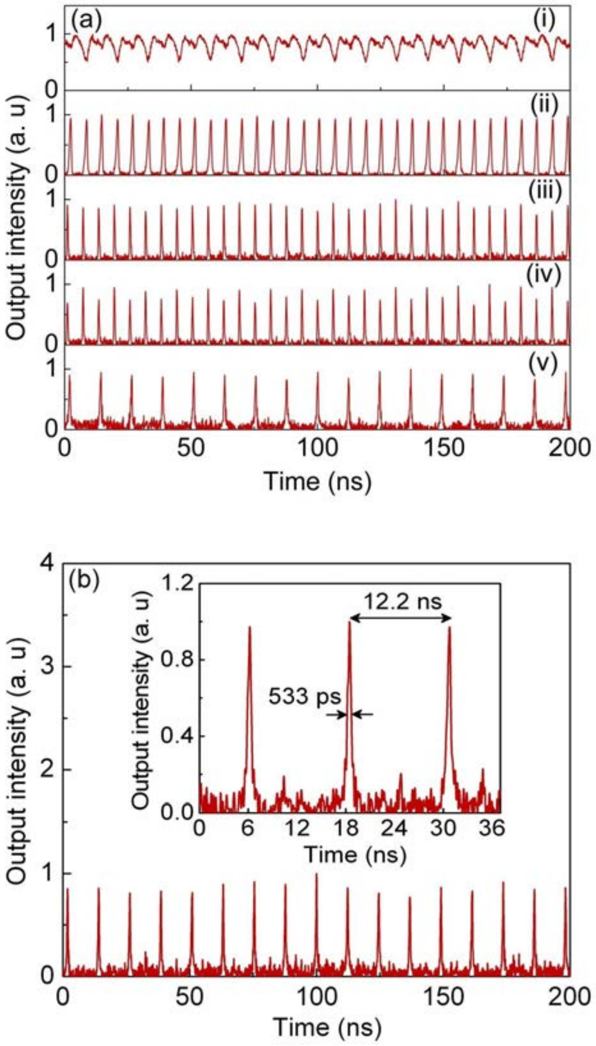

Figure 8.12: (a) Pulse train obtained at modulation frequency of $\nu \pm \Delta\nu$, and for modulation depths of (i) μ_1 (ii) μ_2 (iii) μ_3 (iv) μ_4 and (v) μ_5. (b) Pulse train obtained at modulation frequency of $\nu \pm \Delta\nu'$ and for modulation depth of μ_3. Inset: Zoomed 533 ps pulses at 80 MHz.

is compared with the sinusoidal modulation signal, the optical phase difference between the pulses is found to be π. This shows two pulses travelling back and forth inside the cavity, with one pulse delayed in time by L_{linear}/c with respect to the other. Thus, it represents two oscillating states of mode-locked pulses. For 80 MHz pulses obtained, the pulses pass through the modulator either at the peak or minima of the modulation signal. The two mode-locked states are clearly visible at modulation frequency of $\nu \pm \Delta\nu$ and depth of μ_3=1.99 rads, as seen in (iv) of Fig. 8.12(a), where alternatively equal pulses are observed with one state having higher intensity than the other. The two oscillating states with unequal amplitude are also observed when the modulation depth and frequency are kept fixed at 1.83 rads and $\nu \pm \Delta\nu$, respectively, while slightly detuning the cavity length.

8.4.4 Power stability

We recorded the average passive power stability at mode-locked condition for 160 MHz repetition rate pulses at maximum pump power for modulation depth of 1.83 rads and frequency at $\nu \pm \Delta\nu$. As evident from Fig. 8.13, an average passive power stability better than 3.5% rms over 15 minutes has been observed. The fluctuation in the average power is attributed to the mechanical vibrations, air currents, and temperature variations, as the measurements were taken in open laboratory environment and under free running condition of the DRO. The corresponding pulse train recorded in the microsecond scale, depicting the intensity noise on the output pulses, is shown in the inset of Fig. 8.13, where a pulse peak-to-peak stability better than 19% is measured over 20 μs. The pulse width measured at end of 20 μs is the same as in the beginning, showing steady state pulse durations over microsecond time scale.

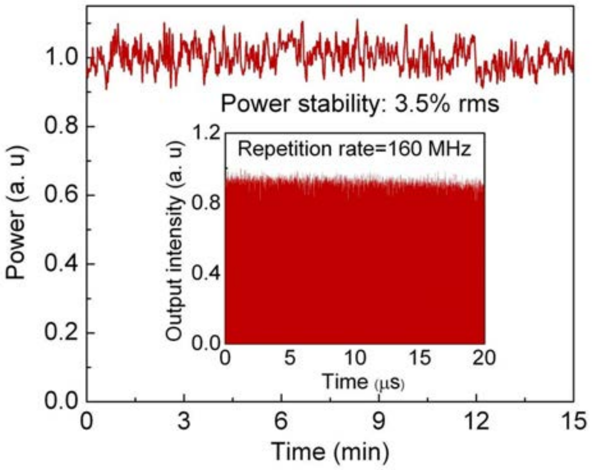

Figure 8.13: Time trace of the mode-locked output at 160 MHz over 15 minutes. Inset: Mode-locked output pulse train at 160 MHz over 20 μs.

8.4.5 Pulse width dependence on the position of EOM

In order to study the dependence of the pulse width on the position of the EOM inside the cavity, we increased the distance of the EOM from OC to z_0=6 cm, and observed the output from DRO in time domain for different modulation conditions. The behavior of the output from the DRO is similar as compared to when EOM is placed very close to OC (z_0=1 cm), except the difference in the pulse width. Figure 8.14 shows the pulses obtained at modulation depth of 1.83 rads and modulation frequency at $\nu \pm \Delta\nu$ for z_0=6 cm, and the inset of Fig. 8.14 shows the comparison for (i) z_0=6 cm and (ii) z_0=1 cm with the zoomed version of the pulses. As observed, the pulse duration for z_0=6 cm is 953 ps, which is larger than the pulse duration obtained for z_0=1 cm. As also shown earlier in the context of lasers, the modulation coupling has direct dependence on the location of the modulation element inside the cavity [129]. When the EOM is very close to the cavity mirror, z_0~0, the coefficient in the coupled equation [129] is maximized, showing increase in locking of the modes.

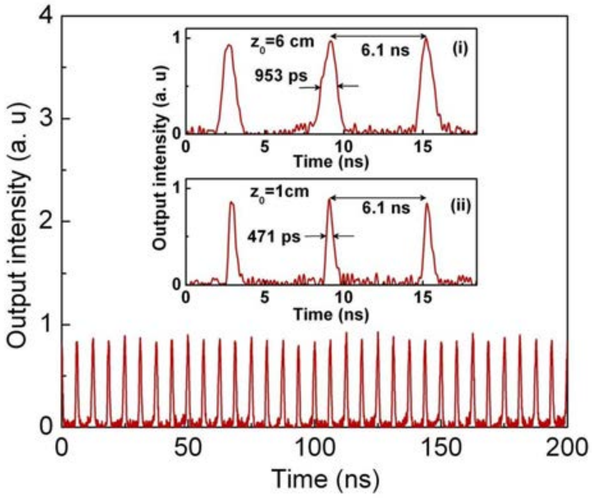

Figure 8.14: Pulse train at 160 MHz for z_0=6 cm. Inset: Zoomed 953 ps and 471 ps pulses for (i) z_0=6 cm and (ii) z_0=1 cm, respectively.

8.4.6 Pulse width dependence on pumping level

We also looked into the duration of pulses for different input pump power keeping z_0=6 cm. We have observed very less significant change in pulse duration with the change in the pumping level. For example, we measured a decrease in pulse duration from 953 ps to 848 ps at 160 MHz for a decrease in pump power from 9.7 W to 6.8 W, accompanied with the decrease in the pulse amplitude. The OPO stops working with further decrease in pump power to 3.4 W.

8.4.7 Output spectrum

We further looked into the spectral domain under cw and mode-locked condition using spectrometer (HR4000 oceanoptics). Figure 8.15(a) shows the output spectrum of the DRO under cw operation. Under cw condition the modes are oscillating independently, with an observed spectral bandwidth of 11 nm and 10 nm for signal and idler, respectively. However, when the modulation depth is increased to 1.83 rads and frequency tuned to $\nu \pm \Delta\nu$, a spectrum with almost the same bandwidth as in cw has been observed for signal and idler, but with an envelope, as seen in Fig. 8.15(b). The lower intensity of idler is due to the low reflectivity value of cavity concave mirrors for idler wavelength.

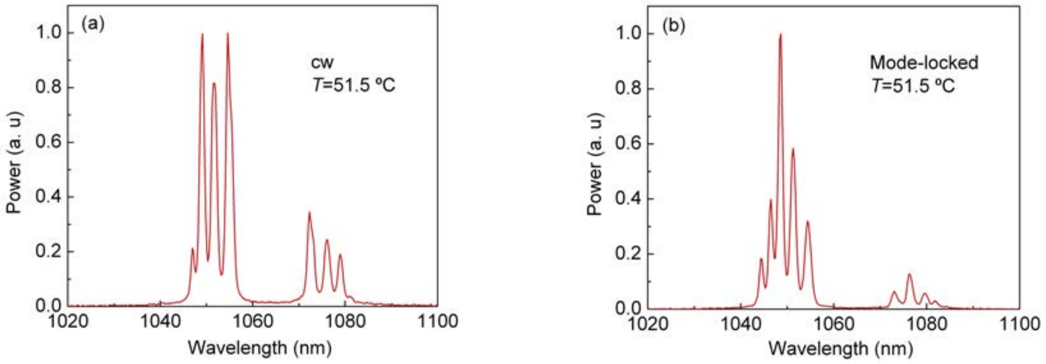

Figure 8.15: Spectrum of the output extracted from the DRO at T=51.5 ^{o}C, under (a) cw operation, and (b) mode-locked operation at modulation frequency of $\nu \pm \Delta\nu$ and depth of μ_3=1.83 rads.

If we decrease the crystal temperature to T=50 ^{o}C, keeping modulation frequency at $\nu \pm \Delta\nu$ and depth at μ=1.83 rads, at degeneracy the signal and idler branches meet together resulting in a spectrum spanning over 31 nm, as seen in Fig 8.16(a). When the modulation frequency is detuned to ν, the spectrum broadens to its maximum, with an observed increase in average power. The result is shown in Fig. 8.16(b), where a spectrum spanning over 52 nm is measured at T=50 ^{o}C. The corresponding measurement in time domain showed only some perturbation with no mode-locking, however at modulation frequency of $\nu \pm \Delta\nu$, pulses are observed with the same duration as at T=51.5 ^{o}C.

Assuming Gaussian pulse shape and a time-bandwidth product of 0.44, the transform limited pulse duration for 31 nm bandwidth spectrum has been calculated to be ~53 fs. Also, considering the internal phase modulation that result in to a linear frequency shift, as discussed in earlier reports [61], leading to a time-bandwidth product of 0.626, the pulse duration has been calculated

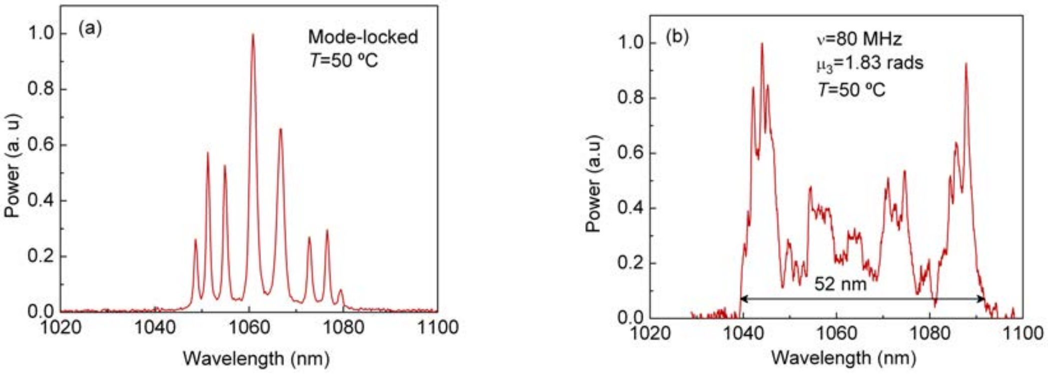

Figure 8.16: Spectrum of the output extracted from the DRO at T=50 ^{o}C, for modulation depth of μ_3=1.83 rads, and at modulation frequencies of (a) $\nu \pm \Delta\nu$ and (b) ν=80 MHz.

to be ∼75 fs. The discrepancy between the experimental pulse duration and the transform limited pulse duration could be due to the lower modulation frequency of the EOM, which results into less efficient mode-locking as all of the modes in the spectrum does not get locked in phase. The longer pulse duration obtained could also be due to the intracavity dispersion which comes into effect because of the longer nonlinear crystal and longer electro-optic crystal used. Further shorter pulses could be attained using modulator with high speed modulation and also by using nonlinear crystals with shorter interaction length, as the DROs are not affected much with lower gain, subject to the low oscillation threshold power. Use of dispersive or chirp mirrors could also be useful.

8.4.8 Confirmation of true mode-locked operation

For confirming the mode-locked operation, we performed the external single-pass SHG of the DRO output at different operating conditions. The nonlinear crystal used is 10-mm-long BBO cut at θ=26^o, ϕ=0^o. Using a lens of focal length, f=75 mm, the output for cw, 160 MHz and 80 MHz pulses was focused consecutively at the centre of the crystal, and the frequency-doubled power was measured using the GaAsP photodetector. We have observed ∼4 times enhancement of the SHG power in mode-locked operation both for 80 and

160 MHz pulses, as compared to that in the cw operation, for a fixed average fundamental power in both conditions. The SHG enhancement factor of ∼4 times is lower than that of the theoretically calculated value of 23 times, for 533 ps pulses at 80 MHz. As we have not observed any cw background with the mode-locked pulses, we believe that the cw background has negligible effect on the measured SHG enhancement factor. However, the low SHG enhancement could be attributed to various factors including narrow acceptance bandwidth of BBO, as also discussed in section 8.3.5.

8.5 Phase-modulation-mode-locked cw SRO

8.5.1 Experimental setup

The experimental configuration of the mode-locked cw SRO, as shown in Fig. 8.17, is identical to that of the mode-locked cw DRO described in section 8.4.1, except the cavity mirrors used here. Here, mirrors, M_1 and M_2, are highly reflecting for the idler (R>99.9% over 1064–1292 nm) and transmitting for the signal (T>75%–90% over 800–1000 nm) and pump (T>86% at 532 nm). Mirror, M_3 is highly reflecting for the idler (R>99.9% over 1064–1245 nm). Mirror, M_4 is reflective for the idler (R>99.7%) only across the 1064–1155 nm wavelength range, while M_5 is highly reflecting for the idler (R>99.9%) over 1064–1245 nm. Thus, the mirrors reflectivity ensures idler-only resonant configuration. The nonlinear crystal used is identical to that described in section 8.3.1. The crystal is housed in an oven with a stability of ±0.1 ^{o}C, enabling the temperature to be varied from 25 ^{o}C to 200 ^{o}C. Using a lens of focal length, f=150 mm, the pump beam is focused to waist radius of w_p=31 μm, corresponding to a confocal focusing parameter of $\xi\sim1.2$. The SRO cavity provides an idler beam waist of w_i=46 μm, resulting in optimum mode matching ($b_p\sim b_i$) at the center of the crystal. We use the idler-resonant design for the SRO to minimize intracavity losses due to the AR-coating range

(1–1.6 μm) of the EOM deployed for mode-locking. The EOM, described in section 8.2, is introduced inside the cavity close to the mirror, M_5. The single-pass insertion loss of the EOM is measured to be ~5% (−0.23 dB) at 1032 nm. The beam diameter through the EOM can be adjusted using mirror M_4. Mirror, M_3 is mounted on a translation stage to enable adjustment of the cavity length for synchronization with the EOM resonant frequency. The total SRO cavity length is L=3.7 m, synchronized to the EOM resonant frequency. A dichroic mirror, M, is used to separate the non-resonant signal from the transmitted pump.

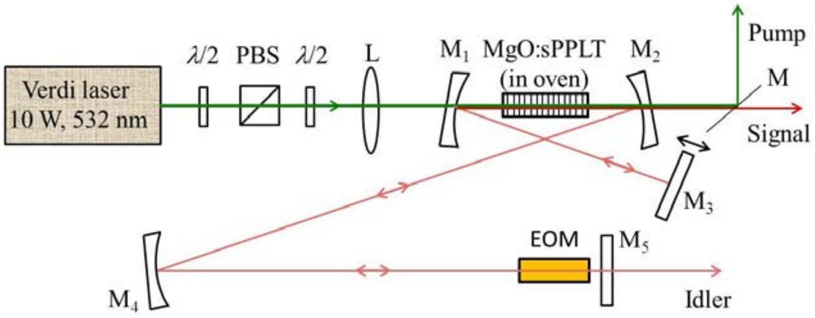

Figure 8.17: Schematic of the experimental setup. $\lambda/2$: Half-wave plate, PBS: Polarizing beam-splitter, L: Lens, M_{1-5}: Cavity mirrors, M: Dichroic mirror, EOM: Electro-optic phase modulator.

8.5.2 Mode-locked pulse generation

We investigated mode-locking of the SRO output by performing systematic change in the modulation depth of the EOM, while simultaneously studying the fine adjustment of modulation frequency and accurate change in the cavity length.

Maintaining the crystal temperature at 70 ^{o}C, corresponding to a signal wavelength of 989 nm (idler of 1151 nm), we monitored the temporal output of the SRO using the InGaAs photodetector (20 GHz, 18.5 ps) and the fast oscilloscope (3.5 GHz, 40 GS/s). At these wavelengths, the parametric gain bandwidth for the crystal is 0.6 THz. The SRO oscillation threshold power was 7.15 W and the data were collected for both the resonant idler (extracted through mirror M_5) and the non-resonant signal (extracted through M_2) at a pump power of 9.62 W.

When the EOM incorporated inside the SRO cavity is switched on, with the modulation frequency and depth kept at the minimum value, a slight sinusoidal modulation is observed in the cw SRO output in time. With the increase in modulation depth to μ'=0.18 rads, a modulated output at 80 MHz repetition frequency is observed. Figure 8.18 shows measurements for the idler output, depicting the effect of change in modulation frequency and depth, keeping either of the parameters fixed. In (i), with the modulation depth fixed at μ'=0.18 rads, increasing the modulation frequency from minimum to ν_1 results in the generation of 720 ps pulses at 160 MHz. Then, in (ii), by increasing the modulation frequency to 80 MHz (ν) short pulses of 230 ps duration at 80 MHz repetition rate are generated. With further increase in modulation frequency from 80 MHz to ν_2, in (iii), the pulse repetition rate again changes to 160 MHz. The change in modulation frequency ($\Delta\nu = \nu - \nu_1$ or $\nu_2 - \nu$) is very small, of the order of kHz, and corresponds to very narrow zone for change in the cavity length. The use of a PZT-driven self-tuning mirror could be helpful for sensitive control of the cavity length. Thus, to obtain stable short pulses at 80 MHz, perfect synchronization of the cavity length (free spectral range, FSR=c/L) with the EOM resonant frequency or careful adjustment of the modulation frequency is required. At marginally lower and higher modulation frequencies than ν_1 and ν_2, respectively, broader pulses at 160 MHz are generated. On the other hand, by keeping the modulation frequency fixed at ν (80 MHz) and reducing modulation depth from μ'=0.18 rads to a lower value (μ''), we observe 620 ps pulses at 160 MHz, as seen in (iv). Further decrease in modulation depth to μ''' results in broadening of the pulses to 1.4 ns, as seen in (v).

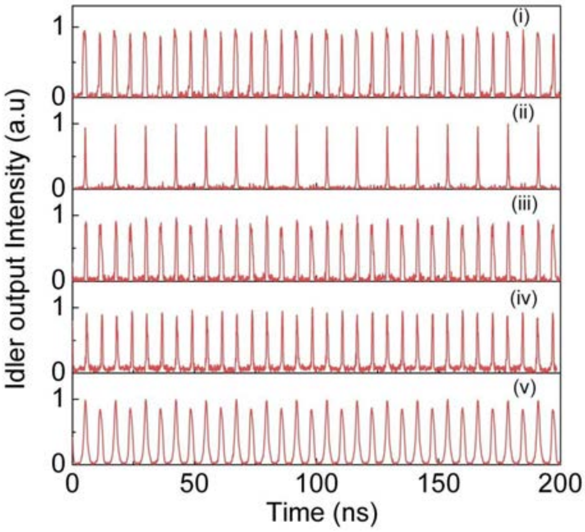

Figure 8.18: Idler output pulse train obtained at modulation frequency ($\nu_1<\nu<\nu_2$) and modulation depth ($\mu'>\mu''>\mu'''$) of (i) ν_1, μ'; (ii) ν, μ'; (iii) ν_2, μ'; (iv) ν, μ''; (v) ν, μ'''.

Figure 8.19 shows the applied sinusoidal modulation (at μ'=0.18 rads) together with resonant idler pulses obtained at the exact modulation frequency of 80 MHz (ν), and at slight detuning (ν_1, ν_2). As evident, for 80 MHz pulses (obtained at ν), the pulses appears at alternating values of 0 and 2π. Thus, the optical phase difference between the pulses is 2π. However, for 160 MHz pulses (obtained at ν_1, ν_2), the phase difference is observed to be π. This indicates that a slight detuning of modulation frequency from synchronization can lead to pulses with twice the repetition rate. At the modulation frequency of 80 MHz (ν), a single phase-locked state oscillates inside the cavity, but as the modulation frequency is increased or decreased by $\Delta\nu$, double pulsing occurs with two mode-locked states oscillating together. Similar behavior was also observed for the non-resonant signal wave.

Figures 8.20(a) and 8.20(b) show the output signal pulses at modulation depth of μ'=0.18 rads with repetition frequency of 160 and 80 MHz obtained at modulation frequency of ν_1 and ν, respectively. As seen, pulses as short as 737 ps at 160 MHz and 288 ps at 80 MHz were recorded, exhibiting a similar

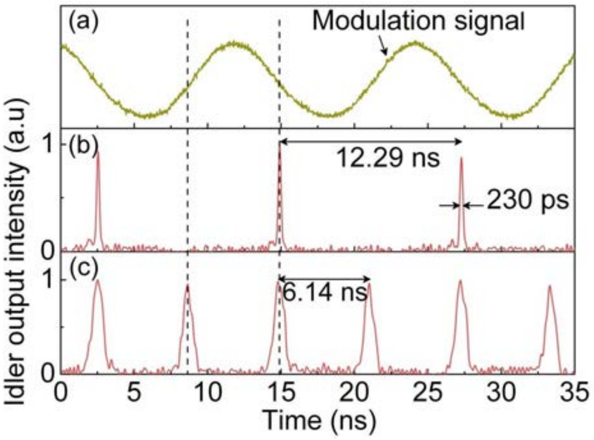

Figure 8.19: (a) Applied modulation, (b) 80 MHz, and (c) 160 MHz repetition rate idler pulses at μ'=0.18 rads.

behavior to the idler pulses. Also, as evident, there is no cw background present in the idler or signal pulse intensity.

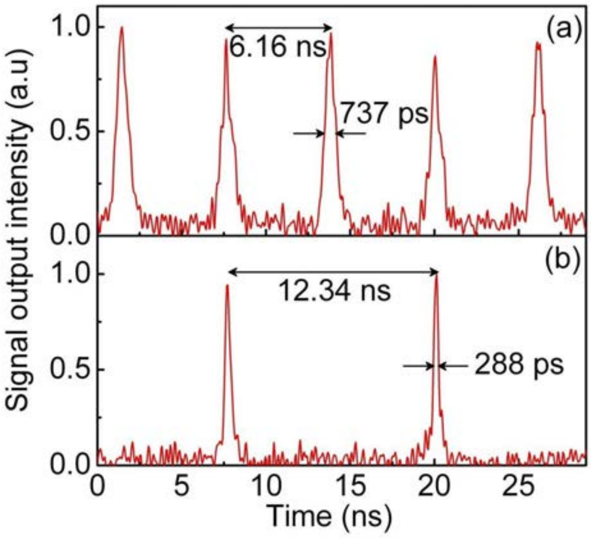

Figure 8.20: Signal pulses at (a) 160 MHz and (b) 80 MHz.

As compared to the pulse width obtained, in section 8.4.3 from mode-locked cw DRO, we observed shorter pulses in SRO configuration. We believe that the difference in the pulse duration could be due to the phase modulator used in the experiment, which are specified for narrowband or single-frequency operation.

As we have seen in section 8.4.6, and also there are earlier reports [47] showing effect of pump power on pulse duration, the difference in the pulse duration could also be due to the higher pumping level (5 times above threshold) in the DRO as compared to that in the SRO.

8.5.3 Output spectrum

Using a FPI (FSR=1 GHz, finesse=400), we measured the spectrum of the mode-locked signal output. As shown in Fig. 8.21, under mode-locked condition (μ' =0.18 rads; ν_1) we found the spectrum to extend across Δf~0.619 GHz. The corresponding transform-limited pulse duration is calculated to be $\Delta\tau$~710 ps, assuming Gaussian pulse shape and a time-bandwidth product of $\Delta\tau \cdot \Delta f$=0.44. However, it has been shown that internal phase modulation results in a linear frequency shift, which leads to a timebandwidth product of 0.626 [61]. Considering the frequency chirp and low FSR of our FPI, we believe the spectrum to be broader than what we observe. In mode-locked operation at 80 MHz repetition rate, the signal spectral bandwidth could not be determined, as the measurement was limited by the diagnostics.

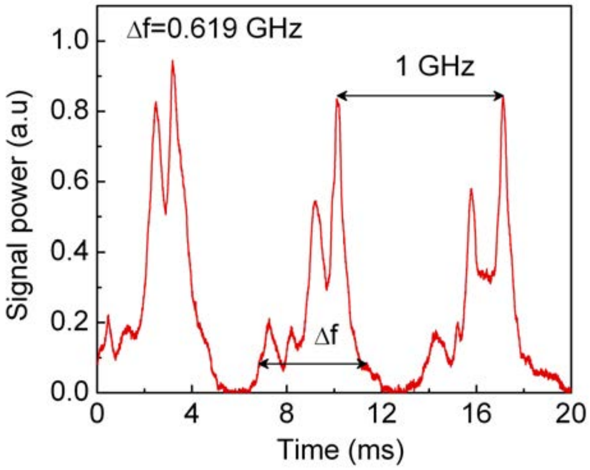

Figure 8.21: Spectrum of the mode-locked signal at 160 MHz.

8.5.4 Pulse stability, and confirmation of true mode-locked operation

We also determined the stability of the mode-locked output pulse train by recording the intensity noise on the signal pulses at 80 MHz. The result is shown in Fig. 8.22, where a pulse peak-to-peak stability better than 15% is measured over 500 μs.

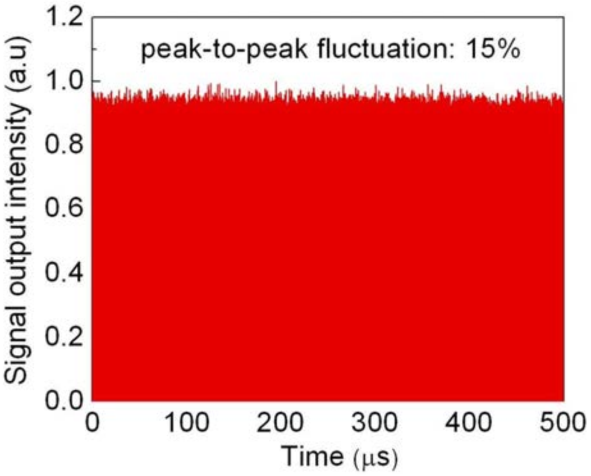

Figure 8.22: Signal pulse train at 80 MHz over 500 μs.

Further, in order to confirm true mode-locked operation of the SRO, we performed external single-pass SHG in 10-mm-long BBO crystal cut at θ=26^o, ϕ=0^o and AR-coated for 425–500 nm and 850–1000 nm. The output signal was focused at the center of the crystal in both mode-locked and cw operation using same lens of focal length, f=75 mm, and the frequency-doubled output in the blue was recorded using the GaAsP photodetector. Using this setup, we observed a ∼4 times enhancement of SHG power in mode-locked operation compared to that in cw operation, for the same average fundamental power in both conditions.

8.6 Conclusions

In conclusion, we have demonstrated, what we believe for the first time, the generation of picosecond pulses from cw OPOs using novel techniques based on phase modulation assisted amplitude modulation, and also by pure phase modulation.

By deploying an electro-optic phase modulator and an ARR interferometer internal to a near-degenerate cw DRO based on MgO:sPPLT, we generated 730 ps pulses at 160 MHz and 450 ps pulses at 80 MHz. Spectral broadening spanning ∼34 nm has also been observed. We have also demonstrated the generation of picosecond pulses from a cw DRO based on MgO:sPPLT by active mode-locking of the DRO using an electro-optic phase modulator as the single mode-locking element. Mode-locked pulses at 80 MHz and 160 MHz with 533 ps and 471 ps pulse duration at modulation depth of 1.83 rads and modulation frequency at $\nu \pm \Delta\nu'$ and $\nu \pm \Delta\nu$, respectively, have been generated. Mode-locked pulses for different operating regions of the DRO, obtained with the change in modulation depth and frequency detuning have been explored. It has also been observed that like in lasers, in OPO cavity the position of the modulator is an important factor for obtaining shorter pulses. The average passive power stability of the DRO output for 160 MHz has been measured to be better than 3.5% rms over 15 minutes. Under moderate modulation depth and at exact resonant frequency modulation, spectrum spanning over 52 nm has been observed at degeneracy. The mode-locked operation has been further confirmed by observing ∼4 times enhancement in SHG power under mode-locked condition, as compared to cw operation.

Further, we have demonstrated successful mode-locking of a cw SRO using direct electro-optic phase modulation, providing output pulses as short as 230 ps at 80 MHz repetition rate. Mode-locked pulses obtained for different operating regions of the SRO have been explored.

By using an EOM with increased modulation frequency and by deploying intracavity dispersion compensation, further reductions in pulse duration could be attainable. The extension of the approach to passive mode-locking techniques, including Kerr-lens mode-locking, will pave the way for the realization of a new generation of ultrafast sources with broad and arbitrary tuning in different spectral regions based on OPOs pumped by widely available cw lasers.

Chapter 9

Summary and outlook

In this thesis, we have demonstrated the development of optical parametric oscillators (OPOs), and nonlinear frequency conversion sources, under continuous-wave (cw) pumping, spanning the ultraviolet (UV) to mid-infrared (IR) spectral regions. Different architectures, designs, experimental configurations and nonlinear crystals have been deployed and investigated, for the first time.

The main outcomes of the work include:

- Demonstration of an efficient fiber-laser-based source of high-power, cw, linearly-polarized radiation at 970 nm in a simple, compact, and practical design. Using direct single-pass second-harmonic-generation (SP-SHG), 13.1 W of output power at 970 nm has been generated for a fundamental power of 40 W at a conversion efficiency as high as 32.7%. The generated second-harmonic output exhibits a passive power stability better than 1.4% (1σ value) over 1 hour, has a linewidth better than 0.3 nm, and a TEM_{00} spatial beam profile with M^2<1.6. Relevant theoretical calculations for the characterization of SP-SHG in the crystal have also been performed.
- Successful deployment of an antiresonant ring (ARR) interferometer for

the attainment of optimum output coupling in a Yb-fiber-laser-pumped cw OPO. The cw OPO, configured as a singly-resonant oscillator (SRO), was based on MgO:PPLN. By fine adjustment of the ARR transmission, a continuously variable signal output coupling from 0.8% to 7.3% has been achieved, providing optimum output coupling for signal and optimum power extraction for the idler, at different input pumping levels. The experimental results were further compared with theoretical calculations for conventional output-coupled cw SRO.

- Demonstration of a high-power, single-frequency, cw source tunable across 775-807 nm in the near-infrared, based on internal second-harmonic-generation (SHG) of a cw SRO pumped by a Yb-fiber laser. The compact, all-periodically-poled source provides as much as 3.7 W of near-infrared power at 793 nm, together with 4 W of idler power at 3232 nm, at an overall extraction efficiency of 28%. Further, the cw OPO is tunable across 3125-3396 nm in the idler, providing as much as 4.3 W at 3133 nm with >3.8 W over 77% of the tuning range together with >3 W of near-infrared power across 56% of SHG tuning range, in high spatial beam quality with M^2<1.4. The SHG output has an instantaneous linewidth of 8.5 MHz and exhibits a passive power stability better than 3.5% rms over more than one minute.
- Generation of stable, cw UV radiation in single-pass configuration based on sum-frequency-mixing of 1064 nm and 532 nm radiation, in BiB_3O_6. The 532 nm radiation was generated by single-pass SHG of Yb-fiber laser in MgO:sPPLT. The single-pass cw UV source provides as much as 68 mW of single-frequency UV power with a passive power stability better than 3.2% rms over 2 hours and frequency stability better than 437 MHz over >2.5 hours, in elliptic beam profile with ${M_x}^2$<1.6 and ${M_y}^2$<1.8, indicating a TEM_{00} spatial mode.
- A novel architecture comprising two cw OPOs coupled together with an

ARR interferometer, generating two pairs of signal and idler wavelengths. The OPOs, based on identical MgO:sPPLT crystals, were pumped by a single cw laser at 532 nm. The two pairs of signal and idler wavelengths can be independently and arbitrarily tuned to indefinitely close spacing, through degeneracy, and beyond, across the wavelength range of 870-1370 nm. Frequency separation from 7 THz down to 0.8 THz has been demonstrated, and their overlap at 951 nm shown, providing a frequency difference of ∼220 MHz. The OPOs simultaneously generated idler powers of >1 W.

- Generation of record shortest picosecond pulses by active mode-locking of cw OPOs in doubly- and singly-resonant configuration using direct low-frequency electro-optic phase-modulation (EOM). Also, a technique based on the deployment of the EOM in combination with an ARR interferometer internal to the cw OPO has been investigated. The mode-locking of cw SRO has resulted in a stable train of 230 ps pulses at 80 MHz.

As a direction for the future work, the performance of the OPOs in terms of power stability can further be improved by better temperature control, isolation from mechanical vibrations, and active stabilization of cavity length. The theoretical study of the output-coupled SRO shows that by reducing the insertion loss of the ARR elements, the performance of the ARR output-coupled cw SRO can be further enhanced. The demonstrated SHG tuning in the near-infrared can be further extended to cover almost the entire Ti:sapphire wavelength range using different grating periods of the employed MgO:PPLN crystal and simultaneously varying the grating of the MgO:sPPLT crystal. In the ARR-coupled OPO, the high intracavity power of the two closely spaced, unidirectional signal waves can be used for efficient generation of widely tunable terahertz radiation. New nonlinear materials for cw terahertz generation can be explored.

Future possible developments of this work include:

- Development of Tm-fiber-laser-pumped cw OPOs tunable in the spectral region beyond 4 μm, based on MgO:PPLN and OP-GaAs
- The deployment of intracavity sum-frequency-mixing scheme in green-laser-pumped cw OPO, resulting in the generation of tunable UV radiation.
- Active mode-locking of cw OPO using an EOM with increased modulation frequency, and various crystal lengths.

Investigations in these directions are already ongoing.

Bibliography

[1] T. H. Maiman, Stimulated optical emission in ruby, Nature 187, 493-494 (1960).

[2] M. Ebrahim-Zadeh and I. T. Sorokina, Mid-Infrared coherent sources and applications, 1st ed. (Springer, 2007).

[3] C. L. Tang and L.K. Cheng, Fundamentals of optical parametric processes and oscillators in Laser science and technology series,Vol-10, Harwood academic publishers (1995).

[4] J. A. Armstrong, N. Bloembergen, J. Ducuing, and P. S. Pershan, Interaction between light waves in a nonlinear dielectric, Phys. Rev. 127, 1918-1939 (1962).

[5] M. Ebrahim-Zadeh, Continuous wave optical parametric oscillators, Handbook of optics, 3rd ed. (Optical Society of America, Washington, D.C.), Vol. 4, Chapter. 17 (2010).

[6] R. C. Gray, The Rev. John Kerr, F.R.S., Inventor of the Kerr Cell, Nature 136, 245-247 (1935).

[7] C. V. Raman and K. S. Krishnan, A new type of secondary radiation, Nature 121, 501-502 (1928).

[8] E. Schrodinger, Nonlinear optics, Proc. Royal Irish Academy 47 A, 77-117 (1942).

[9] E. Schrodinger, A new exact solution in non-linear optics, Proc. Royal Irish Academy 49 A, 59-66 (1943).

[10] P. A. Franken, A. E. Hill, C. W. Peters, and G. Weinreich, Generation of optical harmonics, Phys. Rev. Lett. 7, 118-119 (1961).

[11] M. Bass, P. A. Franken, A. E. Hill, C. W. Peters, and G. Weinreich, Optical mixing, Phys. Rev. Lett. 8, 18-18 (1962).

[12] J. A. Giodmaine, Mixing of light beams in crystals, Phys. Rev. Lett. 8, 19-20 (1962).

[13] A. W. Smith and N. Braslau, Observation of an optical difference frequency, J. Appl. Phys. 34, 2105-2106 (1963).

[14] R. H. Kingston, Parametric amplification and oscillation at optical frequencies, Proc. IRE 50, 472–473 (1962).

[15] N. M. Kroll, Parametric amplification in spatially extended media and application to the design of tuneable oscillators at optical frequencies, Phys. Rev. 127, 1207–1211 (1962).

[16] S. A. Akhmanov and R. V. Khokhlov, Concerning one possibility of amplification of light waves, Sov. Phys. J. Exp. Theor. Phys. 16, 252–254 (1963).

[17] C. C. Wang and G. W. Racette, Measurement of parametric gain accompanying optical difference frequency generation, Appl. Phys. Lett. 6, 169-171 (1965).

[18] J. A. Giordmaine and R. C. Miller, Tunable coherent parametric oscillation in $LiNbO_3$ at optical frequencies, Phys. Rev. Lett. 14, 973-976 (1965).

[19] R. G. Smith, J. E. Geusic, H. J. Levinstein, S. Singh, and L. G. Van Uitert, Low-threshold optical parametric oscillator using $Ba_2NaNb_5O_{15}$, J. Appl. Phys. 39, 4030-4032 (1968).

[20] R. L. Byer, M. K. Oshman, J. F. Young, and S. E. Harris, Visible cw parametric oscillator, Appl. Phys. Lett. 13, 109-111 (1968).

[21] Y. X. Fan, R. C. Eckardt, R. L. Byer, R. K. Route, and R. S. Feigelson, $AgGaS_2$ infrared parametric oscillator, Appl. Phys. Lett. 45, 313-315 (1984).

[22] M. J. Rosker and C. L. Tang, Widely tunable optical parametric oscillator using urea, J. Opt. Soc. Am. B 2, 691-696 (1985).

[23] L. K. Cheng, W. R. Bosenberg, and C. L. Tang, Broadly tunable optical parametric oscillation in β-BaB_2O_4, Appl. Phys. Lett. 53, 175-177 (1988).

[24] M. Ebrahim-Zadeh, A. J. Henderson, and M. H. Dunn, An Excimer-pumped β-BaB_2O_4 optical parametric oscillator tunable from 354 nm to 2.370 μm, IEEE J. Quantum Electron. 26, 1241-1252, (1990).

[25] D. C. Edelstein, E. S. Wachman, and C. L. Tang, Broadly tunable high repetition rate femtosecond optical parametric oscillator, Appl. Phys. Lett. 54, 1728-1730 (1989).

[26] M. Ebrahim-Zadeh, Mid-Infrared ultrafast and continuous-wave optical parametric oscillators in Solid-State Mid-Infrared Laser Sources, Springer-Verlag (2003).

[27] M. Ghotbi, A. Esteban-Martin, and M. Ebrahim-Zadeh, BiB_3O_6 femtosecond optical parametric oscillator, Opt. Lett. 31, 3128-3130 (2006).

[28] M. Ghotbi, A. Esteban-Martin, and M. Ebrahim-Zadeh, Tunable, highrepetition-rate, femtosecond pulse generation in the ultraviolet, Opt. Lett. 33, 345-347 (2008).

[29] K. Kawase, M. Sato, T. Taniuchi, and H. Ito, Coherent tunable THz-wave generation from $LiNbO_3$ with monolithic grating coupler, Appl. Phys. Lett. 68, 2483-2485 (1996).

[30] S. T. Yang, R. C. Eckardt, and R. L. Byer, Continuous-wave singly resonant optical parametric oscillator pumped by a single-frequency resonantly doubled Nd:YAG laser, Opt. Lett. 18, 971-973 (1993).

[31] F. G. Colville, M.H. Dunn, and M. Ebrahim-Zadeh, Continuous-wave, singly resonant intracavity parametric oscillator, Opt. Lett. 22, 75–79 (1997).

[32] T. J. Edwards, G.A. Turnbull, M.H. Dunn, M. Ebrahim-Zadeh, and F.G. Colville, High-power, continuous-wave, singly resonant intracavity optical parametric oscillator, Appl. Phys. Lett. 72, 1527–1529 (1998).

[33] M. Scheidt, B. Beier, R. Knappe, K.-J. Boller, and R. Wallenstein, Diode-laser pumped continuous-wave KTP optical parametric oscillator, J. Opt. Soc. Am. B 12, 2087–2094 (1995).

[34] M. Scheidt, B. Beier, K.-J. Boller, and R. Wallenstein, Frequency-stable operation of a diode-pumped continuous-wave $RbTiOAsO_4$ optical parametric oscillator, Opt. Lett. 22, 1287–1289 (1997).

[35] S. Matsumoto, E. J. Lim, H. M. Hertz, and M. M. Fejer, Quasi-phase-matched second harmonic generation of blue light in electrically periodically-poled lithium tantalate waveguides, Electron. Lett. 27, 2040-2042 (1991).

[36] W. R. Bosenberg, A. Drobshoff, J. I. Alexander, L. E. Myers and R. L. Byer, 93%-pump depletion, 3.5-W continuous-wave, singly resonant optical parametric oscillator, Opt. Lett. 21, 1336-1338 (1996).

[37] P. E. Powers, Thomas J. Kulp, and S. E. Bisson, Continuous tuning of a continuous-wave periodically poled lithium niobate optical parametric oscillator by use of a fan-out grating design, Opt. Lett. 23, 159–161 (1998).

[38] M. M. J. W. van Herpen, S. E. Bisson, and F. J. M. Harren, Continuous-wave operation of a single-frequency optical parametric oscillator at 4–5 µm based on periodically poled $LiNbO_3$, Opt. Lett. 28, 2497–2499 (2003).

[39] J. Henderson and R. Stafford, Intra-cavity power effects in singly resonant cw OPOs, Appl. Phys. B 85, 181–184 (2006).

[40] G. K. Samanta, G. R. Fayaz, Z. Sun, and M. Ebrahim-Zadeh, Highpower, continuous-wave, singly resonant optical parametric oscillator based on MgOsPPLT, Opt. Lett. 32, 400-402 (2007).

[41] S. Chaitanya Kumar, R. Das, G. K. Samanta, and M. Ebrahim-Zadeh, Optimally output-coupled, 17.5 W, fiber-laser-pumped continuous-wave optical parametric oscillator, Appl. Phys. B: Lasers Opt. 102, 31-35 (2011).

[42] M. E. Klein, C. K. Laue, D. H. Lee, K. J. Boller, and R. Wallenstein, Diode-pumped singly resonant continuous-wave optical parametric oscillator with wide continuous tuning of the near-infrared idler wave, Opt. Lett. 25, 490-492 (2000).

[43] M. Vainio, J. Peltola, S. Persijn, F. J. M. Harren, and L. Halonen, Singly resonant cw OPO with simple wavelength tuning, Opt. Express 16, 11141-11146 (2008).

[44] G. K. Samanta, S. Chaitanya Kumar, K. Devi, and M. Ebrahim-Zadeh, Multicrystal, continuous-wave, single-pass second-harmonic generation with 56% efficiency, Opt. Lett. 35, 3513-3515 (2010).

[45] A. Henderson, and R. Stafford, Spectral broadening and stimulated Raman conversion in a continuous-wave optical parametric oscillator, Opt. Lett. 32, 1281-1283 (2007).

[46] G. K. Samanta, and M. Ebrahim-Zadeh, Continuous-wave, single-frequency, solid-state blue source for the 425–489 nm spectral range, Opt. Lett. 33, 1228-1230 (2008).

[47] N. Forget, S. Bahbah, C. Drag, F. Bretenaker, M. Lefebvre, and E. Rosencher, Actively mode-locked optical parametric oscillator, Opt. Lett. 31, 972-974 (2006).

[48] R. W. Boyd, Nonlinear optics, Academic press, San Diego, USA (2007).

[49] M. Ebrahim-Zadeh and M. H. Dunn, Optical parametric oscillators, Handbook of optics, 2nd ed. (Optical Society of America, Washington, D.C.), Chapter. 22 (2000).

[50] R. L. Sutherland, Handbook of nonlinear optics, 2nd ed., Marcel Dekker, Inc. (1996).

[51] V. G. Dmitriev, G. G. Gurzadyan, and D. N. Nikogosyan, Handbook of nonlinear optical crystals, 3rd ed., Springer (1999).

[52] M. M. Fejer, G. A. Magel, D. H. Jundt, and R. L. Byer, Quasi-phase-matched second harmonic generation: Tuning and tolerances, IEEE J. Quantum Elect. 28, 2631-2654 (1992).

[53] S. E. Harris, Tunable optical parametric oscillators, Proc. of IEEE, 57, 2096- 2113 (1969).

[54] O. Paul, A. Quosig, T. Bauer, M. Nittmann, J. Bartschke, G. Anstett, and J. A. L'Huillier, Temperature-dependent Sellmeier equation in the MIR for the extraordinary refractive index of 5% MgO doped congruent $LiNbO_3$, Appl. Phys. B: Lasers Opt. 86, 111-115 (2007).

[55] H. Kogelnik and T. Li, Laser beams and resonators, Appl. Opt. 5, 1550-1567 (1966).

[56] P. A. Belanger, Beam propagation and the ABCD ray matrices, Opt. Lett. 16, 196-198 (1991).

[57] P. W Smith, Mode-locking of lasers, Proc. IEEE, 58, 1342-1357 (1970).

[58] H. A. Haus, Mode-locking of lasers, IEEE J. Select. Topics Quantum Electron, 6, 1173-1185 (2000).

[59] M. Becker, D. Kuizenga, D. Phillion, and A. Siegman, J. Appl. Phys. 45, 3996-4005 (1974).

[60] J-M Melkonian, N. Forget, F. Bretenaker, C. Drag, M. Lefebvre, and E. Rosencher, Active mode locking of continuous-wave doubly and singly resonant optical parametric oscillators, Opt. Lett. 32, 1701-1703 (2007).

[61] D. J. Kuizenga and A. E. Siegman, FM and AM mode locking of the homogeneous laser. Pt.I:Theory, IEEE J. Quantum Electron. 6, 694-708 (1970).

[62] R. P. Scott, C. V. Bennett, and B. H. Kolner, AM and high-harmonic FM laser mode locking, Appl. Opt. 36, 5908-5912 (1997).

[63] S. E. Harris and O. P McDuff, FM laser oscillation-Theory, Appl. Phys. Lett. 5, 205-206 (1964).

[64] T. Sandrock, D. Fischer, P. Glas, M. Leitner, M. Wrage, and A. Diening, Diode-pumped 1-W Er-doped fluoride glass M-profile fiber laser emitting at 2.8 µm, Opt. Lett. 24, 1284–1286 (1999).

[65] E. Heumann, S. Bar, K. Rademaker, G. Huber, S. Butterworth, A. Diening, and W. Seelert, Semiconductor-laser-pumped high-power upconversion laser, Appl. Phys. Lett. 88, 061108-1-3 (2006).

[66] T. Kasamatsu, H. Sekita, and Y. Kuwano, Temperature dependence and optimization of 970-nm diode-pumped Yb:YAG and Yb:LuAG lasers, Appl. Opt. 38, 5149–5153 (1999).

[67] I. Goykhman, B. Desiatov, and U. Levy, Ultrathin silicon nitride microring resonator for biophotonic application at 970 nm wavelength, Appl. Phys. Lett. 97, 081108-1-3 (2010).

[68] X. G. Sun, G. W. Switzer, and J. L. Carlsten, Blue light generation in an external ring cavity using both cavity and grating feedback, Appl. Phys. Lett. 76, 955–957 (2000).

[69] L. J. Al-Muhanna, L. J. Mawst, D. Botez, D. Z. Garbuzov, R. U. Martinelli, and J. C. Connolly, High-power (>10 W) continuous-wave operation from 100-µm-aperture 0.97-µm-emitting Al-free diode lasers, Appl. Phys. Lett. 73, 1182–1184 (1998).

[70] M. Kanskar, T. Earles, T. J. Goodnough, E. Stiers, D. Botez, and L. J. Mawst, 73% cw power conversion efficiency at 50 W from 970 nm diode laser bars, Electron. Lett. 41, 245–247 (2005).

[71] C. Ruppert and M. Betz, Generation of 30 femtosecond, 900-970 nm pulses from a Ti:sapphire laser far off the gain peak, Opt. Express 16, 5572–5576 (2008).

[72] F. Demaria, S. Lorch, S. Menzel, M. C. Riedl, F. Rinaldi, R. Rosch, and P. Unger, Design of highly efficient high-power optically pumped semiconductor disk lasers, IEEE J. Sel. Top. Quantum Electron. 15, 973–977 (2009).

[73] F. Roser, C. Jauregui, J. Limpert, and A. Tunnermann, 94 W 980 nm high brightness Yb-doped fiber laser, Opt. Express 16, 17310–17318 (2008).

[74] S. C. Kumar, G. K. Samanta, and M. Ebrahim-Zadeh, High-power, single-frequency, continuous-wave second-harmonic-generation of ytterbium fiber laser in PPKTP and MgO:sPPLT, Opt. Express 17, 13711–13726 (2009).

[75] G. Frith, T. McComb, B. Samson, W. Torruellas, M. Dennis, A. Carter, V. Khitrov, and K. Tankala, Frequency doubling of Tm-doped fiber lasers for efficient 950 nm generation, in Advanced Solid-State Photonics, (Denver, Colorado, 2009), paper WB5.

[76] G. D. Boyd and D. A. Kleinman, Parametric interaction of focused Gaussian light beams, J. Appl. Phys. 39, 3597–3639 (1968).

[77] D. H. Jundt, Temperature-dependent Sellmeier equation for the index of refraction, n(e), in congruent lithium niobate, Opt. Lett. 22, 1553–1555 (1997).

[78] W. R. Bosenberg, A. Drobshoff, J. I. Alexander, L. E. Myers, and R. L. Byer, Continuous-wave singly resonant optical parametric oscillator based on periodically poled $LiNbO_3$, Opt. Lett. 21, 713–715 (1996).

[79] P. Gross, M. E. Klein, T. Walde, K.-J. Boller, M. Auerbach, P. Wessels, and C. Fallnich, "Fiber-laser-pumped continuous-wave singly resonant optical parametric oscillator," Opt. Lett. 27, 418–420 (2002).

[80] I. D. Lindsay, B. Adhimoolam, P. Groß, M. E. Klein, and K. J. Boller, 110GHz rapid, continuous tuning from an optical parametric oscillator pumped by a fiber-amplified DBR diode laser, Opt. Express 13, 1234–1239 (2005).

[81] A. Henderson and R. Stafford, Low threshold, singly-resonant cw OPO pumped by an all-fiber pump source, Opt. Express 14, 767–772 (2006).

[82] G. K. Samanta, S. C. Kumar, R. Das, and M. Ebrahim-Zadeh, Continuous-wave optical parametric oscillator pumped by a fiber laser green source at 532 nm, Opt. Lett. 34, 2255–2257 (2009).

[83] G. K. Samanta and M. Ebrahim-Zadeh, Continuous-wave singly-resonant optical parametric oscillator with resonant wave coupling, Opt. Express 16, 6883–6888 (2008).

[84] R. O. Moore, G. Biondini, and W. L. Kath, Self-induced thermal effects and modal competition in continuous-wave optical parametric oscillators, J. Opt. Soc. Am. B 19, 802–811 (2002).

[85] M. Vainio, J. Peltola, S. Persijn, F. J. M. Harren, and L. Halonen, Thermal effects in singly resonant continuous-wave optical parametric oscillators, Appl. Phys. B 94, 411–427 (2009).

[86] A. Esteban-Martin, O. Kokabee, and M. Ebrahim-Zadeh, Optimum output coupling in optical oscillators using an antiresonant ring interferometer, Opt. Lett. 35, 2786–2788 (2010).

[87] S. Chaitanya Kumar, A. Esteban-Martin, and M. Ebrahim-Zadeh, Interferometric output coupling of ring optical oscillators, Opt. Lett. 36, 1068–1070 (2011).

[88] J. E. Bjorkholm, Some effects of spatially nonuniform pumping in pulsed optical parametric oscillators, IEEE J. Quantum Electron. 7, 109–118 (1971).

[89] S. Guha, F.-J. Wu, and J. Falk, The effects of focusing on parametric oscillation, IEEE J. Quantum Electron. 18, 907–912 (1982).

[90] L. E. Myers and W. R. Bosenberg, Periodically poled lithium niobate and quasi-phase-matched optical parametric oscillators, IEEE J. Quantum Electron. 33, 1663–1672 (1997).

[91] A. E. Siegman, An antiresonant ring interferometer for coupled laser cavities, laser output coupling, mode locking, and cavity dumping, IEEE J. Quantum Electron. 9, 247–250 (1973).

[92] R. Trutna and A. E. Siegman, Laser cavity dumping using an antiresonant ring, IEEE J. Quantum Electron. 13, 955–962 (1977).

[93] H. Vanherzeele, J. L. Van Eck, and A. E. Siegman, Colliding pulse mode locking of a Nd:YAG laser with an antiresonant ring structure, Appl. Opt. 20, 3484–3486 (1981).

[94] A. E. Seigman, Laser beams and resonators: Beyond the 1960s, IEEE J. Sel. Top. Quantum Electron. 6, 1389–1399 (2000).

[95] C.-F. Cheng, Y. R. Sun, H. Pan, Y. Lu, X.-F. Li, J. Wang, A.-W. Liu, and S.-M. Hu, Cavity ring-down spectroscopy of Doppler-broadened absorption line with sub-MHz absolute frequency accuracy, Opt. Express 20, 9956-9961 (2012).

[96] G. K. Samanta, S. Chaitanya Kumar, K. Devi, and M. Ebrahim-Zadeh, High-power, continuous-wave Ti:sapphire laser pumped by fiber-laser green source at 532 nm, Opt. Lasers Eng. 50, 215-219 (2012).

[97] S. Chaitanya Kumar, G. K. Samanta, K. Devi, S. Sanguinetti, and M. Ebrahim-Zadeh, Single-frequency, high-power, continuous-wave fiber-laser-pumped Ti:sapphire laser, Appl. Opt. 51, 15-20 (2012).

[98] K. Devi, S. Chaitanya Kumar, and M. Ebrahim-Zadeh, 13.1 W, high-beam-quality, narrow-linewidth continuous-wave fiber-based source at 970 nm, Opt. Express 19, 11631-11637 (2011).

[99] U. Strossner, J.-P. Meyn, R. Wallenstein, P. Urenski, A. Arie, G. Rosenman, J. Mlynek, S. Schiller, and A. Peters, Single-frequency continuous-wave optical parametric oscillator system with an ultrawide tuning range of 550 to 2830 nm, J. Opt. Soc. Am. B. 19, 1419-1424 (2002).

[100] W. R. Bosenberg, J. I. Alexander, L. E. Myers, and R. W. Wallace, 2.5-W, continuous-wave, 629-nm solid-state laser source, Opt. Lett. 23, 207-209 (1998).

[101] S. Chaitanya Kumar, O. Kimmelma, and M. Ebrahim-Zadeh, High-power, Yb-fiber-laser-pumped, picosecond parametric source tunable across 752–860 nm, Opt. Lett. 37, 1577-1579 (2012).

[102] A. Bruner, D. Eger, M. B. Oron, P. Blau, M. Katz, and S. Ruschin, Temperature-dependent Sellmeier equation for the refractive index of stoichiometric lithium tantalate, Opt. Lett. 28, 194-196 (2003).

[103] K. Devi, S. Chaitanya Kumar, A. Esteban-Martin, and M. Ebrahim-Zadeh, Antiresonant ring output-coupled continuous-wave optical parametric oscillator, Opt. Express 20, 19313-19321 (2012).

[104] M. Ebrahim-Zadeh and M. H. Dunn, Optical parametric fluorescence and oscillation in urea using an excimer laser, Opt. Commun. 69, 161-165 (1988).

[105] A. Richter, N. Pavel, E. Heumann, G. Huber, D. Parisi, A. Toncelli, M. Tonelli, A. Diening, and W. Seelert, Continuous-wave ultraviolet generation at 320 nm by intracavity frequency doubling of red-emitting Praseodymium lasers, Opt. Express 14, 3282-3287 (2006).

[106] Y. Taira, High-power continuous-wave ultraviolet generation by frequency doubling of an argon laser, Jpn. J. Appl. Phys. 31, L682-L684 (1992).

[107] S. Chaitanya Kumar, G. K. Samanta, K. Devi, and M. Ebrahim-Zadeh, High-efficiency, multicrystal, single-pass, continuous-wave second harmonic generation, Opt. Express 19, 11152-11169 (2011).

[108] I. Ricciardi, M. De Rosa, A. Rocco, P. Ferraro, A. Vannucci, P. Spano, and P. De Natale, Sum-frequency generation of cw ultraviolet radiation in periodically poled $LiTaO_3$, Opt. Lett. 39, 1348-1350 (2009).

[109] J. Hirohashi, Y. Tomihari, T. Fukui, S. Makio, K. Suzuki, K. Imai, H. Motegi, and Y. Furukawa, Low noise cw 355 nm generation by simple

single pass configuration with PPMgSLTs from fiber based laser, Lasers, Sources, and Related Photonic Devices Technical Digest (2012).

[110] M. Ghotbi, Z. Sun, A. Majchrowski, E. Michalski, I. V. Kityk, and M. Ebrahim-Zadeh, Efficient third harmonic generation of microjoule picosecond pulses at 355 nm in BiB_3O_6, Appl. Phys. Lett. 89, 173124-1-3 (2006).

[111] M. Ebrahim-Zadeh, Efficient ultrafast frequency conversion sources for the visible and ultraviolet based on BiB_3O_6, IEEE J. Sel. Top. Quantum Electron. 13, 679–691 (2007).

[112] V. Petrov, M. Ghotbi, O. Kokabee, A. Esteban-Martin, F. Noack, A. Gaydardzhiev, I. Nikolov, P. Tzankov, I. Buchvarov, K. Miyata, A. Majchrowski, I. Kityk, F. Rotermund, E. Michalski, and M. Ebrahim-Zadeh, Femtosecond nonlinear frequency conversion based on BiB_3O_6, Laser & Photon. Rev. 4, 53-98 (2010).

[113] M. Peltz, J. Bartschke, A. Borsutzky, R. Wallenstein, S. Vernay, T. Salva, and D. Rytz, Harmonic generation in bismuth triborate (BiB_3O_6), Appl. Phys. B 81, 487–495 (2005).

[114] S. Moller, A. Andresen, C. Merschjann, B. Zimmermann, M. Prinz, and M. Imlau, Insight to UV-induced formation of laser damage on LiB_3O_5 optical surfaces during long-term sum-frequency generation, Opt. Express 15, 7351-7356 (2007).

[115] M. Tang, H. Minamide, Y. Wang, T. Ntake, S. Ohno, and H. Ito, Dual-wavelength single-crystal double-pass KTP optical parametric oscillator and its application in terahertz wave generation, Opt. Lett. 35, 1698-1700 (2010).

[116] J. Kiessling, F. Fuchs, K. Buse, and I. Breunig, Pump-enhanced optical parametric oscillator generating continuous-wave tunable terahertz radiation, Opt. Lett. 36, 4374-4376 (2011).

[117] G. K. Samanta and M. Ebrahim-Zadeh, Dual-wavelength, two crystal, continuous-wave optical parametric oscillator, Opt. Lett. 36, 3033-3035 (2011).

[118] A. Esteban-Martin, V. Ramaiah-Badarla, and M. Ebrahim-Zadeh, Dual-wavelength optical parametric oscillator using antiresonant ring interferometer, Laser Photonics Rev. 6, 7-11 (2012).

[119] A. Esteban-Martin, G. K. Samanta, K. Devi, S. Chaitanya Kumar, and M. Ebrahim-Zadeh, Frequency-modulation-mode-locked optical parametric oscillator, Opt. Lett. 37, 115-117 (2012).

[120] K. Gurs and R. Mullers, Breitband-modulation durch steurung der emission eines optischen masers (Auskopple-modulation), Phys. Lett. 5, 179-181 (1963).

[121] F. J. Duarte, Tunable laser applications, CRC, New York, (2009).

[122] J. F. Ready, Industrial applications of lasers, Academic, New York, (1997).

[123] D. E. Spence, P. N. Kean, and W. Sibbett, 60-fsec pulse generation from a self-mode-locked Ti:sapphire laser, Opt. Lett. 16, 42-44 (1991).

[124] S. E. Harris and R. Targ, FM oscillation of the He-Ne laser, Appl. Phys. Lett. 5, 202-204 (1964).

[125] E. O Ammann, B. J. McMurtry, and M. K. OShman, Detailed experiments on Helium-Neon FM lasers, IEEE J. Quantum Electron. 1, 263-272 (1965).

[126] D. J. Kuizenga, Mode locking of the cw Dye laser, Appl. Phys. Lett. 19, 260-263 (1971).

[127] G. T. Maker and A. I. Ferguson, Frequency-modulation mode locking of a diode-pumped Nd:YAG laser, Opt. Lett. 14, 788-790 (1989).

[128] D. W. Hughes, J. R. M. Barr, and D. C. Hanna, Mode locking of a diode-laser-pumped Nd:glass laser by frequency modulation," Opt. Lett. 16, 147-149 (1991).

[129] G. W. Hong and J. R. Whinnery, Switching of phase-locked states in the intracavity phase-modulated He-Ne laser, IEEE J. Quantum Electron. 5, 367-376 (1969).